

# **THE APPLICATION OF THE HOMOGENISATION METHOD TO THE NUMERICAL MODELLING OF CANCELLOUS BONE**

**BY**

**D.J. CONWAY**

A thesis submitted in partial fulfillment of the requirements for  
the degree of Master of Science in Engineering

Department of Mechanical Engineering  
University of Cape Town  
Rondebosch 7700  
South Africa

August 1995

The University of Cape Town has been given  
the right to reproduce this thesis in whole  
or in part. Copyright is held by the author.

The copyright of this thesis vests in the author. No quotation from it or information derived from it is to be published without full acknowledgement of the source. The thesis is to be used for private study or non-commercial research purposes only.

Published by the University of Cape Town (UCT) in terms of the non-exclusive license granted to UCT by the author.

## DECLARATION

This is to certify that the results, calculations and other work presented in this thesis are essentially my own, and that no part of it has been submitted for a degree at this or any other university

Signed by candidate

Signature Removed

D.J. Conway  
August 1995

---

## ACKNOWLEDGEMENTS

---

Sincere thanks to the following people:

- My supervisors, Dr Greg Mitchell - for his interest, and very helpful guidance throughout my masters, and Mr Thanos Spirakis - for his encouragement and advice.
- Colleagues and friends at CERECAM; in particular: Greg Starke, Mike Eastman and Hellmut Bowles for their untiring assistance, encouragement, and many helpful “hints”. The people of CERECAM have helped to make my studies here very rewarding and enjoyable.
- My parents for their support, encouragement, and saint-like patience.

I would also like to thank the FRD and CERECAM for their financial support.

---

## SYNOPSIS

---

This thesis reports on an investigation into the viability of developing idealised numerical models of cancellous bone in order to make reasonable predictions about its macro- and microstructural mechanical behaviour using the homogenisation method.

In total joint replacement, cancellous bone (the soft porous bone which lies below the articular surfaces at weight-bearing joints) provides the medium for the transfer of loads from the artificial component, or prosthesis to the hard, outer cortical bone. Although total joint replacement is usually a successful operation - providing relief from pain and often considerably improved joint function - loosening of the metal components remains a major obstacle to the long-term success of these operations. In the ongoing work to develop joints which are less susceptible to loosening, it has become necessary to study the micromechanics of cancellous bone in order to predict its response to the changing stress environments brought about by the inserted prostheses.

Biomechanical engineers have used finite element analysis extensively in the analysis of reconstructed joints. However, owing to the prohibitively high computational costs associated with the microstructural modelling of cancellous bone, it is generally modelled simply as a homogeneous, isotropic material. It is not possible to accurately predict the mechanical response of cancellous bone to various implant conditions under this simplistic modelling assumption. Thus, alternative methods are being sought which will allow for more realistic modelling of cancellous bone. The homogenisation method is one such alternative. This method makes it possible to uncouple the analysis of some problem involving a composite material into an apparent global analysis and a local microstructural analysis. The apparent material properties of the periodically repeating composite microstructure are calculated, taking into account the structural heterogeneities of the composite. These properties are then used in the global analysis where the composite is treated as a continuum. The apparent global-level results are subsequently postprocessed to obtain the microstructural behaviour in any local regions of interest.

The main aim of this research project was to investigate the applicability of the homogenisation method to the modelling of cancellous bone. The first part of this work involved an extensive literature study on the architecture and micromechanics of cancellous bone to investigate whether cancellous bone can indeed be modelled as an idealised composite material with a periodically repeating microstructure. The outcome of this investigation revealed that the structure and behaviour of cancellous bone is highly variable - depending on the patient, anatomic location and the level of density. However, certain regions of cancellous bone do have typical repeating architectures which have a major influence on the apparent mechanical behaviour of the bone. Thus it has been concluded that these specific regions of cancellous bone can be modelled by idealised structures, provided the observed microstructures and predominant deformations modes are well characterised in the models.

The next step involved the implementation of the homogenisation method within a three-dimensional finite element code. A number of numerical trials were then set up to ascertain the levels of accuracy that can be expected when using the homogenisation method to model highly porous microstructures such as cancellous bone under conditions which are typical of the reconstructed joint environment. These trials indicated that the homogenisation method generally provides reasonably accurate predictions of the microstructural behaviour of structures which undergo compression, shearing and bending. This technique was thus deemed to be suitable for the analysis of idealised models of cancellous bone.

Previous studies have attempted to create idealised models of cancellous bone. However, these models have generally been limited, since the possibility of internal bending deformations, and the orthotropic nature of cancellous bone have not been accommodated. In this study a range of more realistic idealised finite element models of cancellous bone microstructure from the upper knee (proximal tibia) have been developed. The apparent material properties of these models have been calculated using the homogenisation method, and compared to previously published experimental data for bone specimens from this region. Although some difficulty was experienced in the correlation of actual stiffness magnitudes, it was found that the overall orthotropic behaviour of this type of cancellous bone could be well simulated by the idealised models over a large range of apparent densities. The actual magnitudes could be improved by using a higher level of discretisation, more accurate bone-tissue material properties and more refined structural models of the bone microstructures. However, the good results of this feasibility study give a strong indication that, provided the cancellous bone is modelled to a sufficiently high level of sophistication, idealised models can be developed and analysed using the homogenisation method to achieve reasonably high levels of accuracy in the prediction of cancellous bone behaviour on both the macro- and microstructural level. Although this conclusion is based on the results for models of the proximal tibia, it can reasonably be extended to all regions of cancellous bone which exhibit typical repeating microstructural architectures.

---

# TABLE OF CONTENTS

---

|                                                                                       | <u>PAGE</u> |
|---------------------------------------------------------------------------------------|-------------|
| <b>ACKNOWLEDGEMENTS</b>                                                               | i           |
| <b>SYNOPSIS</b>                                                                       | ii          |
| <b>TABLE OF CONTENTS</b>                                                              | iv          |
| <b>LIST OF FIGURES</b>                                                                | vi          |
| <b>LIST OF TABLES</b>                                                                 | viii        |
| <b>CHAPTER 1: INTRODUCTION</b>                                                        | 1           |
| <b>1.1 OVERVIEW</b>                                                                   | 1           |
| <b>1.2 BACKGROUND</b>                                                                 | 4           |
| <b>1.3 OBJECTIVES</b>                                                                 | 9           |
| <b>1.4 PLAN OF THIS THESIS</b>                                                        | 10          |
| <b>CHAPTER 2: CANCELLOUS BONE</b>                                                     | 11          |
| <b>2.1 MORPHOLOGICAL/ARCHITECTURAL CHARACTERISTICS<br/>        OF CANCELLOUS BONE</b> | 12          |
| <b>2.2 EXPERIMENTAL EVIDENCE</b>                                                      | 16          |
| 2.2.1 EXPERIMENTAL METHODS                                                            | 16          |
| 2.2.2 EXPERIMENTAL AND ANALYTICAL RESULTS                                             | 17          |
| 2.2.3 DISCUSSION                                                                      | 25          |
| <b>2.3 MATERIAL PROPERTIES OF SOLID PHASE<br/>        TRABECULAR BONE</b>             | 26          |
| <b>CHAPTER 3: THE HOMOGENISATION METHOD</b>                                           | 27          |
| <b>3.1 INTRODUCTION TO HOMOGENISATION</b>                                             | 27          |
| <b>3.2 THEORY OF HOMOGENISATION</b>                                                   | 31          |
| <b>3.3 IMPLEMENTATION IN THE FINITE ELEMENT METHOD</b>                                | 35          |
| <b>3.4 NUMERICAL TRIALS</b>                                                           | 37          |
| 3.4.1 BOUNDARY AND LOADING CONDITIONS                                                 | 41          |
| 3.4.2 PERIODICITY                                                                     | 43          |
| 3.4.3 INTEGRATION SCHEME AND BOUNDARY EFFECTS                                         | 45          |
| 3.4.4 NON-UNIFORM LOADING                                                             | 48          |
| 3.4.5 BENDING MODES                                                                   | 51          |
| <b>3.5 DISCUSSION</b>                                                                 | 55          |

|                                                                                              |    |
|----------------------------------------------------------------------------------------------|----|
| <b>CHAPTER 4: IDEALISED MODELS OF CANCELLOUS BONE<br/>USING THE HOMOGENISATION METHOD</b>    | 56 |
| <b>4.1 PREVIOUS WORK</b>                                                                     | 56 |
| <b>4.2 IDEALISED FINITE ELEMENT MODELS OF CANCELLOUS<br/>    BONE IN THE PROXIMAL TIBIA</b>  | 60 |
| 4.2.1 MODEL I                                                                                | 62 |
| 4.2.2 MODEL II                                                                               | 62 |
| 4.2.3 MODEL III                                                                              | 64 |
| 4.2.4 MODEL IV                                                                               | 67 |
| 4.2.5 MODEL V AND MODEL VI                                                                   | 67 |
| 4.2.6 REGRESSION ANALYSIS OF NUMERICAL RESULTS                                               | 68 |
| 4.2.7 GLOBAL KNEE MODEL                                                                      | 69 |
| <b>4.3 DISCUSSION</b>                                                                        | 71 |
| <br>                                                                                         |    |
| <b>CHAPTER 5: CONCLUSIONS</b>                                                                | 73 |
| <br>                                                                                         |    |
| <b>REFERENCES</b>                                                                            | 75 |
| <br>                                                                                         |    |
| <b>APPENDIX A: Definition of the Sample Correlation Coefficient</b>                          | A1 |
| <b>APPENDIX B: Theory of homogenisation</b>                                                  | B1 |
| <b>APPENDIX C: Tables of results for numerical homogenisation trials</b>                     | C1 |
| <b>APPENDIX D: Tables of homogenised engineering constants for<br/>idealised bone models</b> | D1 |
| <b>APPENDIX E: User information on homogenisation code</b>                                   | E1 |

---

## LIST OF FIGURES

---

**FIGURE**  
**PAGE**

|                                                                                                                                                  |    |
|--------------------------------------------------------------------------------------------------------------------------------------------------|----|
| 1.1 Human skeleton                                                                                                                               | 5  |
| 1.2 Vertebral cancellous bone                                                                                                                    | 6  |
| 1.3 Reconstructed knee joint with cemented prosthesis                                                                                            | 6  |
| 2.1a-d Types of cancellous bone                                                                                                                  | 13 |
| 2.2 Analytical idealised models of cancellous bone                                                                                               | 13 |
| 2.4 Cubic and linear regression curves to data for apparent vertical stiffness of proximal tibial cancellous bone                                | 19 |
| 3.1a Open-cell bone matrix containing roughly spherical pores                                                                                    | 28 |
| 3.1b Beaupre and Hayes' (1985) idealised spherical bone model                                                                                    | 28 |
| 3.2 Global and local domains of a composite material                                                                                             | 31 |
| 3.3 Schematic of procedure for numerical homogenisation trials                                                                                   | 38 |
| 3.3a Periodic boundary conditions applied to base-cell                                                                                           | 39 |
| 3.4 First base-cell model                                                                                                                        | 40 |
| 3.5 Symmetrical half of first global test model                                                                                                  | 40 |
| 3.6a-c Homogenisation and standard finite element predictions of strain energy densities in innermost base-cell for first numerical trial        | 42 |
| 3.7 Second global test model                                                                                                                     | 43 |
| 3.8a-c Homogenisation and standard finite element predictions of strain energy densities in innermost base-cell for second numerical trial       | 44 |
| 3.9a,b Displaced shape and percentage errors in strain energy density for second global model using reduced integration                          | 46 |
| 3.9c,d Homogenisation and standard FEM predictions of strain energy densities in full global model (uniform shear and compressive loading)       | 47 |
| 3.10a,b Displaced shape and percentage errors in strain energy density for third global model using reduced integration                          | 49 |
| 3.10c,d Homogenisation and standard FEM predictions of strain energy densities in full global model (eccentric compressive loading)              | 50 |
| 3.11 Bending test base-cells                                                                                                                     | 52 |
| 3.12 Apparent vertical stiffness versus apparent density for base-cell structures with internal bending members                                  | 52 |
| 3.13a-c Homogenisation and standard finite element predictions of strain energy densities in base-cell structure containing bending deformations | 53 |

|                                                                                                                           |    |
|---------------------------------------------------------------------------------------------------------------------------|----|
| 4.1a-c Idealised models of cancellous bone (Hollister <i>et al.</i> , 1994)                                               | 57 |
| 4.2 Digitised 1mm cube sample of cancellous bone from lumbar spine                                                        | 57 |
| 4.3a,b Transverse and vertical views of high density bone from the proximal tibia                                         | 61 |
| 4.4 Model I                                                                                                               | 63 |
| 4.5 Model II                                                                                                              | 63 |
| 4.6 Model III                                                                                                             | 65 |
| 4.7 Model IV                                                                                                              | 65 |
| 4.8 Model V                                                                                                               | 65 |
| 4.9 Model VI                                                                                                              | 65 |
| 4.10a,b Oblique and vertical views of stacked base-cells (Model VI)                                                       | 66 |
| 4.11 Regression curves to numerical predictions and experimental data of Williams and Lewis (1982) for vertical stiffness | 68 |
| 4.12 Simple global model of cementless reconstructed tibia                                                                | 69 |
| 4.13a,b Vertical axial stresses in orthotropic and isotropic cancellous bone regions                                      | 70 |
| 4.14a,b In-plane shear stresses in orthotropic and isotropic cancellous bone regions                                      | 70 |

---

## LIST OF TABLES

---

| <u>TABLE</u>                                                                                | <u>PAGE</u> |
|---------------------------------------------------------------------------------------------|-------------|
| 2.1 Summary of Singhs' (1978) categorisations of cancellous bone                            | 14          |
| 2.2 Regression results from experimental data of apparent stiffness versus apparent density | 24          |
| 2.3 Experimentally measured values of apparent modulus                                      | 24          |
| 2.4 Experimentally measured values of trabecular tissue modulus                             | 26          |
| 3.1 Summary of results of numerical homogenisation trials                                   | 54          |
| 4.1 Homogenisation predictions of apparent Young's moduli of idealised models               | 63          |

---

# CHAPTER 1

## INTRODUCTION

---

### 1.1 OVERVIEW

The degeneration of joints and bone, associated with ageing and bone diseases such as osteoporosis, rheumatoid arthritis and osteoarthritis is a world-wide health problem. There is strong evidence that general bone strength has been rapidly decreasing in both men and women over the last 30 years. An increase in the incidence of femoral head and vertebral fractures of up to four-fold over this period has been reported in some European countries (Mosekilde 1993). The factors which contribute to this drop in bone strength, have been the subject of ongoing and intensive research.

In cases of chronic joint degeneration, total joint replacement is often necessary. The number of patients requiring total joint replacements at increasingly younger ages is growing rapidly. Thus the demand for longer lasting joint replacements is ever-increasing. Although total joint replacement is usually a very successful operation, loosening of the artificial components or prostheses is still a major problem, and a typical joint replacement is not normally expected to last longer than fifteen years. The process of loosening is poorly understood because the micromechanics of the prosthesis/bone interfaces are poorly understood. Thus the stress and strain fields in the underlying bone, and at the artificial and biological material interfaces need to be studied in depth. A greater level of understanding of the microstructural architecture and behaviour of bone will improve the prediction of the responses of bone to changing stress environments. This enhanced knowledge will thus help to further the development of longer lasting prostheses.

The prostheses, which replace the diseased articulating surfaces, are attached to the porous bone (called cancellous or trabecular bone) which lies underneath the cartilage. This bone plays a very important role in the transfer of loads at large weight-bearing joints such as the knee and hip. Cancellous bone has complex region-specific microstructures (made up of various combinations of strut- and plate-like members, or trabeculae) which undergo considerable changes in structure and morphology during the process of ageing. The losses in both strength and impact absorption properties, associated with these structural changes, are compounded by the negative effects of degenerative bone diseases. While an understanding of the histological (cell-level) and physiological changes that take place is crucial to prevent joint and bone degradation in the future, it is also important that the structural changes and mechanical behaviour are well understood. The structural and material responses of bone to changing load environments are thought to be driven by mechanical stimuli such as strain (Carter (1984)) and micro-motion (Galante (1977)). Therefore the prediction of these responses is not only a physiological problem but also a mechanical one.

The fact that there is still a wide variety of different prosthesis designs in use - especially for the hip and knee - would suggest that optimal designs have not yet been developed. Each design will result in a different stress field within the surrounding cancellous bone. Probably the most favourable design would be one that induces a stress field which is as normal or physiological as possible so that any post-operative bone remodelling is minimised. Bone remodelling is a biological process which results in a redistribution of bone density caused by long term changes in the day-to-day stress magnitudes and distributions within the bone. In a reconstructed joint, the stiff metal component tends to shield the surrounding bone from the physiological stresses, causing bone resorption (reduction in density) in that region. If the artificial component is designed to minimise the stress shielding, thus reducing the amount of bone resorption around the implant, the chances of implant loosening and ultimate joint failure are reduced, and consequently the life-expectancy of the total joint replacement is improved.

Finite element analysis (FEA) has been used extensively in biomechanics to predict the mechanical behaviour of reconstructed joints (Mackerle 1994). Many of the larger joint replacement manufacturing companies use FEA to analyse and compare various prostheses. However, the high computational costs that are necessary to model the complex implant configurations make it impossible for cancellous bone to be modelled as anything but a homogeneous material. This oversimplification, while perhaps adequate for the purposes of obtaining an overall idea of the behaviour of the inserted component, is not representative enough to enable one to make realistic predictions about the microstructural mechanics of cancellous bone. Thus alternatives to the standard finite element analysis have to be considered, which will enable one to make predictions about not only the global behaviour of a reconstructed joint, but also the microstructural behaviour of the surrounding bone. One such alternative is the homogenisation method.

The homogenisation method is a mathematically rigorous technique which has been developed for the global and local analysis of problems involving composite or porous materials with complex microstructures. The technique makes it possible to characterise the average mechanical behaviour as well as the local effects of the composite material heterogeneities without the need for a high degree of finite element discretisation in large global problems. Homogenisation involves the calculation of effective elastic properties of the basic composite microstructure which can then be used in a finite element analysis of a global problem. Microstructural stress or strain values in local regions of interest within the global domain can then be calculated by postprocessing the global strain results.

The homogenisation method provides a promising technique for the macro- and microstructural analysis of cancellous bone behaviour (Hollister (1991, 1993)). However, it will only produce meaningful results if realistic numerical models of cancellous bone can be developed which characterise the general microstructural architecture and behaviour reasonably well. A number of researchers have suggested models for cancellous bone for the purposes of modelling its mechanical behaviour: Gibson (1985), Williams and Lewis (1982), Beaupre and Hayes (1985), Hollister (1991). Their models are based on the reasonable assumption that cancellous bone, like other cellular materials, can be modelled by idealising the observed structures, characterising the trabecular material properties and analysing the mechanisms by which the trabeculae (bone fibres)

deform. In order to validate such models, these researchers have compared the macrostructural or apparent behaviour of their numerical or analytical models to the results from experimental tests on cancellous bone specimens. They have assumed that if there is a good correlation between the global behaviour of the idealised models and the actual test specimens, then there will be a good correlation between the microstructural behaviour of the models and the real bone - provided the original modelling assumptions are accurate. Although it is difficult to verify, this reasonable approach to the modelling of cancellous bone has been adopted in this research project. For clarity, the principal assumption of this thesis, which includes the modelling of cancellous bone using the homogenisation method is stated below:

**If the basic characteristics which affect the mechanical behaviour of cancellous bone are well modelled, then a good correlation between the apparent behaviour of the idealised models and the actual bone test specimens is indicative of a reasonably good correlation between the microstructural behaviour of the idealised models and the actual bone. And so, if the idealised models can be designed to exhibit the same apparent behaviour as that of the actual bone, then the homogenisation method can be used to predict the microstructural behaviour of cancellous bone in large global analyses.**

The aim of the research project has been to assess the viability of creating realistic idealised models of cancellous bone microstructure with apparent material properties that correlate with the experimental evidence of previous research. The homogenisation method has been used to calculate the apparent material properties of these idealised finite element models which have been developed based on the observations and empirical evidence of a number of previous studies on cancellous bone.

## 1.2 BACKGROUND

In this section, some background information is given on cancellous bone regarding its anatomic function, location and biological and mechanical behaviour. The problems associated with the modelling of cancellous bone in joint replacement analyses using the finite element method are also introduced.

The human skeleton in Figure 1.1 identifies some of the bones that will be referred to in this thesis. Bone occurs in two forms: as a dense solid known as cortical bone, and as a porous material known as cancellous or trabecular bone which is made up of a network of rod- and plate-like trabeculae. In this thesis the term “trabecular” will refer to the individual bone fibres which make up this spongy bone, while “cancellous” will refer to the overall porous material.

In this research project, cancellous bone from the upper knee (proximal tibia) has been studied in depth. The knee joint (along with the hip joint) requires reconstructive surgery most frequently, and so it is important that the microstructural behaviour of the cancellous bone in this region is well understood. Another reason for the importance of this region is that it is subjected to high static and dynamic loads during normal daily activities. The structural morphology (architecture) in proximal tibial cancellous bone is fairly complex. It is not as regular or as simple as bone from the distal femur (lower thigh bone), yet more regular and columnar in architecture than bone from the proximal femur (upper thigh bone). This is discussed in detail in Chapter 2. Many experimental studies have been conducted on proximal tibial cancellous bone, and the availability of experimental data has made this a convenient region to investigate.

Cortical bone provides the hard outer structural shell of most bones. Cancellous bone is continuous with the inner surface of the cortical shell, and exists mainly at the long ends of the larger weight-bearing bones such as the tibia, femur and the vertebrae. A typical example of cancellous bone is shown in Figure 1.2. This softer, spongy bone underneath the articulating joint surfaces provides a medium for the transfer of loads from the joint to the outer cortical shell. Cancellous bone has a high strength to weight ratio to provide this support while minimising the total bone mass. In addition to its load transfer function, cancellous bone also provides an impact absorption cushion which helps to protect the cartilage at the joint from damage. The microstructure of cancellous bone varies considerably according to the type and magnitudes of loads which it experiences under normal or physiological conditions. If the loading is predominantly uniaxial, as in the proximal (upper) tibia and distal (lower) femur, the trabeculae tend to form columnar structures with cylindrical symmetry. In this case, the stiffness in the direction of principal loading (i.e. the vertical direction) is somewhat higher than that in the transverse directions. If the loading is complex, as in the proximal femur and the patella (knee-cap), the cancellous bone microstructure is also complex and highly asymmetrical. In general, the higher the loads, the greater the relative or apparent density - which is the ratio of solid bone volume to total volume of the cancellous bone. Structural variations (including a range of apparent densities from about 0.05 to 0.4) do not only occur between different bones; significant variations in structure and density can also occur locally within an anatomical region.

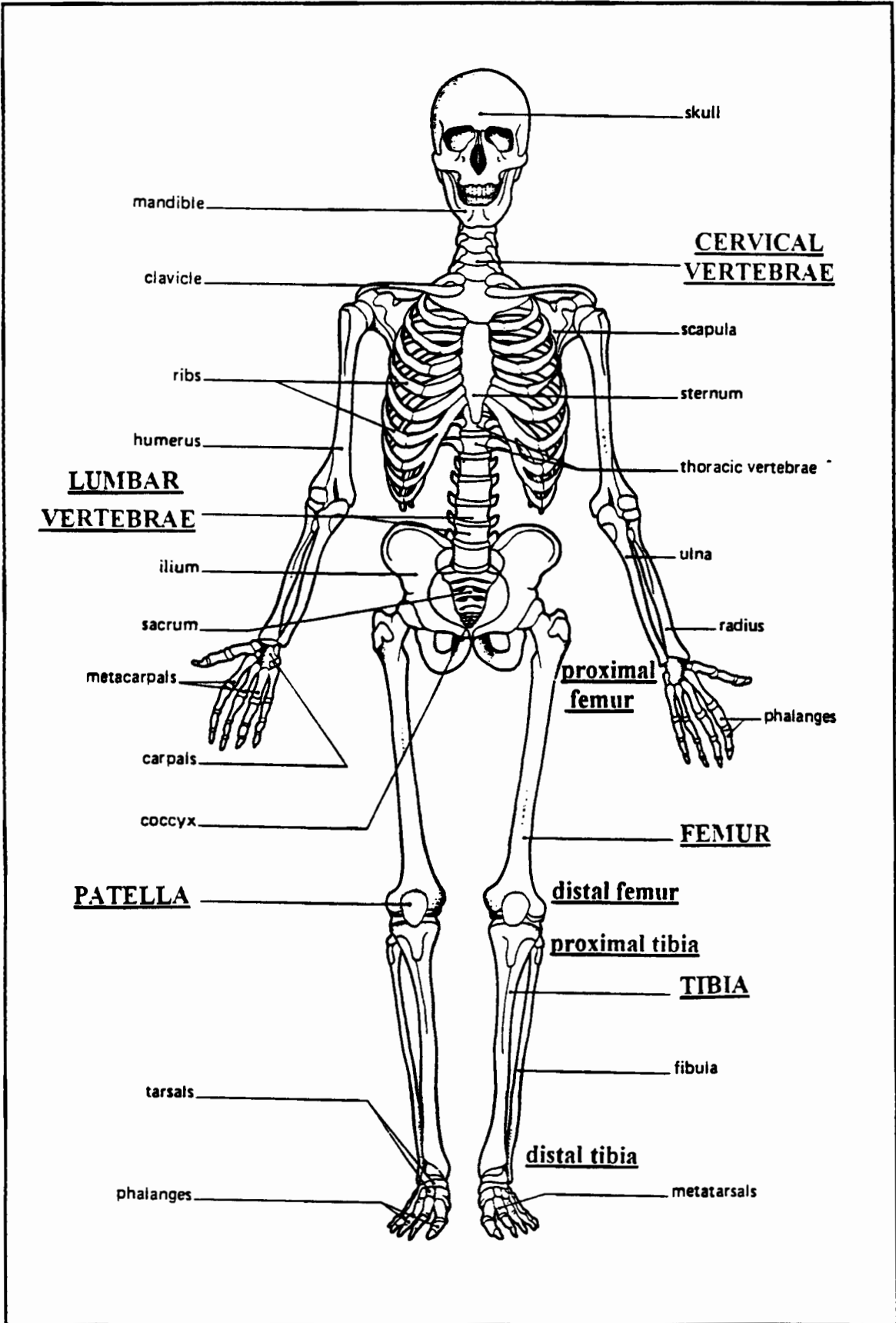


**FIGURE 1.1 Human skeleton**  
 (bones and bone regions mentioned in this thesis are underlined)

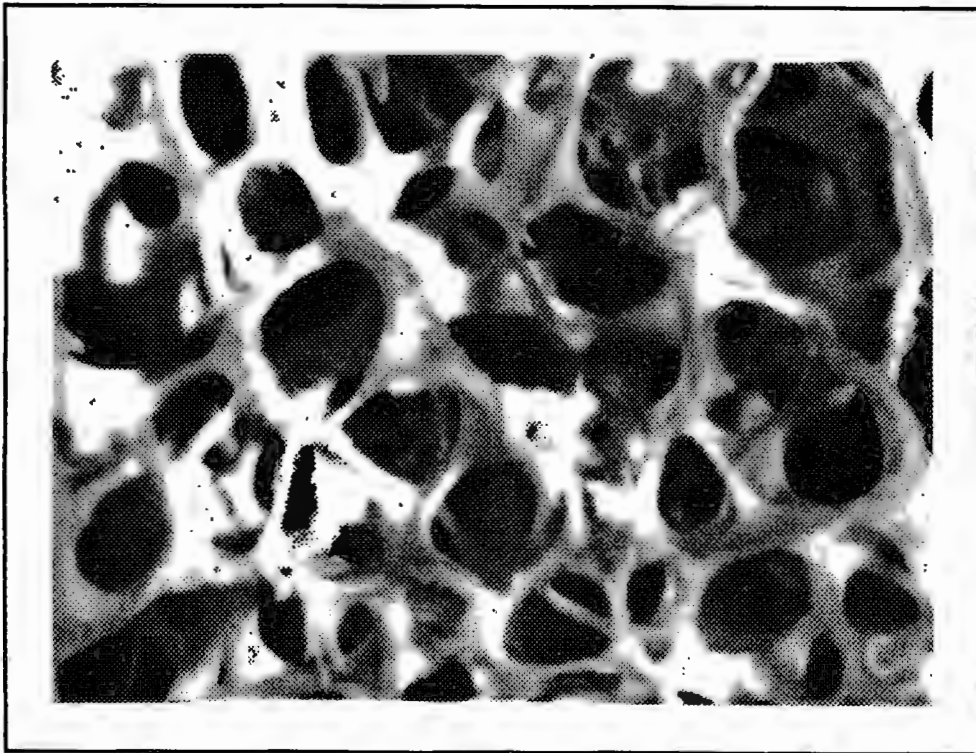


**FIGURE 1.2 Vertebral Cancellous bone (TYPE I)**  
**Amstutz and Sissons (1969)**

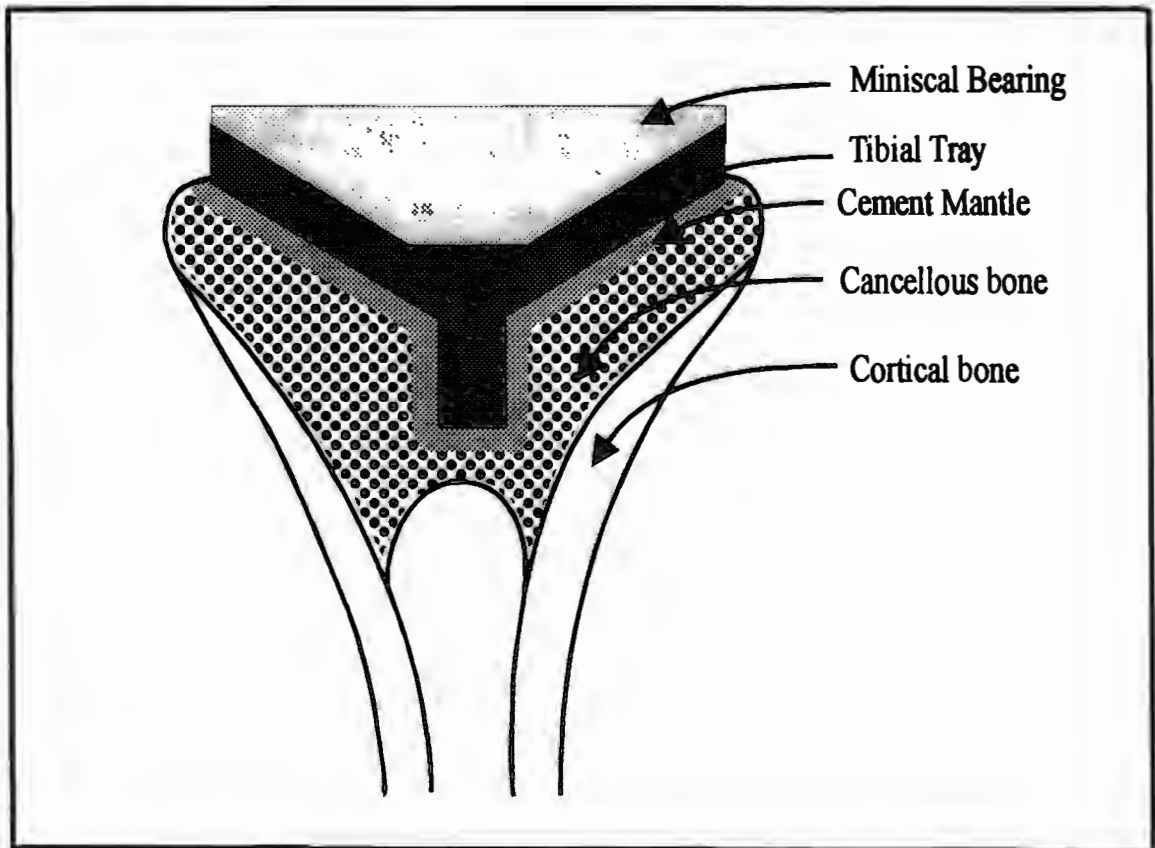


**FIGURE 1.3 Reconstructed knee joint with cemented prosthesis**  
**(tibial component)**

Perhaps the most important characteristic which affects the apparent mechanical behaviour of cancellous bone is the mode of deformation of the individual trabeculae. The trabecular behaviour is dependent on the actual bone structure and on the level of porosity of the cancellous bone. Owing to the generally anisotropic microstructure of cancellous bone, the predominant deformation modes can differ along different orientations for the same region of bone. Under normal compressive loads, the trabeculae in a particular region of bone will deform by some combination of bending and axial compression. When the individual trabeculae deform by some degree of bending and not only by axial compression, the apparent compressive stiffness of the cancellous bone is considerably reduced while maintaining strength, thus improving the impact absorption characteristics. Therefore trabecular structures underlying weight-bearing joints which frequently experience high impact loads generally exhibit considerable bending under compressive loads.

Since bone is a living material, it undergoes morphological and structural changes in response to changing environments of stress. When general stress levels are reduced over a long period of time, the bone in that region will resorb (i.e. reduce in density). Conversely, long-term increases in stress will result in bone densification. The driving force behind this mechanism is the maintenance of a high strength to weight ratio of bone. In addition to changes in density, the orientation of cancellous bone fibres (i.e. the struts or plates) will also adapt to optimise the load transfer characteristics of the bone. In joint replacement, the artificial component is usually cemented into the resected bone, and is supported by a mantle of trabecular bone. This is illustrated for a knee replacement in Figure 1.3. If the cement and implant take up too much of the load and transfer it directly to the cortical region, the surrounding cancellous bone will be shielded from its normal stress environment and it will tend to resorb away from the implant. This process will compromise the strength of the implant fixation, and increase the risk of implant loosening.

Another method for bonding the metal implant to the bone is the cementless method. Cementless implants have porous coatings which consist of small metal beads on the implant surface. The cancellous bone grows into these beads to establish a strong bond between the implant and the bone. However, loosening is also a problem with this cementless procedure. Establishing a strong implant-bone bond through bony ingrowth into the porous coating has proved difficult, and this method is not used as frequently as the more conventional cemented method.

Regardless of the method of fixation that is used, the cancellous bone remains the most important link in the transfer of loads from the artificial component to the hard outer cortical shell, and it is crucial that the stress fields induced by the implant at the biological interfaces and in the general cancellous region are favourable.

Finite element analysis is used frequently to gain a better understanding of the effect on the stresses in the surrounding cement and bone to some change in the overall implant environment such as loading conditions, cement thickness, cement modulus, implant design, and cement-implant, bone-cement or bone-implant interface conditions. Although it is generally accepted that the complex and varied microstructure of cancellous bone will have a significant influence on the mechanical behaviour of the bone - and thus on the overall result - most investigators make the assumption that cancellous bone can be

modelled as an isotropic continuum material. This assumption has been justified on the basis that the continuum model for cancellous bone - while providing no information on the microstructural response of bone - allows one to make reasonable predictions about the overall response of a given implant environment to a particular set of conditions. While this justification might be valid, it is still important that the global behaviour of the particular region of cancellous bone is well characterised in the implant model. This requires a thorough knowledge of the generally anisotropic material constants of cancellous bone, which are highly dependent on the particular microstructure of the bone. Furthermore, as implant designs become more refined, it is becoming necessary for the implant development engineers to be able to predict not only the global, but also the microstructural responses of cancellous bone to implant designs. They have to be sure that seemingly innocuous apparent stress levels do not cause localised cancellous bone failure where the interfaces between the biological tissue and the implant are critical. The ability to predict possible trabecular reorientations owing to long term changes in the stress environment would also make a valuable contribution to the design process.

Harrigan *et al.* (1988) investigated the limitations of the continuum assumption made by most biomechanics analysts, and established length scales over which the continuum assumption is valid in cancellous bone. This study was based on work done by Potter and Foss (1975) who established a process for calculating acceptable length scales at which a certain required accuracy is achieved for a non-continuum material. This classical method was applied to cancellous bone, and the authors found that within three to five intertrabecular lengths of an implant, continuum modelling is not valid and should be replaced by a statistical model of the interface. They also concluded that if a continuum model of bone predicts results which vary by 20% to 30% over a distance spanning three to five trabeculae, then the results will be unreliable.

Williams and Lewis (1982) illustrated the importance of the anisotropy of cancellous bone by using experimentally measured transversely isotropic properties of cancellous bone in the proximal tibia in a finite element analysis of a reconstructed knee joint. The peak normal and shear stresses were 50% and 20% lower than the respective results for the same model using an isotropic material for cancellous bone.

In the light of this evidence, there is an obvious need for modelling techniques which include the anisotropic nature and which can predict the microstructural behaviour of cancellous bone. However, the modelling of the structural heterogeneity of cancellous bone in a full finite element model for structural skeletal analysis is totally impractical if not impossible. Various approaches to the modelling of cancellous bone have been investigated. These methods - including the homogenisation method - attempt to quantify the influence of the microstructural variations on the global behaviour of cancellous bone. These techniques are discussed in Chapter 3.

### 1.3 OBJECTIVES

The objectives of the research project were as follows:

- To implement the homogenisation method in a three dimensional finite element code.
- To carry out numerical tests to investigate the levels of accuracy produced by the homogenisation method in the analysis of highly porous materials with structural and material properties similar to those of cancellous bone.
- To develop realistic idealised models of cancellous bone microstructure based on the observations and experimental evidence of previous research.
- To analyse the idealised models using the homogenisation method to find the apparent material properties and to compare these results to the accumulated pool of experimental evidence.
- To draw conclusions about the viability of developing idealised numerical models of cancellous bone which reasonably approximate the microstructural architecture and exhibit similar mechanical behaviour to that of actual cancellous bone.
- To draw conclusions about the viability of applying the homogenisation method to the numerical modelling of cancellous bone in order to predict, reasonably accurately, the macro- and microstructural behaviour of cancellous bone in large global problems.

## **1.4 PLAN OF THIS THESIS**

In this chapter, the need to model the microstructural behaviour of cancellous bone, and the problems associated with this task have been introduced. Chapter 2 presents the findings of a comprehensive literature study of the work which has been done on the mechanical properties and morphological nature of cancellous bone. In Chapter 3 the homogenisation method is introduced. Different techniques which have been used to model cancellous bone are first discussed, and the advantages of the homogenisation method are presented. The theory of homogenisation and its implementation within a three dimensional finite element code are then documented. The last part of Chapter 3 presents the results of numerical trials which have been conducted to assess the accuracy of the homogenisation technique under conditions which are characteristic of trabecular bone geometry and environment (e.g. high void fractions, thin-walled/fibred structures, compressive and shear loading, and bending and compressive modes of deformation). Chapter 4 presents the work done on the development of idealised finite element models of cancellous bone. The more important aspects, highlighted in Chapter 2, which characterise the physical properties and behaviour of cancellous bone from the proximal tibia (lower knee) have been taken into account when developing idealised microstructures for this region. The numerical models have been analysed using the homogenisation method to find the apparent material properties. These continuum-level properties have been compared to experimentally measured values from the literature. Having developed suitable models of cancellous bone which exhibit similar orthotropic properties to actual bone, a simple global model of a cementless reconstructed knee joint was set up to investigate the differences in the overall behaviour of the joint when the cancellous region is modelled as an orthotropic material compared to an isotropic material. Finally, in Chapter 5, conclusions are drawn about the viability of developing realistic idealised models of cancellous bone, as well as the feasibility of using the homogenisation method to predict the microstructural behaviour of these idealised cancellous bone models.

---

## CHAPTER 2

# CANCELLOUS BONE

---

This chapter contains an overview of the literature on the mechanical behaviour, structural characterisation, and idealised modelling of cancellous bone.

Considerable research has been done on this topic over the last 30 years. The fundamental issues pertaining to the understanding of the morphology or microstructure as well as the mechanical behaviour of cancellous bone have been addressed by various researchers, and there is now general agreement on most of these issues. There is certainly conclusive empirical evidence that there are a large number of interrelated factors which affect the material behaviour of cancellous bone. These include trabecular architecture, degree of anisotropy, degree of porosity, solid phase material properties, and modes of bone fibre or trabecular deformation. It is crucial that these important factors are well characterised when developing idealised representative models of cancellous bone in order to predict the macro- and microstructural behaviour of bone with a reasonable degree of accuracy.

A realistic idealised model of cancellous bone, must exhibit the same typical mechanical behaviour as that of the actual bone which is being modelled. A good quantitative measure of how well a structural bone model approximates the apparent mechanical behaviour of actual bone is the correlation of apparent stiffness. The apparent moduli (three values for orthotropic bone) of the numerical model, which can be calculated using the homogenisation method, can be compared to experimentally measured values of test specimens. The apparent level values of Poisson's ratio (which are also calculated by the homogenisation analysis, but which are difficult to measure experimentally) can also be compared. However, accurate correlation of these second order Poisson effects is less important than achieving close agreement of the triaxial moduli.

In the following sections, some of the more important aspects which affect the apparent stiffness, and which must therefore be taken into account when developing numerical models of cancellous bone, are discussed.

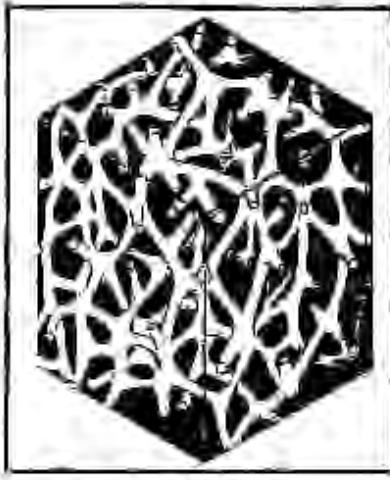
## 2.1 MORPHOLOGICAL/ARCHITECTURAL CHARACTERISTICS OF CANCELLOUS BONE

The architectural characteristics of cancellous bone microstructure are highly region-dependent. The different bones in the body perform different load-bearing functions, and the resulting variations in stress environment in the underlying cancellous regions lead to variations in structure, orientation and density from one anatomic location to the next.

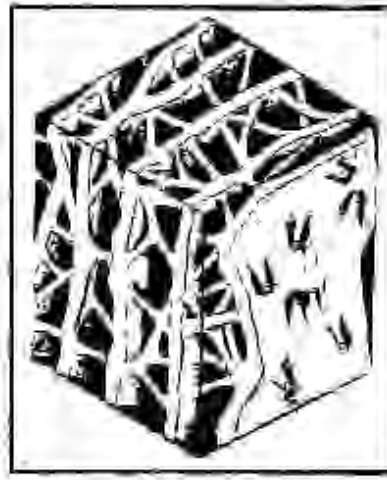
Cancellous bone is generally anisotropic because of the preferred orientations of the trabeculae. Many studies on trabecular architecture have been undertaken. (Amstutz and Sissons (1969), Whitehouse and Dysen (1974), Townsend *et al.* (1975), Singh (1978), Gibson (1985), Snyder and Hayes (1990), Mosekilde (1993)). While these studies have all lead to the conclusion that cancellous bone morphology can not be generalised for all regions of bone, there is consensus that the distinctive structures of cancellous bone from different anatomic regions can be classified into general groups. Although a particular region of bone will exhibit typical microstructural characteristics, there will always be a high degree of randomness in the structure, orientation and size of any one trabecula within that region.

Singh (1978) did a comprehensive study of cancellous bone from various parts of the human skeleton and concluded that cancellous bone can be classified into three main types, each with a number of sub-categories. Some of the more regularly structured types of bone, which occur in the more important load-bearing regions and can be more readily idealised, are described below.

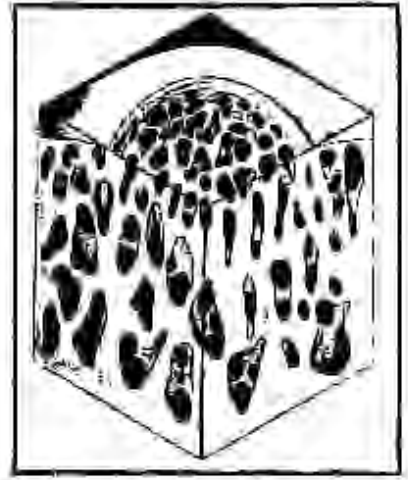
The first type of cancellous bone described by Singh (TYPE I) comprises a delicate three-dimensional meshwork of straight or curved rod-type trabeculae, with no preferential orientations. The rods are typically 0.08-0.14mm in diameter and about 1mm in length. This type (illustrated in Figures 1.2 and 2.1a) occurs in the deeper parts of the ends of long bones. The second type (TYPE II) which is divided into three subtypes is made up of a combination of rods and plates. This type ranges from a meshwork similar to TYPE I where some of the rods have been replaced by delicate plates of bone, to a meshwork which consists almost entirely of plates. In this latter case, the larger plates have many fenestrations (or holes) to interconnect the marrow cavities. Subtype IIc, which occurs typically at the distal end of the femur, exhibits a particularly specific arrangement of trabeculae (Figure 2.1b). It consists mainly of thick plates (0.16-0.3mm thick) arranged parallel to each other in 0.4-0.8mm intervals. The plates are orientated at right angles to the articular surface, and the parallel formations can be maintained for up to a centimetre in length. Transverse rods span the spaces between the parallel plates and appear to hold the plates apart. TYPE III - also divided into three subtypes - describes cancellous bone which is made up entirely of plates of varying size and shape with many small perforations. This type of bone occurs in a range of densities, and may or may not exhibit preferred trabecular orientations. Subtype IIIb, occurring at the ends of the tibia - close to the articular surfaces - and in the lower vertebrae, resembles TYPE IIc. However the parallel plates are more delicate than in TYPE IIc (0.12-0.24mm thick) and the transverse rods are now replaced by more plates - thus forming tubular or cylindrical type structures (with diameters of 0.7-2.00mm) which are vertically orientated along the longitudinal axis of the bone, which is the axis of maximum compressive stress. These cylindrical



2.1a TYPE I

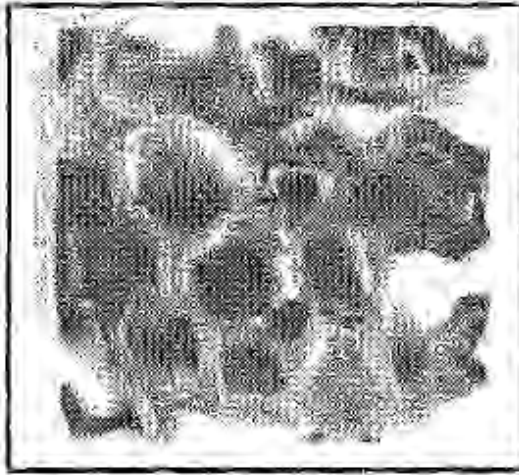


2.1b TYPE IIc



2.1c TYPE IIIc

FIGURE 2.1 Three types of cancellous bone (Singh, 1978)

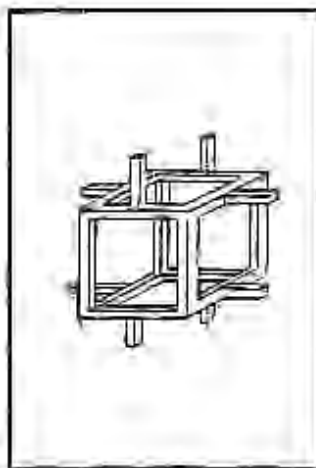


2.1c Transverse cut

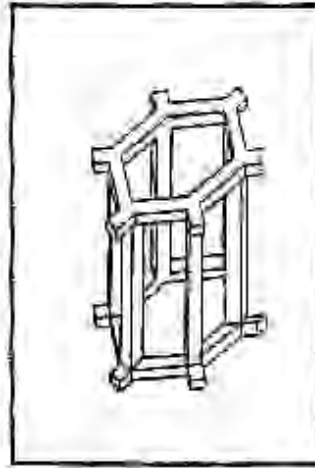


2.1d Vertical cut

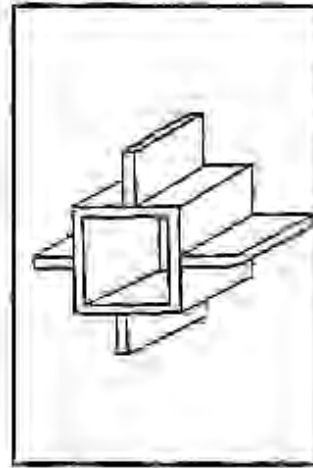
FIGURE 2.1 (cont.) TYPE IIIb bone specimen from the proximal tibia (Williams and Lewis, 1982)



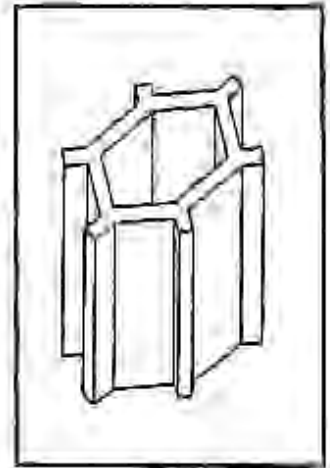
2.2a Asymmetric open cell



2.2b Columnar open cell



2.2c Asymmetric closed cell



2.2d Columnar closed cell

FIGURE 2.2 Analytical idealised models of cancellous bone (Gibson, 1985)

arrangements are seen in the transverse and vertical cuts of an actual bone specimen in Figures 2.1d and e. Subtype IIIc, which occurs beneath articular surfaces (e.g. in the femoral head, upper cervical vertebrae and in the patella), consists of dense cancellous bone with thick walls (0.2-0.4mm) enclosing spaces 0.4-0.6mm across. Just below the articular surfaces, there appear to be no preferential orientations (Figure 2.1c). However, further away, the intertrabecular spaces become much larger and elongated in the direction perpendicular to the articular surface, gradually approaching the structures of TYPES IIc and IIIb. A summary of Singh's categorisations of cancellous bone is given in Table 2.1

**TABLE 2.1 Summary of Singh's (1978) categorisations of cancellous bone**

| TYPE | LOCATION                                                                                            | DESCRIPTION                                                                                                                                                                                                        |
|------|-----------------------------------------------------------------------------------------------------|--------------------------------------------------------------------------------------------------------------------------------------------------------------------------------------------------------------------|
| I    | deeper parts of long ends of bones                                                                  | meshwork of 0.08-0.14mm diameter rods<br>no preferential orientations                                                                                                                                              |
| IIa  | long ends of bones                                                                                  | low density meshwork of rods and plates 0.1-0.2mm thick and 1mm long                                                                                                                                               |
| IIb  | calcaneum                                                                                           | similar to TYPE IIa but with larger plates up to 0.5mm thick and several millimetres long, with numerous fenestrations, and interconnected with rods                                                               |
| IIc  | lower end of femur, close to articular surfaces                                                     | parallel plates 0.16-0.3mm thick and up to 10mm long, running perpendicular to articular surface, separated by transverse rods 0.4-0.8mm long                                                                      |
| IIIa | -                                                                                                   | similar to TYPE IIa but with plates only - 0.1-0.2mm thick and 1mm long, interconnecting fenestrations                                                                                                             |
| IIIb | ends of tibia - adjacent to articular surfaces, widely distributed in the skeleton, lower vertebrae | similar to TYPE IIc, delicate construction of plates 0.12-0.24mm thick vertically orientated to form tubular structures with interconnecting holes                                                                 |
| IIIc | directly beneath articular surfaces, femoral head                                                   | solid mass of bone, fenestrated by numerous interconnecting spaces, thick plates 0.2-0.4mm, no preferential orientations close to articular surface, but further away spaces become elongated changing to TYPE IIc |

Singh's work provides a good departure point from which to set about developing idealised models of cancellous bone. Subsequent studies have confirmed the existence of these various categories (Williams and Lewis (1982), Gibson (1985), Rice *et al.* (1988)). However, it has become clear that even within one region of bone, there is a significant level of variation in the trabecular microstructure. Williams and Lewis (1982) made observations regarding the structure of cancellous bone from the proximal tibia, and identified three general structural types in this region alone. These three categories; rod-rod, plate-rod and plate-plate, coincide roughly with Singh's TYPES I, IIc, and IIIc, respectively. Williams and Lewis noted that the three types of bone are all related and not always distinct. They also observed that all the cancellous bone in this region tends to form cylindrical arrangements in the vertical direction, as can be seen in Figures 2.1d and 2.1e. This concurs with Singh's observations.

Gibson's (1985) descriptions of the structure of cancellous bone are somewhat simpler than those of Singh and Williams and Lewis. She has divided cancellous bone into four distinct categories for the purpose of developing idealised analytical models of bone. The structure of bone has been categorised according to the predominant type of trabecular member (rod-like or plate-like), and according to whether these trabecular members have preferential orientations or not (columnar or asymmetric). The four types are:

- 1: asymmetric open cell, rod-like
- 2: columnar open cell, rod-like
- 3: asymmetric closed cell, plate-like
- 4: columnar closed cell, plate-like

The open cell structures describe bone which has apparent densities of typically less than 0.13, and closed cell structures represent bone with apparent densities above 0.2. These definitions stem from work done by Whitehouse and Dysen (1974) who did comprehensive studies on femoral head trabecular bone morphology and who categorised bone in this manner based on their observations. In categorising bone into these four distinct groups, Gibson's aim was to make predictions regarding the dependence of compressive stiffness on apparent density based on the assumed modes of trabecular deformation (bending or axial compression). These predictions (discussed in the next section) are useful in identifying predominant modes of deformation for different types of cancellous bone structure. However, Gibson's actual analytical bone models corresponding to the four distinct bone types, (Figures 2.2a-d), are perhaps too simplistic for the purposes of developing realistic finite element models of cancellous bone structure. Rice *et al.* (1988) suggest that trabecular bone microstructure is generally more realistically idealised as some combination of the open and closed cell models. Gibson has not categorised this intermediate (and apparently more prevalent) bone microstructure which consists of combinations of rod- and plate-like members, with apparent densities between 0.13 and 0.25.

## **2.2 EXPERIMENTAL EVIDENCE - THE RELATIONSHIP BETWEEN APPARENT MECHANICAL PROPERTIES, TRABECULAR DEFORMATION MODES AND APPARENT DENSITY**

### **2.2.1 EXPERIMENTAL METHODS**

Before reporting on some of the experimental work that has been done on cancellous bone by previous investigators, it is necessary to consider the possible causes of discrepancy in results and conclusions drawn. It is extremely difficult to correlate data from different studies because of the large number of variables which have to be kept constant in order to make meaningful comparisons. A number of different methods have been used to measure the compressive modulus of cancellous bone. The choice of experimental methodology will generally have a significant influence on the results owing to the different assumptions which are inherent in each experimental method. To trace any inconsistent results and conclusions from different studies directly to the different experimental procedures is difficult since variations in results can, in part, be attributed to variations in actual bone morphology from one test specimen to the next - from region to region and from person to person. However, discrepancies which can be attributed to variations in experimental procedures have been investigated by several researchers, and their results are briefly discussed here.

The more important aspects which influence the results of experimental tests are: the treatment of bone prior to testing, the specimen size and geometry, and the testing method (e.g. confined or unconfined tests, compression, tensile, or ultrasonic testing, and the testing strain rate).

Some investigators dry their bone specimens, others test them fresh or freeze them first, others dry, defat and rewet the specimens before testing. It is generally accepted that bone that has been dried prior to testing will be stiffer than bone which is tested fresh (Rice *et al.* (1988), Goldstein (1987)).

The choice of specimen size and geometry has a significant influence on experimental results. The machining of bone specimens to size will necessitate the interruption of the trabecular network at the specimen ends. Thus, even if the actual trabecular tissue is not damaged during machining, the end effects will result in an underprediction of the true compressive stiffness. Keaveny *et al.* (1993) performed a theoretical analysis to characterise these end effects (called damage artefacts) for different specimen shapes and sizes. Their theory predicted an underestimation of Young's modulus by 45-75% (depending on the specimen platen lubrication) for 6mm cubic specimens. They found that cylindrical specimens with aspect ratios of 2:1 provided the most accurate results when conducting compression tests.

Gibson (1985) reported that the use of a confining ring when performing uniaxial compression tests on cylindrical specimens will result in data being higher by a factor of about one third than the corresponding results for unconfined tests.

The effect of experimental strain rate on the results of compression tests on cancellous bone was investigated by Carter and Hayes (1977) and later by Linde *et al.* (1991). Both these groups of researchers performed compression tests on cylindrical bone specimens from human tibia for a range of strain rates. Carter and Hayes found that the measured stiffness varied with strain rate to the 0.06 power. The corresponding value found by Linde *et al.* was 0.047. This reasonably close agreement indicates that the effect of testing strain rate is relatively small provided the strain rates are not too high.

### 2.2.2 EXPERIMENTAL AND ANALYTICAL RESULTS

The experimental evidence that is reported and discussed in this section concentrates mainly on results from studies for cancellous bone in the proximal tibial region. It is this type of bone that is modelled numerically in Chapter 4.

Many studies have shown that the apparent density of cancellous bone is a very good first order predictor of compressive modulus (Goldstein (1987), Rice *et al.* (1988), Snyder and Hayes (1990), Linde *et al.* (1991), Keaveny *et al.* (1994)). These studies have all attempted to find empirical relations between the apparent density and the compressive modulus of bone. There has been some debate about whether stiffness is a linear or an exponential function of apparent density and it appears that there is no specific power law function which relates these two variables for all types and regions of cancellous bone. A general form of these functions is as follows:

$$E = A \rho^B + C \quad (2.1)$$

where

- E is the apparent or bulk compressive modulus
- $\rho$  is the apparent density
- A is a proportionality constant
- B is the power coefficient, and
- C is the "function intercept"

### The Physical Meaning of B

It is generally accepted that the predominant mode of deformation of the trabeculae, for loading in a particular direction, will directly influence the power law relation between apparent density and apparent stiffness in that direction. However, it appears that the relationship between the deformation modes and the value of B is not fully understood. In order to interpret the physical meaning of B it is useful to compare a linear and power law regression fit to one set of data as shown in Figure 2.4 (the regression relations for these two curves are listed in Table 2.2 at the end of this section). If the trabecular structures deform purely by axial compression with no bending, then the apparent stiffness of a representative volume of bone would simply be the solid volume fraction in the transverse plane multiplied by the solid volume stiffness. For this linear relation,  $B = 1$ . If the trabeculae deformed by some combination of bending and axial compression then the amount of bending relative to the amount of axial compression would vary depending on the level of porosity. Snyder and Hayes (1990) have shown that increases in apparent density of cancellous bone translates to increases in trabecular thickness, implying reduced slenderness and thus reduced trabecular bending. Thus at low densities, there would be significant bending of the thin trabecular fibres under compressive loads. In this range, an increase in apparent density would result in a smaller increase in stiffness than that for a trabecular structure which deforms predominantly by axial compression. And so, at low densities, the slope of the E versus  $\rho$  curve for the bending model would be less than the slope for the purely axial compressive model. However, at higher densities the gradual reduction in bending would result in a more dramatic increase in stiffness for an increase in apparent density compared to the purely axial compressive model. Hence, at higher densities the slope of the regression curve of the combined bending and compressive model would be greater than that for the purely compressive model. A power law regression curve relating E to  $\rho$  for any  $B > 1$  will exhibit the required increasing slope with increasing density which would be characteristic of the combined bending and compressive model.

This interpretation implies that the magnitude of B is not necessarily a measure of how much bending occurs at any particular level of porosity, but rather a measure of the extent to which the predominance of bending deformations, relative to axial compressive deformations, changes from low density to high density regions. Thus a low value of B (close to 1) does not necessarily indicate that the degree of bending deformations is low but rather that the degree of bending - be it high or low - does not vary considerably over the range of densities measured. It is important to consider the range of densities that are included in the regression fit when interpreting the value of B. Only when the full range of densities has been tested can conclusions be drawn with confidence about the actual degree of bending on the basis of the magnitude of B.

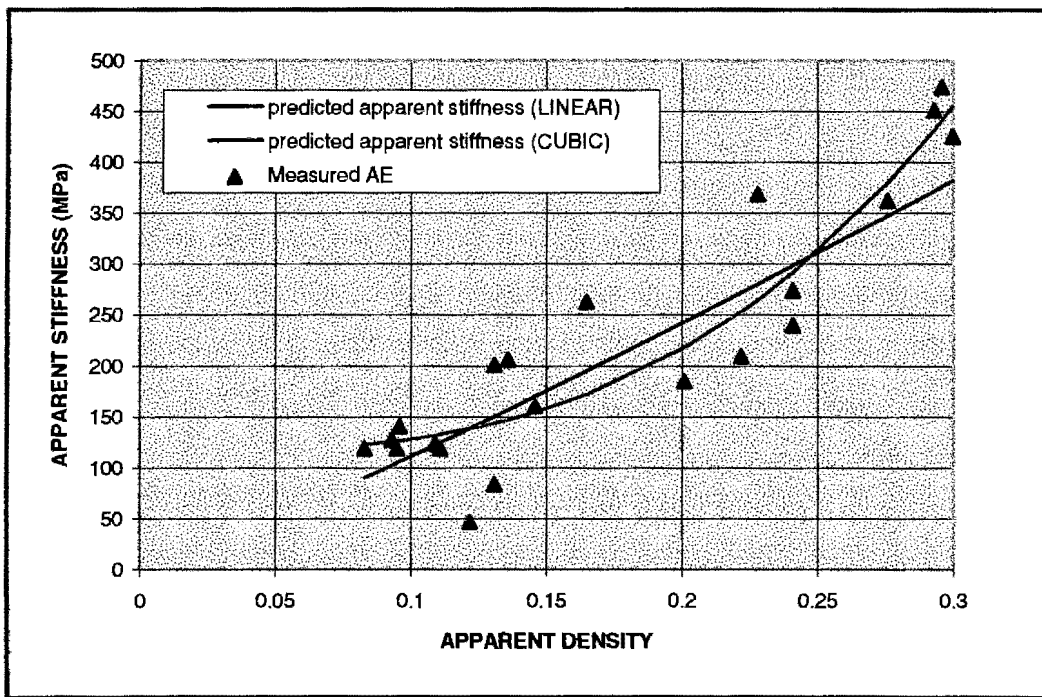


**FIGURE 2.4** Cubic and linear regression curves to data for apparent vertical stiffness of proximal tibial cancellous bone. Data from Williams and Lewis (1982)

Gibson (1985) made analytical predictions of power law functions for different types of cancellous bone and for different deformation mechanisms by using her simple analytical models of cancellous bone. She showed that, under the assumption that bending is the major mode of deformation, Young's modulus should vary with the square of density for open cell structures ( $\rho < 0.2$ ) and with the cube of density for closed cell structures ( $\rho > 0.2$ ) if these structures are both asymmetric. For columnar type structures, where axial compression is assumed to be the major mode of deformation, Gibson predicted a linear relation. These analytical predictions appear to agree reasonably well with the experimental results of Carter and Hayes (1977) Williams and Lewis (1982) and Ashman and Rho (1988). However, some of the assumptions that have been made - both in the experimental procedures, and in the correlation of the experimental data according to assumed functions - are perhaps simplistic.

Carter and Hayes (1977) conducted compression tests on 100 cylindrical bone specimens from the human proximal tibia and 24 specimens from the bovine distal femur for a range of apparent densities. They combined their data for bovine and human bone to calculate one regression relation. It is presumed that the data was combined in order to have a wider range of densities for analysis, although the justification for doing this has subsequently been refuted in the literature (Rice *et al.* (1988), Ashman and Rho (1988)). The test specimens, which were kept fully moist, were orientated with their axes parallel to the long axis of the bone. Carter and Hayes used the confined uniaxial compression test on these specimens. They fitted a least squares linear regression curve to the log of apparent density versus the log of apparent compressive modulus. In this way, they were able to measure the variables A and B in Equation (2.1). They made the assumption that C is zero, thus forcing their regression curve to go through the origin. This assumption does seem reasonable, since one would expect the stiffness at zero density to be zero as well. The structural characteristics of cancellous bone do, however, vary according to the

degree of porosity. And so it is possible that the relationship between apparent stiffness and apparent density will not be constant over the whole range of densities. However, if the changes in microstructural architecture are gradual over the range of apparent densities, then it is reasonable to assume that one smooth relationship will apply over that range. Carter and Hayes have no data for apparent densities below 0.1, thus the validity of extrapolating their data to zero density is perhaps questionable. They have provided no information on the coefficient of correlation or level of significance of this analysis, and they have evidently not investigated other possible regression functions. From their results (listed in Table 2.2), Carter and Hayes conclude that the compressive modulus of cancellous bone in the proximal tibia is proportional to the cube of apparent density. This implies that, although the trabeculae in the proximal tibia are highly orientated along the vertical axis, they do deform by some bending when subjected to axial compressive loading in this direction. According to the previously discussed interpretation of B, the high value of 3 is an indication that bending effects are considerably reduced at higher densities.

Gibson (1985) subsequently cited Carter and Hayes' data in support of her analytical predictions. However, she separated the data into two groups. The first contained only bovine data for bone with apparent densities above 0.2. The second group contained all the remaining bovine data and all the human bone data. The two regression curves for these two groups indicate that the power law exponent, B, changed from 2 to 3 at an apparent density of about 0.2 which is in agreement with Gibson's analytical predictions for open and closed cell asymmetric models. However, this observed transition at a density of 0.2 is not necessarily true for one particular region of human bone since all the data for the range of apparent densities above 0.2 was taken from bovine distal femora (not human proximal tibia). Gibson also ignored the possibility that the best fit to the high density data might not go through the origin, and no information on the correlation of the data has been given.

Williams and Lewis (1982) conducted compression tests on 5-6mm cubes of cancellous bone from the human proximal tibia. The specimens were defatted, dried and rewetted, and were tested in three orthogonal directions for stiffness. A linear curve was fitted to the data of stiffness in the vertical direction versus estimated apparent density, with a correlation coefficient squared of  $r^2 = 0.81^*$  (see Appendix A). However, they found no significant linear correlation between stiffness and apparent density in the transverse directions (Rice *et al.* (1988) subsequently fitted a quadratic curve to this data for transverse stiffness). Williams and Lewis concluded from their analysis that in the vertical direction, the major mode of deformation is axial compression, while bending is predominant in the transverse directions. Their linear regression curve for axial loading differs from Carter and Hayes' exponential relations for the same region of cancellous bone. However, it appears that Williams and Lewis made no attempt to fit an exponential curve to their data.

---

\*  $r$  is the coefficient of correlation for a linear regression analysis. The value  $r^2$  indicates what proportion of a variation in  $y$  (apparent stiffness, in this case) can be attributed to the least squares linear relationship with  $x$  (apparent density) - Miller and Freund (1985).

---

On the assumption that the trabeculae in the proximal tibia do deform predominantly by axial compression, Williams and Lewis calculated the corresponding Young's modulus of the trabecular tissue by dividing the measured stiffness along the vertical axis by the area fraction of their cubic specimens. The resultant tissue stiffness was 1.3 GPa which is considerably lower than the more realistic value of about 5 GPa for trabecular bone (Choi *et al.* 1990). And so, in spite of their good correlation using a linear regression fit, the basis for their conclusion that the trabeculae in the proximal tibia deform predominantly by axial compression in the vertical direction is somewhat tenuous. A further statistical analysis of the data of Williams and Lewis has revealed that although a linear regression curve does indeed give a correlation of  $r^2 = 0.81$ , the best fit to this data is for a power coefficient of 3 ( $r^2 = 0.85$ ). Alternatively, by forcing the regression curve to go through the origin, a much lower exponent of 1.12 is predicted with  $r^2 = 0.82$ . This lower exponent is probably more realistic since the apparent stiffness intercept for the cubic fit is 115 MPa which is very high. The cubic and original linear regression curves are compared graphically in Figure 2.4 and the corresponding predicted expressions are listed in Table 2.2.

As discussed, the work of Keaveny *et al.* (1993) suggests that Williams and Lewis' measured values of stiffness for their range of specimens were probably underestimated by at least 45% owing to the shape and size of their bone specimens. However, their results have proven useful in this study because they have reported actual measured values of apparent stiffness in both the longitudinal and transverse directions for all their bone specimens. For lack of similar data from more recent studies, this data has been used as a benchmark for comparison to the numerical results of this study. Although the predicted systematic errors in the measured data values have been taken into account when assessing the numerical predictions, it is the ratio of transverse to longitudinal stiffnesses that has been of more value in this study.

Williams and Lewis (1982) found that the average ratios of vertical to lateral stiffness were between 3 and 4 for highly orientated trabecular bone such as that found in the proximal tibial region. Thus they have concluded that density alone, being a scalar property, cannot be the only indicator of stiffness, since stiffness varies with direction because of preferred trabecular orientations and different deformation modes.

The fact that a high percentage of the variance in apparent stiffness in the vertical direction can be accounted for by the corresponding variance in apparent density using both a linear and cubic regression curve for Williams and Lewis' data indicates that there is perhaps too much scatter in the data and not enough data to conclude categorically what the true relation between apparent stiffness and apparent density is for this sample of cancellous bone. However, there is certainly strong evidence that would suggest that the vertical trabeculae in the proximal tibia do indeed deform by some degree of bending under axial compressive loading, and not purely by axial compression.

More recent studies on cancellous bone from the proximal tibia, using more accurate experimental techniques (Linde *et al.* (1985, 1988, 1991), Hvid *et al.* (1989)) have reported power law relations between apparent vertical stiffness and apparent density with lower exponents. Table 2.2 lists a range of results from all the different studies on cancellous bone in this region. These results suggest that B in Equation (2.1) is perhaps more realistically in the range of 1-2 than 2-3 for cancellous bone in the proximal tibia.

For cancellous bone in the distal femur, there is not as much experimental evidence as for the proximal tibia. Ashman and Rho (1988) used an ultrasonic technique to measure the elastic modulus of cancellous bone and trabecular bone material in 53 cylindrical specimens taken from three human distal femora. The ultrasonic technique makes use of piezoelectric transducers applied directly to the bone specimens to transmit and receive elastic waves. The apparent modulus,  $E$ , is calculated from the equation:

$$v = \sqrt{\frac{E}{\rho}} \quad (2.2)$$

where  $v$  is the acoustic velocity  
and  $\rho$  is the material density

This technique for the calculation of  $E$  was previously validated by these authors where their results correlated well with mechanical tension tests. They found  $E_{\text{mech}} = E_{\text{ultrasonic}} + 23.3 \text{ MPa}$  where  $r^2 = 0.935$ , for 15 samples.

The distal femur, like the proximal tibia, is a relatively anisotropic region with preferred trabecular orientations along the longitudinal axis. The cylindrical test specimens were cut approximately parallel to the general orientation of local trabeculae, and so the measured stiffness values correspond approximately to the longitudinal axis. Ashman and Rho initially conducted a linear regression analysis between apparent density and apparent modulus for their experimental data and achieved a high correlation ( $r^2 = 0.93$ ). However, they improved  $r^2$  to 0.95 by fitting an exponential curve where  $E$  was found to be related to apparent density raised to the power 1.88. For this exponential regression, the curve was again forced to go through the origin. The average apparent density of the test specimens was about 0.19. This region of bone, corresponds to Singh's TYPE IIc (thick parallel plates in the longitudinal direction held apart by numerous transverse rod-like trabeculae). The predicted compressive stiffness from Ashman and Rho's exponential regression curve is 1.9 GPa at the average apparent density. This value is 430% higher than the adjusted predicted value from Williams and Lewis' (1982) data for the same apparent density in the proximal tibial region. This result suggests that considerably less trabecular bending occurs in the distal femur than in the proximal tibia. This can be explained by the fact that the vertically orientated plate-like structures in the distal femur are thicker and are more preferentially orientated than those in the proximal femur. In addition, the transverse rods tend to limit the bending of the plates and prevent them from buckling. The apparent moduli in the transverse directions were not measured in this study.

Similar tests on bovine distal femora were conducted by these authors who found different power law correlations between apparent density and apparent stiffness to those found for human bone. Thus, cancellous bone from different specimens should not be combined in an attempt to find one general regression correlation for different species. This fact was confirmed by Rice *et al.* (1988) who conducted a statistical analysis of pooled data from previous experiments by various researches (including Cater and Hayes (1977), and Williams and Lewis (1982)).

Rice *et al.* investigated the relationship between apparent density and apparent modulus using the accumulated data. They proposed three possible models for this relationship; namely, a quadratic, cubic, and quadratic plus cubic model. The data sets were all different with respect to species, direction, and test conditions and procedures, and so the authors created indicator variables which were included in the regression equations in order to compare these three models while controlling for data group membership. The indicator variables accounted for species (bovine or human), sample specimen orientation, tension or compression testing, and confined, unconfined or indentation testing protocols. The data was all adjusted to one equivalent testing strain rate ( $0.01 \text{ s}^{-1}$ ) using Carter and Hayes power law relation between strain rate and apparent density. No differentiation was made for bone from different regions of the body. Rice *et al.* found that the quadratic model fitted the data most accurately and effectively; with a variance in  $\rho$  accounting for 78% of the variance in E. However their regression relations for transverse stiffness in human bone which was calculated on the basis of extrapolated bovine data, predicted a negative dependence of compressive modulus on the square of apparent density. It is acknowledged by the authors that this can not be correct, and it is perhaps an indication that there was not sufficient data to find accurate relations between all the different control groups. In addition, one can deduce from this that the anisotropic effects of bovine bone are different from those of human bone. Bovine data can therefore not be combined with human data in an attempt to find one specific relation between apparent density and apparent modulus.

Rice *et al.* conclude that on the basis of the good correlations which they found, the apparent Young's modulus for cancellous bone is proportional to the square of apparent density for all cancellous bone, and that the different specific relations are dependent on species, direction and stress type. They also suggest that the particular region of bone does not affect the apparent modulus. However, there is no real basis for this last conclusion. Their data for human bone comes from the studies of Carter and Hayes and Williams and Lewis which were both on the proximal tibia, and so generalisations about the mechanical behaviour of all types of cancellous bone cannot be made based solely on these results.

Table 2.3 lists the reported ranges of measured apparent stiffnesses in the proximal tibia and distal femur from various studies. The reported values for the distal femur are all considerably higher than those for the proximal tibia.

**TABLE 2.2 Regression results from experimental data of apparent stiffness (E) versus apparent density ( $\rho$ )**

| Authors                           | Year | Specimen Geometry | Predicted E (MPa)                        | $r^2$ | E @ $\rho = 0.2$ | Comments                                                         |
|-----------------------------------|------|-------------------|------------------------------------------|-------|------------------|------------------------------------------------------------------|
| Carter & Hayes                    | 1977 | 5/21mm cyl*       | $23000\rho^3$                            |       | 184              |                                                                  |
| Williams & Lewis                  | 1982 | 5-6mm cube*       | $1500\rho - 40$ †                        | 0.81  | 260              | strain rate: $0.005s^{-1}$<br>specimens dried and rewetted       |
|                                   |      |                   | $12583\rho^3 + 115$ †                    | 0.85  | 216              |                                                                  |
|                                   |      |                   | $1760\rho^{1.12}$                        | 0.82  | 290              |                                                                  |
| Gibson (data of Carter and Hayes) | 1985 | 5/21mm cyl        | $E \propto \rho^2$<br>$E \propto \rho^3$ |       |                  | $\rho < 0.2$ (bending)<br>$\rho > 0.2$ (bending)                 |
| Klever et al.                     | 1985 | 8mm cube          | $11600\rho^{1.5}$                        |       | 1038             |                                                                  |
| Linde et al.                      | 1988 | 7.5/7.5 cyl       | $7092\rho^{1.47}$                        |       | 666              |                                                                  |
| Ashman and Rho                    | 1988 | 15/5 cyl          | $18880\rho - 1480$                       | 0.93  | 2296             | <u>distal femur</u><br>fresh specimens<br>ultrasonic test method |
|                                   |      |                   | $43863\rho^{1.88}$                       | 0.95  | 2128             |                                                                  |
| Rice et al.                       | 1988 |                   | $3280\rho^2 + 70$                        | 0.78  | 201              | combined data of Carter & Hayes and Williams and Lewis           |
| Linde et al.                      | 1991 | 8.25/5.5 cyl      | $5300\rho^{1.56}$                        | 0.71  | 430              |                                                                  |

\* cyl => cylindrical specimens, cube => cubic specimens

† => linear fit, and ‡ => cubic fit to Williams and Lewis' (1982) data - plotted in Figure 2.4

Unless stated otherwise, all results are for cancellous bone from the proximal tibia, using compressive testing at a strain rate of  $0.01s^{-1}$ ; storage method: fresh frozen.

**TABLE 2.3 Experimentally measured values of apparent modulus**

| Authors          | Year | Location       | Specimen Geometry | Range of Apparent Modulus (MPa) | Comments               |
|------------------|------|----------------|-------------------|---------------------------------|------------------------|
| Carter & Hayes   | 1977 | Proximal Tibia | 5/21mm cyl        | 10 - 500                        |                        |
| Williams & Lewis | 1982 | Proximal Tibia | 5-6 mm cube       | 45 - 476                        | vertical<br>transverse |
|                  |      |                |                   | 8 - 130                         |                        |
| Goldstein et al. | 1983 | Proximal Tibia | 10/7 mm cyl       | 4 - 430                         |                        |
| Ciarelli et al.  | 1986 | Proximal Tibia | 8 mm cube         | 5 - 552                         |                        |
| Pugh et al.      | 1973 | Distal Femur   | 5/9.5 mm cyl      | 413 - 1516                      |                        |
| Ducheyne et al.  | 1977 | Distal Femur   | 8/5 mm cyl        | 59 - 2947                       |                        |
| Ciarelli et al.  | 1986 | Distal Femur   | 8 mm cube         | 8 - 800                         |                        |
| Ashman and Rho   | 1988 | Distal Femur   | 15/5 cyl          | 571 - 3240                      |                        |

Results for both vertical and transverse directions unless otherwise stated.

### 2.2.3 DISCUSSION

The experimental and analytical results of Carter and Hayes (1977), Williams and Lewis (1982), Gibson (1985), Ashman and Rho (1988), Rice *et al.* (1988), and Linde *et al.* (1988, 1991) attest to the fact that there is a large degree of variability in the mechanical behaviour of cancellous bone in regions such as the proximal tibia and proximal femur. Despite these variations, (caused not only by actual random variations in cancellous bone, but also by significant differences in experimental procedure) there appears to be consistent evidence that the relationship between apparent stiffness in the vertical direction and apparent density is exponential with a power exponent of between 1 and 3. This would indicate that the trabeculae in these regions do deform by some degree of bending in the vertical direction under compressive loading. Axial compression is thus not necessarily the predominant mode of deformation (especially not at lower densities) - even though the trabeculae in these regions are highly orientated in the direction of principal loading. Considering the high impact loads that the knee has to endure during normal daily activities, one would expect the cancellous bone under the articulating surfaces to exhibit some impact absorption capabilities as well as good strength characteristics. The various reported values of apparent modulus for the distal femur are much higher than those for the proximal tibia for the same range of apparent moduli. This would suggest that the trabeculae in the distal femur bend less than those in the proximal tibia. The fact that the trabecular plates are thicker and more highly orientated in the vertical direction in the distal femur compared to the proximal tibia, supports this theory. This needs to be taken into account when designing numerical idealised models of cancellous bone for the two regions.

## 2.3 MATERIAL PROPERTIES OF SOLID PHASE TRABECULAR BONE

Since the last century, biomechanics researchers have debated the issue of the true solid phase material properties of trabecular bone tissue. Wolff (1892) proposed that the tissue properties of trabecular and cortical bone are the same. However, subsequent experimental evidence has shown that trabecular bone is somewhat less stiff than cortical bone. A possible reason for this difference is the fact that the turnover rate of cancellous bone (rate of bone renewal) is much faster than that of cortical bone which results in a drop in bone mineral content of approximately 20% (Ashman and Rho (1988)). In addition, the effect of surface flaws, localised regions of demineralisation, and general variations in tissue-structure within any single trabecula will all contribute to a reduction in the observed stiffness of the trabeculae. The reported values of trabecular tissue modulus range from 1.3 GPa (Williams and Lewis (1982)) to 16 GPa (Gibson (1985)). However, these investigators have not done actual tests on individual trabecular. Some of the reported values of tissue modulus measured by various investigators using various experimental techniques are listed in Table 2.4.

Choi *et al.* (1990) did three-point bending tests on machined trabecular and cortical specimens from the human proximal tibia and found that Young's modulus values dropped with decreasing specimen size. This was attributed to an increase in the weakening effect of surface variations and flaws with an increasing surface to volume ratio. Choi *et al.* found that the mean moduli for cortical specimens with thicknesses greater than 0.55mm remained fairly constant at about 15 GPa. For thicknesses from 0.55mm to 0.1mm the moduli decreased from 15 GPa to about 5 GPa. The mean modulus of trabecular specimens was found to be 4.6 GPa compared to a value of 5.4 GPa for the same sized cortical specimens, which constitutes a 19% increase.

Kuhn *et al.* (1989) and Mente and Lewis (1989) have also presented experimental evidence that trabecular fibres exhibit effective Young's moduli of around 5 GPa. Recent work on the numerical modelling of cancellous bone by Hollister *et al.* (1991, 1994) has shown a very good correlation between experimental data and numerical predictions of apparent cancellous bone behaviour when using a Young's modulus of 5 GPa and a Poisson's ratio of 0.3 to model the trabecular tissue.

**TABLE 2.4 Experimentally measured values of trabecular tissue modulus**

| Authors                | Year | Location     | Experimental Technique | Tissue Modulus (GPa) |
|------------------------|------|--------------|------------------------|----------------------|
| Townsend <i>et al.</i> | 1975 | Tibia        | Inelastic Buckling     | 11.4                 |
| Ku <i>et al.</i>       | 1987 | Tibia        | 3-Point Bending        | 3.17 (1.5)           |
| Choi <i>et al.</i>     | 1989 | Tibia        | 3-Point Bending        | 4.6                  |
| Choi                   | 1991 | Tibia        | 4-Point Bending        | 5.35 (1.4)           |
| Mente and Lewis        | 1987 | Tibia, Femur | Cantilever Bending     | 5.3 (2.6)            |
| Mente and Lewis        | 1989 | Tibia, Femur | Cantilever Bending     | 7.8 (5.4)            |
| Runkle and Pugh        | 1975 | Femur        | Buckling               | 8.7 (3.2)            |
| Ashman and Rho         | 1988 | Femur        | Ultrasonic test        | 12.7 (2.0)           |

Standard deviations in parenthesis

---

## CHAPTER 3

### THE HOMOGENISATION METHOD

---

This chapter begins with an overview of some of the numerical and analytical methods which have been used to model cancellous bone. The homogenisation method is then introduced and some of the advantages of this method are discussed. The next section describes the basic theory of homogenisation. Then the implementation of homogenisation within the finite element method is discussed. In the following section, numerical trials to test the homogenisation method are described and the results of these tests are presented. These trials were set up to gain an understanding of the levels of accuracy that can be expected when using the homogenisation technique to model the behaviour of highly porous media such as cancellous bone. Finally the results of these test problems are discussed.

#### 3.1 INTRODUCTION TO HOMOGENISATION

There are a range of techniques which attempt to model or simulate the microstructural influences of a composite material on its apparent global behaviour while treating the composite as a continuum on the global level. A number of researchers have investigated the application of these methods to the modelling of cancellous bone.

Hayes *et al.* (1981) investigated the possibility of applying the theory of mixtures for composite materials to cancellous bone. This approach involves calculating the continuum-level mechanical properties of the aggregate from the material properties and volume fractions of the constituent materials. Besides the fact that this method can not be used to predict local stresses within the composite, Hayes *et al.* found that this method predicts compressive stiffnesses for cancellous bone that are an order of magnitude too high. The reason for this is that the possibility of bending of the individual trabeculae within the bone composite is not considered and so, as discussed in the previous chapter, this leads to an overestimation of the stiffness.

Gibson and Ashby (1988) treated cancellous bone as a cellular solid. They suggested modelling cancellous bone as a continuum, using the orthogonal apparent moduli predicted by triaxial regression relations between apparent density and apparent stiffness. This would then take into account the bending behaviour of the individual trabeculae. This method does not facilitate the prediction of microstructural responses to global stress environments.

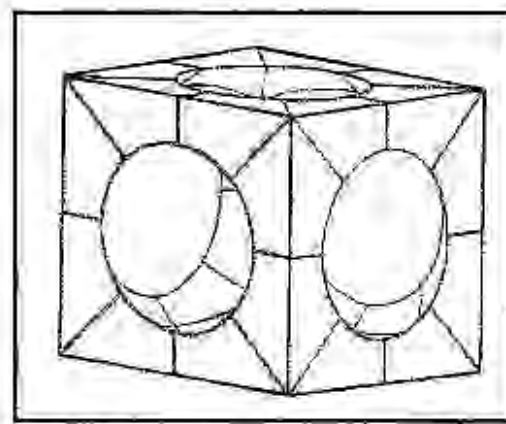
Beaupre and Hayes (1985) used the finite element method to predict the global response of an idealised model of cancellous bone. The model, a cube with a spherical void and 20% solid volume, was based on the observed architecture of an open-celled matrix

containing roughly spherical pores (Figures 3.1a-b). The apparent elastic constants of this model were calculated by relating the average strain to the average stress under simulated uniaxial compression and shear loads with prescribed displacement boundary conditions. The predicted results fell well above the experimental results from uniaxial compressive-strain tests on bovine cancellous bone. There are a number of factors which contributed to this over-prediction:

- The partly random nature of cancellous bone structure (which was not included in the idealised model) contributes to a reduction in actual stiffness.
- The finite element model did not allow for bending of the individual trabeculae since the loads were perfectly aligned
- Displacement based boundary conditions always result in an overestimation of the apparent modulus (Hollister and Kikuchi (1992), Beaupre and Hayes (1985))



3.1a Open-cell bone matrix containing roughly spherical pores



3.1b Beaupre and Hayes' idealised model

Figure 3.1 (Beaupre and Hayes, 1985)

The approach used by Beaupre and Hayes is known as the standard mechanics approach to the homogenisation of material properties of composite materials. It is based on the concept of a Representative Volume Element (RVE) (Hill (1973)) or "base-cell" which represents the periodically repeating microstructure within a composite material. The RVE-based methods decouple the global analysis of a composite or porous material into separate analyses at the local and global levels. At the local level, the microstructural base-cell is analysed to determine its effective elastic properties. In the global structural analysis the composite material is replaced by an equivalent homogeneous material having the previously calculated effective elastic properties. The apparent-level results from the global analysis can then be postprocessed to calculate the microstructural (material-level) response corresponding to this apparent global behaviour. The choice of boundary conditions imposed on the base-cell when calculating the effective elastic properties will strongly influence the results. The boundary conditions must accurately represent the type of boundary conditions which the base-cell is subjected to in the global analysis, and these are not usually known prior to the analysis. The standard mechanics homogenisation methods use either displacement- or traction-based boundary conditions. These methods provide fairly accurate estimates of the apparent elastic properties of the RVE when the

ratio of the RVE size to the global dimensions of the composite (denoted  $\eta$ ) goes to zero. However, in materials such as cancellous bone where the microstructure is only locally periodic ( $\eta$  finite), these imposed boundary effects lead to less accurate results. This has been demonstrated by Hollister and Kikuchi (1992).

An alternative to the displacement- and traction-based boundary conditions is the use of periodic boundary conditions. Here it is assumed that because of the periodic nature of the microstructure, opposite faces of the base-cell will have the same deformations. The homogenisation technique, makes use of this periodic boundary condition for the analysis of composite materials. The postprocessing of apparent level strains to find material-level strains is called localisation (Bensoussan *et al.* (1978)). This localisation step is integral to the derivation of the theory of homogenisation. Much of the initial work on the development of the homogenisation method was done by Babuska (1976), Keller (1977), Larsen (1975), Sanchez-Palencia (1974) and Bensoussan *et al.* (1978). However, published work on the implementation of this method - particularly within the finite element method - is scarce.

Hollister and Kikuchi (1992) investigated the accuracy of the homogenisation method compared to the standard mechanics approaches for global problems where  $\eta$  is not close to zero. They set up a range of two dimensional finite element models of global structures containing five by five ( $\eta=0.2$ ) base-cells with varying solid volume fractions. The effective elastic constants of the base-cells were calculated using the homogenisation method as well as the standard mechanics method with both uniform displacement and uniform traction boundary conditions. These effective properties were then used in the analysis of the global problems where the base-cells were replaced with the equivalent homogeneous elements. The apparent level results were then postprocessed to find the microstructural strains in each base-cell, and these values were compared to those predicted by a standard finite element analysis of the global problem containing the fully discretised microstructures. Hollister and Kikuchi compared their results in terms of strain energy density, and found that the homogenisation results were generally within 30% of the standard finite element results, compared to errors of up to and above 70% in the results of the standard mechanics approaches.

Applied boundary displacements give an upper bound on apparent stiffness while applied tractions give a lower bound \*. Hollister and Kikuchi demonstrated this by showing that the effective material properties predicted by the standard mechanics approaches using multiple RVEs within one base-cell converged to the homogenisation predictions using only one RVE within the base-cell. Meguid and Kalamkarov (1994) used the homogenisation technique to determine the elastic behaviour of reinforced composite materials with unidirectional regular fibres and compared their results to the standard

---

\* By the principle of minimum strain energy, actual, *in situ* boundary conditions will minimise the strain energy, while assumed displacement-based boundary conditions will produce a greater strain energy. Thus to produce the same average strain in a base-cell, the average stiffness predicted with an assumed displacement boundary condition will be greater than the actual average stiffness. By the principle of minimum complementary energy, applied traction boundary conditions will produce a higher complementary energy than the *in situ* traction condition for the same average stress. Thus the average compliance is over-predicted and the average stiffness is under-predicted with assumed traction-based boundary conditions. (Hollister and Kikuchi, 1992)

---

mechanics results. They found that for their composite materials, the effective moduli predicted by the homogenisation method were always bounded by the corresponding standard mechanics values.

Homogenisation has been used in the field of composite materials, for a range of applications. Abeyaratne and Triantafyllidis (1984) used homogenisation to study the overall behaviour of highly porous elastic materials at finite levels of strain. Santosa and Symes (1989) used the method to model the propagation of waves through a composite material made up of linearly elastic inclusions in matrix where the two components are held together by viscous coupling. Sigmund (1994) applied the homogenisation technique to an inverse optimisation problem of finding a base-cell material (made up of truss structures) with given effective properties - including a material with a Poisson's ratio of -1.0.

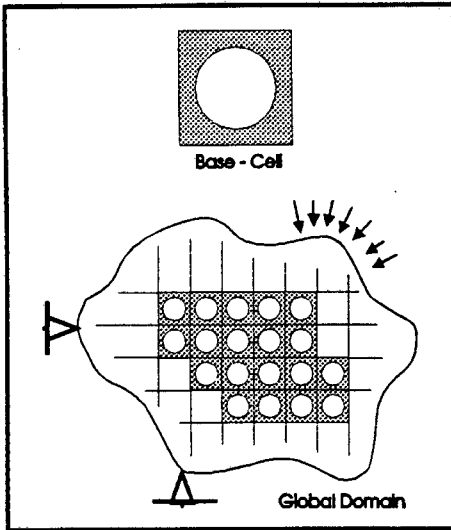
Kohn *et al.* (1993) investigated the viability of using the homogenisation theory to predict the stresses at the implant-bone interface of cementless joint replacements. They developed a simple model of the interface which consisted of a solid bone matrix interspersed with metal beads. Simple two dimensional global models were set up to test the accuracy of the homogenisation technique compared to a direct finite element analysis. Although their model was only periodic in one direction, they found that loading perpendicular or parallel to this direction of periodicity yielded low average errors. However, for shear loading perpendicular to the direction of periodicity, the errors were somewhat higher. They did not investigate the case of shear loading parallel to this periodic direction. In the regions of highest stresses the errors were all below 35%. They found that the homogenisation theory tended to under-predict the stresses in these high-stress regions.

Hollister *et al.* (1991) conducted a simple global numerical test to assess the accuracy of the tissue Von Mises stresses predicted by the homogenisation method using a simple strut-type bone model. This global test consisted of a block of 16 base cell elements loaded in compression. The homogenisation predictions of local strains were compared to the results of a direct finite element analysis of the global model. They found that the predicted Von Mises stresses in the innermost base cell (furthest away from the boundaries) agreed very well with the direct results. However, at the boundaries, the results were less accurate. Actual accuracy levels were not published.

## 3.2 THEORY OF HOMOGENISATION

The salient details of the theory of homogenisation are described in this section. A more formal derivation of the theory is given by Guedes and Kikuchi (1990), and a summary of their derivation is outlined in Appendix B.

The basic assumption of homogenisation theory is that a composite material has a periodically repeating microstructure (the base-cell) which fully characterises the microstructural geometry of the composite material. This is illustrated in Figure 3.2. Two coordinate systems are defined, representing the global and local domains of the composite material. The two Cartesian coordinate systems,  $\mathbf{x}$  and  $\mathbf{y}$  are related by:



$$\mathbf{y} = \frac{\mathbf{x}}{\eta} \quad (3.1)$$

where:  $\mathbf{x} = (x_1, x_2, x_3)^T$  is the  
apparent/macro/global level  
 $\mathbf{y} = (y_1, y_2, y_3)^T$  is the  
fluctuation/micro/local level  
 $\eta$  is the ratio of the microstructure  
or base-cell size to the size of  
the global region in which it exists.

**FIGURE 3.2**  
**Global and local domains of**  
**a composite material**

So, for some function over the global domain  $g(\mathbf{x}, \mathbf{y}) = g(\mathbf{x}, \mathbf{x}/\eta)$ ,

$$\frac{dg}{d\mathbf{x}} = \frac{\partial g}{\partial \mathbf{x}} + \frac{1}{\eta} \frac{\partial g}{\partial \mathbf{y}} \quad (3.2)$$

The material displacements can be described by a periodic displacement vector which can be expanded as follows (Bensoussan *et al.* 1978)

$$\mathbf{u}(\mathbf{x}, \mathbf{y}) = \mathbf{u}_0(\mathbf{x}, \mathbf{y}) + \eta \mathbf{u}_1(\mathbf{x}, \mathbf{y}) + \eta^2 \mathbf{u}_2(\mathbf{x}, \mathbf{y}) + \dots \quad (3.3)$$

where:  $\mathbf{u} = (u_1, u_2, u_3)^T$  is the total microstructural displacement  
vector

$\mathbf{u}_0 = (u_{01}, u_{02}, u_{03})^T$  is the apparent level displacement vector

$\mathbf{u}_m = (u_{m1}, u_{m2}, u_{m3})^T$ ,  $m = 1, 2, \dots, n$ . are the microstructural  
fluctuations about  $\mathbf{u}_0$

Applying (3.2) and (3.3) to the expression for small strains in a continuum, and ignoring all 3rd and higher order displacements (i.e.  $u_2, u_3 \dots$ ), the material strains - using indicial notation - are:

$$\begin{aligned} \varepsilon_{ij \text{ mat}} &= \frac{1}{2} \left( \frac{\partial u_i}{\partial x_j} + \frac{\partial u_j}{\partial x_i} \right) \\ &= \frac{1}{2} \left[ \left( \frac{\partial u_{0i}}{\partial x_j} + \frac{\partial u_{0j}}{\partial x_i} \right) + \frac{1}{\eta} \left( \frac{\partial u_{0i}}{\partial y_j} + \frac{\partial u_{0j}}{\partial y_i} \right) + \right. \\ &\quad \left. \eta \left( \frac{\partial u_{1i}}{\partial x_j} + \frac{\partial u_{1j}}{\partial x_i} \right) + \left( \frac{\partial u_{1i}}{\partial y_j} + \frac{\partial u_{1j}}{\partial y_i} \right) \right] \end{aligned} \quad (3.4)$$

It can be shown that  $u_0$  is a function of the global coordinate system  $x$  only. This result, which implies that the  $1/\eta$  terms in Equation (3.4) are zero, is discussed in Appendix B. Thus, as  $\eta \rightarrow 0$ , (i.e. as the base-cell size becomes very small compared to the overall dimensions of the global domain) the strains are simply:

$$\varepsilon_{ij \text{ mat}} = \frac{1}{2} \left[ \left( \frac{\partial u_{0i}}{\partial x_j} + \frac{\partial u_{0j}}{\partial x_i} \right) + \left( \frac{\partial u_{1i}}{\partial y_j} + \frac{\partial u_{1j}}{\partial y_i} \right) \right]$$

In vector form, where  $\boldsymbol{\varepsilon} = (\varepsilon_{11} \ \varepsilon_{22} \ \varepsilon_{33} \ \varepsilon_{12} \ \varepsilon_{23} \ \varepsilon_{13})^T$ , the material strains can now be written:

$$\boldsymbol{\varepsilon}_{\text{mat}}(\mathbf{u}) = \boldsymbol{\varepsilon}_{\text{app}}(\mathbf{u}_0) + \boldsymbol{\varepsilon}^*(\mathbf{u}_1) \quad (3.5)$$

where  $\boldsymbol{\varepsilon}_{\text{app}}(\mathbf{u}_0)$  is the apparent strain vector

$\boldsymbol{\varepsilon}^*(\mathbf{u}_1)$  is the fluctuation strain vector

Using the principles of virtual work, the equilibrium expression for the global domain of a body containing a composite material can be written:

$$\int_{\Omega} \boldsymbol{\varepsilon}(\mathbf{v})^T \mathbf{D} \boldsymbol{\varepsilon}_{\text{mat}}(\mathbf{u}) d\Omega = \int_{\Gamma} \mathbf{v}^T \mathbf{t} d\Gamma \quad (3.6)$$

where  $\mathbf{v}$  is the virtual displacement vector (any admissible displacement vector)

$\mathbf{t}$  is an applied traction (restricted to the global continuum boundary,  $\Gamma$ , for this derivation - ignoring internal pressures)

$\Omega$  is the volume of the global domain

$\mathbf{D}$  is the constitutive matrix relating stress to strain ( $\boldsymbol{\sigma} = \mathbf{D}\boldsymbol{\varepsilon}$ )

If the microstructure is periodic (i.e. the material consists of a repeating base-cell structure throughout the global domain as illustrated in Figure 3.2), then the following result can be shown to hold in the limit:

$$\lim_{\eta \rightarrow 0} \int_{\Omega} \varphi \, d\Omega = \int_{\Omega} \left[ \frac{1}{V_{\text{cell}}} \int_{V_{\text{cell}}} \varphi \, dV_{\text{cell}} \right] d\Omega \quad (3.7)$$

for some function,  $\varphi$ , which is periodic over  $\Omega$   
 where  $V_{\text{cell}}$  is the volume of the base-cell  
 (Bensousan *et al.* (1978))

Thus, if the virtual displacement  $\boldsymbol{\nu}$  is chosen to be a function of  $\boldsymbol{y}$  only, then using (3.7), Equation (3.6) becomes:

$$\int_{\Omega} \left[ \frac{1}{V_{\text{cell}}} \int_{V_{\text{cell}}} \boldsymbol{\varepsilon}(\boldsymbol{\nu})^T \mathbf{D} (\boldsymbol{\varepsilon}_{\text{app}} + \boldsymbol{\varepsilon}^*) dV_{\text{cell}} \right] d\Omega = 0 \quad (3.8)$$

This is the equilibrium expression on the local, base-cell level. The right hand side can be taken as zero on this local level, since there are no boundary tractions on the microstructural level (see Appendix B).

To satisfy Equation (3.8), the internal integral must be zero. This gives the following result:

$$\int_{V_{\text{cell}}} \boldsymbol{\varepsilon}(\boldsymbol{\nu})^T \mathbf{D} \boldsymbol{\varepsilon}^* dV_{\text{cell}} = - \int_{V_{\text{cell}}} \boldsymbol{\varepsilon}(\boldsymbol{\nu})^T \mathbf{D} \boldsymbol{\varepsilon}_{\text{app}} dV_{\text{cell}} \quad (3.9)$$

which describes the relationship between the apparent strain vector and the microstructural fluctuation strains within the base-cell. If  $\boldsymbol{\varepsilon}_{\text{app}}$  is known for a particular base-cell, the microstructural strains at each point in that base-cell can be calculated from Equations (3.9) and (3.5). The general solution for the tissue strains in terms of the apparent strain vector is found by setting each of the independent terms in  $\boldsymbol{\varepsilon}_{\text{app}}$  to 1 and keeping the other terms zero, and solving (3.9). This results in six independent equations where the right hand side of (3.9) is one of six different “load” vectors corresponding to the six independent, normalised apparent strain vectors. Since the fluctuation strains are linearly dependent on these six independent apparent strain states, linear superposition can be used to calculate the fluctuation strains for any given apparent strain state:

$$\boldsymbol{\varepsilon}^* = \mathbf{E}^* \boldsymbol{\varepsilon}_{\text{app}} \quad (3.10)$$

where the six columns in  $\mathbf{E}^*$  are the six solutions of generic fluctuation strain vectors corresponding to the six normalised independent “load” vectors in Equation (3.9).

Hence, from (3.5), the localisation step to calculate the material strains is:

$$\begin{aligned}\boldsymbol{\varepsilon}_{\text{material}} &= (\mathbf{I} + \mathbf{E}^*) \boldsymbol{\varepsilon}_{\text{app}} \\ &= \mathbf{M} \boldsymbol{\varepsilon}_{\text{app}}\end{aligned}\quad (3.11)$$

where  $\mathbf{I}$  is the identity matrix

Now, returning to Equation (3.6), using (3.7) and choosing  $\boldsymbol{\nu}$  to be a function of  $\mathbf{x}$  only,  $\boldsymbol{\varepsilon}(\boldsymbol{\nu})$  and  $\boldsymbol{\varepsilon}_{\text{app}}$  (which is also a function of  $\mathbf{x}$  only) can be removed from the interior integral to give:

$$\int_{\Omega} \boldsymbol{\varepsilon}(\boldsymbol{\nu})^T \left[ \frac{1}{V_{\text{cell}}} \int_{V_{\text{cell}}} \mathbf{D} \mathbf{M} dV_{\text{cell}} \right] \boldsymbol{\varepsilon}_{\text{app}} d\Omega = \int_{\Gamma} \boldsymbol{\nu}^T \boldsymbol{t} d\Gamma \quad (3.12)$$

which is the variational equilibrium equation at the apparent, global or continuum level. The term in square brackets is analogous to the constitutive matrix in (3.6) so that

$$\mathbf{D}_{\text{app}} = \frac{1}{V_{\text{cell}}} \int_{V_{\text{cell}}} \mathbf{D} \mathbf{M} dV_{\text{cell}} \quad (3.13)$$

This is the apparent constitutive matrix, containing the effective elastic properties of the homogenised base-cell.

### 3.3 IMPLEMENTATION IN THE FINITE ELEMENT METHOD

The implementation of homogenisation in the finite element method involves two steps: homogenisation and localisation. These calculations are carried out at the base-cell level. In the homogenisation step, a discretised mesh of the base-cell is analysed to find the apparent constitutive matrix. These apparent material properties are then used in a global model, where the base-cells are replaced with single continuum elements. The resultant apparent strains from this global analysis are then postprocessed in the localisation step to find the distribution of actual material strains in each base-cell.

The apparent elastic properties of the composite material are calculated using the equilibrium Equation (3.9) over the discretised base-cell.

$$\sum_e^m \int_{\Omega_e} \mathbf{B}^T \mathbf{D} \mathbf{B} d\Omega_e \chi^k = - \sum_e^m \int_{\Omega_e} \mathbf{B}^T d\Omega_e \mathbf{D} \mathbf{i}^k \quad \text{for } k=1,6 \quad (3.14)$$

where  $\Omega_e$  is the volume of an element within the discretised base-cell

$\chi^k$  are the six vectors of nodal displacements corresponding to the six "load" vectors on the right-hand side.

$\mathbf{i}^k$  is column  $k$  of the  $6 \times 6$  identity matrix

$m$  is the number of elements in the base-cell

$\mathbf{B}$  is the strain-displacement matrix in ( $\boldsymbol{\varepsilon} = \mathbf{B}\mathbf{u}$ )  
(Hinton and Owen (1985))

Equation (3.14) has the same form as the standard finite element equilibrium equation:

$$\sum_e \mathbf{K}_e \chi_e^k = \sum_e \mathbf{f}_e^k$$

where  $\mathbf{K}_e$  is the element stiffness matrix

$\mathbf{f}_e$  is the element nodal load vector

The  $k$ th vector in  $\chi_{k=1,6}^k$  represents the solution for displacements at each node within the base-cell that would be required to maintain equilibrium if the  $k$ th term in  $\boldsymbol{\varepsilon}_{app}$  were set to 1. These six solution vectors are calculated (for the whole base-cell) using periodic boundary conditions. This is consistent with the original assumption that the displacement field is periodic across the global domain. Periodicity implies that opposite faces of the base-cell are constrained to have equal displacements in all directions. This will only be exactly true in the limit as  $\eta \rightarrow 0$  (i.e. as the size of the base-cell becomes very small compared to the dimensions of the global structure).

The apparent constitutive matrix is then determined according to Equation (3.13):

$$\mathbf{D}_{\text{app}} = \frac{1}{V_{\text{cell}}} \sum_e^m \mathbf{D}(\mathbf{I} + \mathbf{B} \mathbf{X}) \Omega_e \quad (3.15)$$

$$\text{where } \mathbf{X}_{6 \times 6} = [\chi^1, \chi^2, \dots, \chi^6]$$

$\mathbf{D}_{\text{app}}$  is the weighted average of the individual contributions of each micro-element (weighted according to micro-element volume) in the base-cell. The calculation of  $\mathbf{D}_{\text{app}}$  is called the homogenisation step.

The matrix  $\mathbf{X}$  is stored for the calculation of tissue strains for the localisation step:

$$\boldsymbol{\varepsilon}_{\text{mat}} = (\mathbf{I} + \mathbf{B} \mathbf{X}) \boldsymbol{\varepsilon}_{\text{app}} \quad (3.16)$$

where  $\mathbf{B} \mathbf{X}$  is equal to  $\mathbf{E}_{6 \times 6}^*$  in Equation (3.11)

The homogenisation algorithm, which includes both the homogenisation and localisation steps, is coded in FORTRAN within a three-dimensional finite element program using 8-noded bilinear isoparametric elements. (A previously written two dimensional code was first adapted to a general purpose three dimensional FE code and then the homogenisation algorithm was incorporated into this code.)

Additional programs have been written to integrate the homogenisation program with the ABAQUS preprocessor, ABAPRE (Hibbitt *et al.* (1994)), for generating discretised base-cells, and to sort and compare postprocessed results. The user information for these codes, including the homogenisation program, is detailed in Appendix E. Homogenisation analyses can be run using either full or reduced integration. Appendix E includes information on an hour-glass control algorithm which was incorporated in the homogenisation code to prevent spurious zero energy modes when reduced integration is used. The homogenisation and localisation FORTRAN subroutines are listed in this appendix. The full homogenisation code, as well as the input deck formatting code and results postprocessing code are stored on a floppy disk in the back of this thesis.

### 3.4 NUMERICAL TRIALS

A number of trial problems have been set up to test the performance of the homogenisation technique for modelling cancellous bone. It was important to assess the accuracy of the technique under conditions which are characteristic of cancellous bone geometry and environment. Simple base-cell models containing thin-walled structures with high void fractions have been analysed under compression and shear loading conditions and different global boundary conditions.

The following questions regarding the accuracy of the homogenisation method have been addressed:

- How accurate are the results in base-cells which are close to external boundaries?
- How small should  $\eta$  be to ensure acceptable levels of accuracy?
- Should the assumption of periodicity be adhered to in all directions, or only in the directions of dominant global loads (i.e. should  $\eta$  be small in all three directions)?
- Does the choice of integration scheme affect the accuracy of the results?
- What are the effects of various loading conditions on the accuracy of the results?
- Does the homogenisation method accommodate bending modes of deformation within the base-cell?

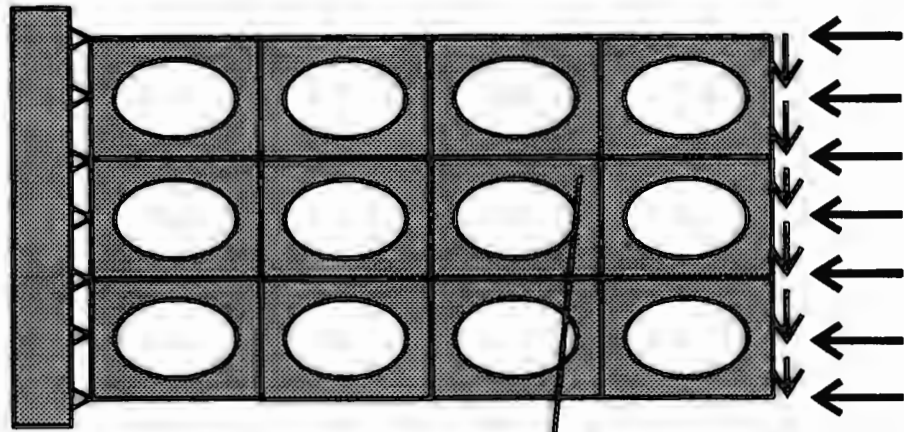
The testing procedure (illustrated in Figure 3.3) is as follows:

Two global models are created. The first model is a standard finite element mesh of the global problem containing the fully discretised base-cells. The second model has the same global dimensions and loading and boundary conditions as the standard model, but each base-cell is replaced with a single “homogenised” element. These global continuum elements are given the calculated apparent material properties of the base-cell. The test problems are run on ABAQUS version 5.4 (Hibbitt *et al.* (1994)).

The apparent strain results in the homogeneous model are postprocessed in the localisation step to calculate the local tissue strains. These local strains are then compared to the strains which were calculated directly in the first standard model. Instead of comparing each of the six independent strain terms, the results are compared in terms of the percentage errors in strain energy density in each element within each base-cell. Table 3.1 - at the end of this section - gives a summary of the results for each global test. A more comprehensive set of results is given in Tables C1-C9 in Appendix C.

A simple base-cell model representing a microstructure with longitudinal plates containing fenestrations has been used for the first set of test problems. This base-cell has an apparent density of 0.22, and is illustrated in Figure 3.4. The external faces of the base-cell are defined as the six faces of a rectangular prism which would be just big enough to accommodate the base-cell. All nodes in the base-cell which are common to these external faces are subject to the periodic boundary constraints. These boundary conditions force all nodes on opposite external faces of the base-cell to have the same displacements. This is illustrated in Figure 3.3a where a discretised two-dimensional base-cell fits into a rectangle, and the nodes which occur at the external faces have the same displacements as those on the opposite (like-coloured) face. Consequently, the four corner nodes have the same displacements. The application of the boundary conditions when creating the base-cell in the preprocessor is described in Appendix E.

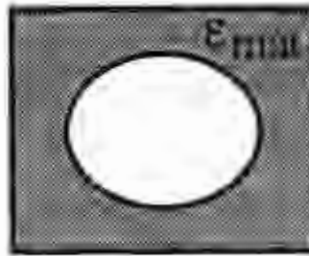
Standard finite element analysis of global problem



$\epsilon_{mat}$

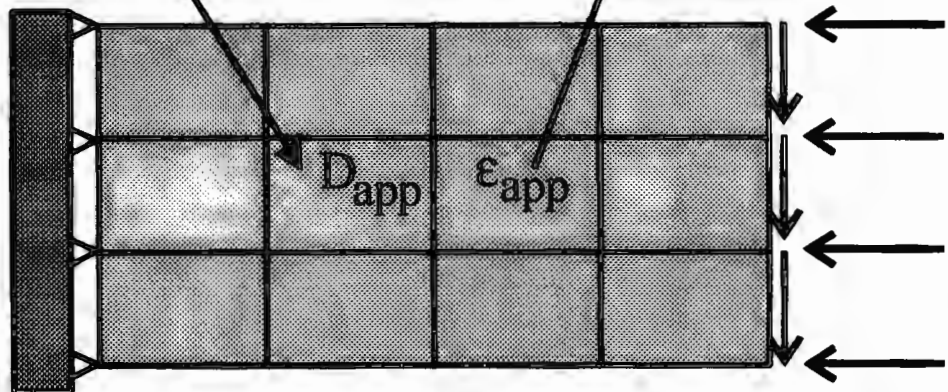
compare results

Homogenisation



Localisation

Base-cell



Homogenisation analysis of global problem

FIGURE 3.3 Schematic of procedure for numerical homogenisation trials

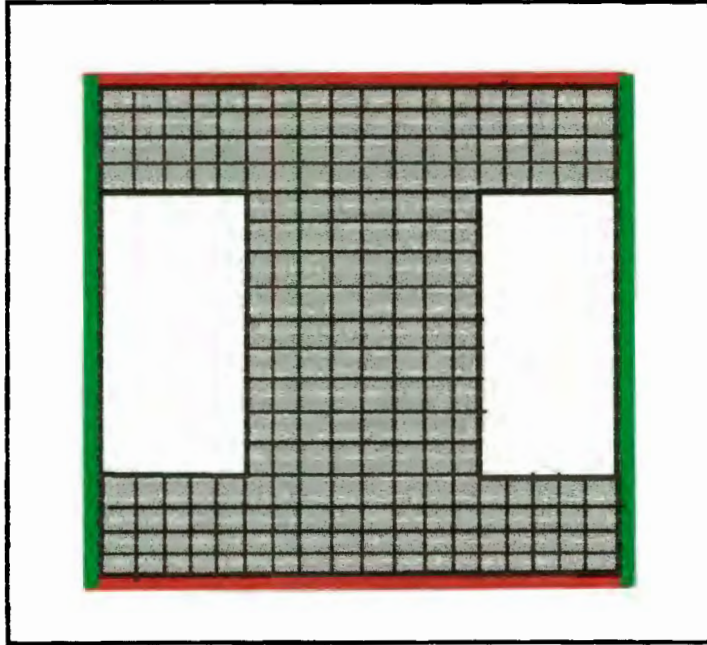


**FIGURE 3.3a** Periodic boundary conditions applied to base-cell  
(nodes on opposite (like-coloured) external faces  
have the same displacements)

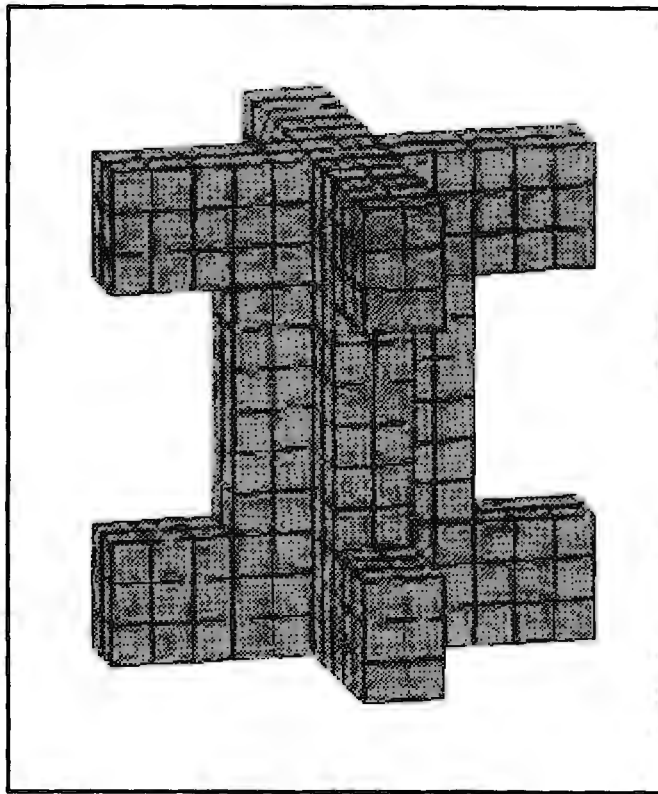


**FIGURE 3.4 First base-cell model**

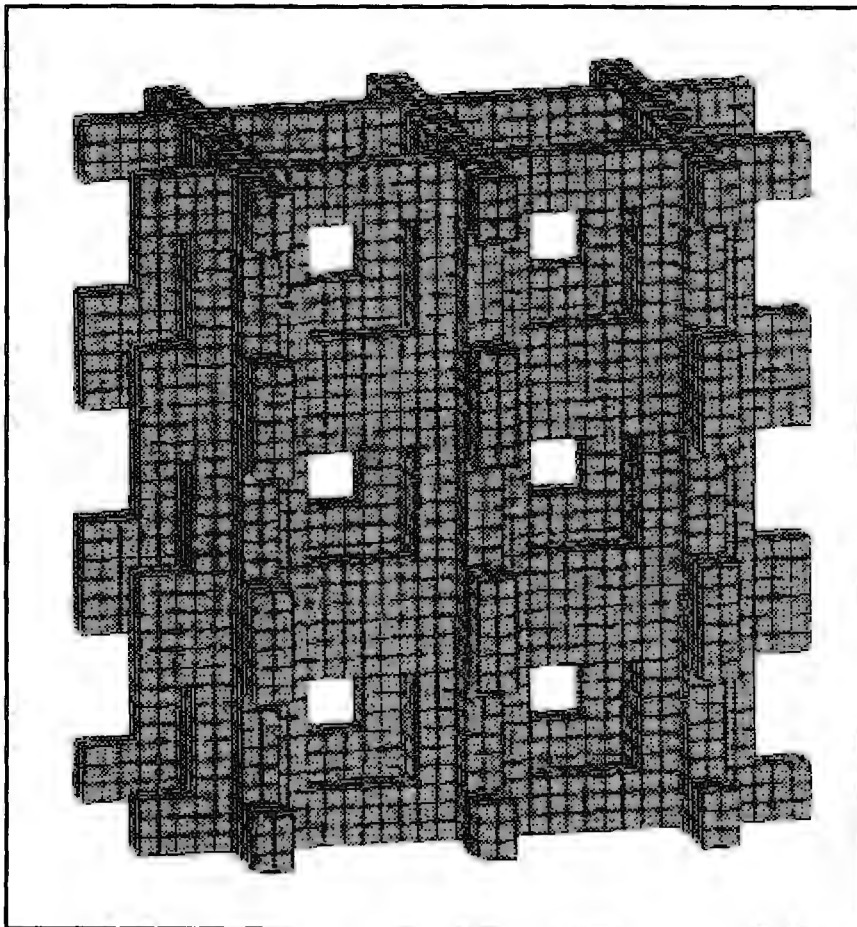
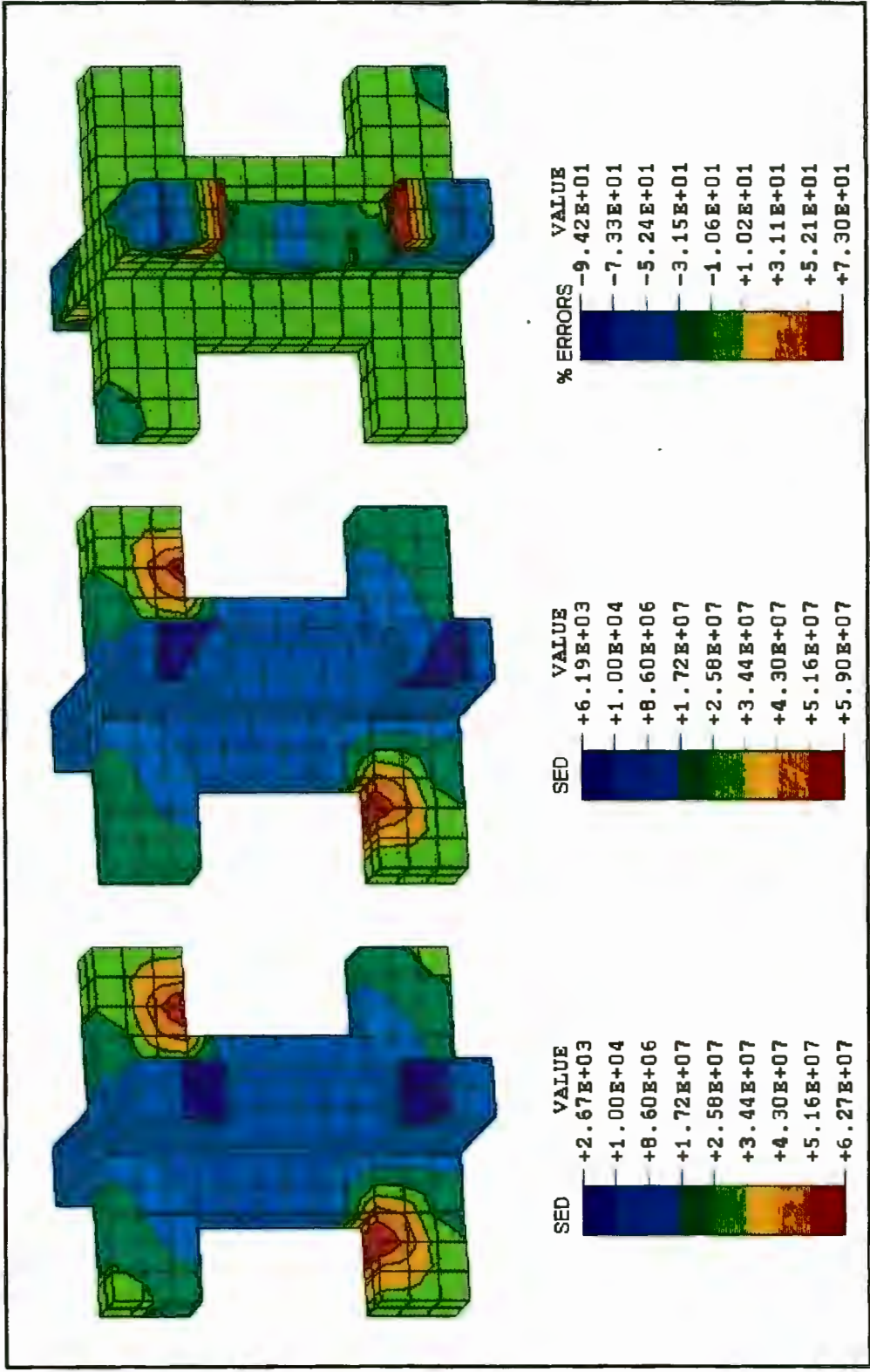


**FIGURE 3.5 Symmetrical half of first global test model  
(Section 3.4.1)**

### 3.4.1 BOUNDARY AND LOADING CONDITIONS

First, the overall accuracy of the homogenisation method was investigated under uniform normal and shear loading conditions in regions close, but not immediately adjacent to external boundaries. The first global model is illustrated in Figure 3.5 (showing only the symmetric half). The model consists of a block of 3x3x4 base-cell structures. Uniform normal and shear displacements were applied to the one face of the block (in the same way illustrated in Figure 3.3), and boundary conditions were applied to the opposite face which constrained rigid body modes but allowed for sliding parallel to the wall, except in the direction of the shear load. The values of tissue strain energy density from the homogenisation and direct analyses were compared for only the innermost base-cell which would be least affected by the external boundary effects.

Contour plots of the predicted strain energy densities for the homogenisation and direct analyses are compared in Figures 3.6a and 3.6b, respectively. (The same contour legend scale is used for both models, although the minimum and maximum strain energy densities are different for the two legends). The distribution of percentage errors within this base-cell is illustrated in Figure 3.6c and listed in Table C1 in Appendix C. The errors in the homogenisation tissue strains (relative to the directly calculated values) are below 20% for 82% of the solid base-cell volume. Errors of above 50% occur in 9% of the solid volume. However, these high errors occur in regions where the strains are very low compared to the maximum strains, and thus the actual magnitudes of the errors are low, and are of little consequence. This can be seen in the contour plots. In all regions of high strain in the base-cell, where actual strain energy densities are within 20% of the maximum value, the percentage errors in the predicted values are all below 6%.



**3.6a** HOMOGENISATION PREDICTION      **3.6b** STANDARD FEM PREDICTION      **3.6c** PERCENTAGE ERRORS IN SED

**FIGURE 3.6 Homogenisation and standard finite element predictions of strain energy densities in innermost base-cell for first numerical trial (Section 3.4.1)**

### 3.4.2 PERIODICITY

The second global model tested the accuracy of the homogenisation method for structures which are periodic in only two directions. This test is similar to that conducted by Kohn *et al.*(1993), except accuracies for shear loading parallel (not perpendicular) to the directions of periodicity have been investigated here. This global model, illustrated in Figure 3.7, has only one layer of base-cell elements in the direction of non-loading. The loading and boundary conditions are the same as in the first model.

The contour plots of the results for the innermost base-cell are shown in Figures 3.8 a, b and c. These results are very similar to those of the previous test. Again, the errors in the innermost base-cell are low (Table C2). The errors are below 20% for 88% of the base-cell volume. The predicted strain energies in the regions of high strain (top 20%) are all within 5% of the directly calculated values, and only 4% of the structure has errors greater than 50%.

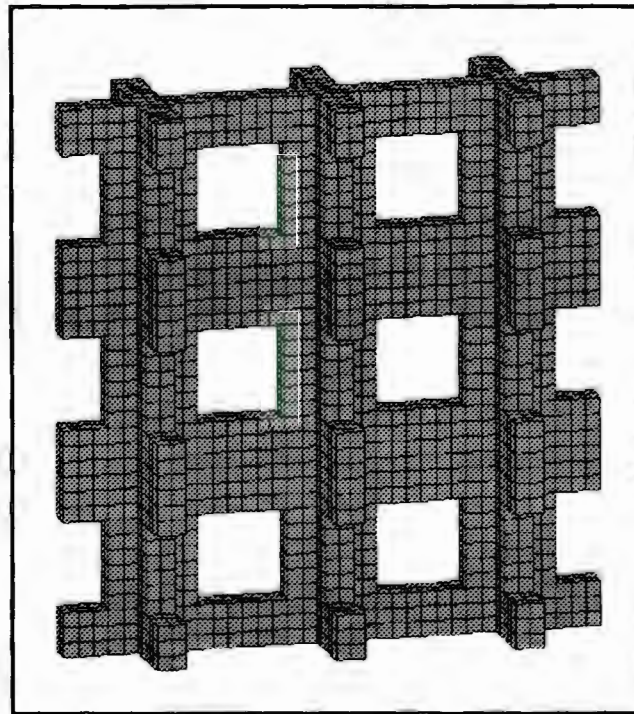
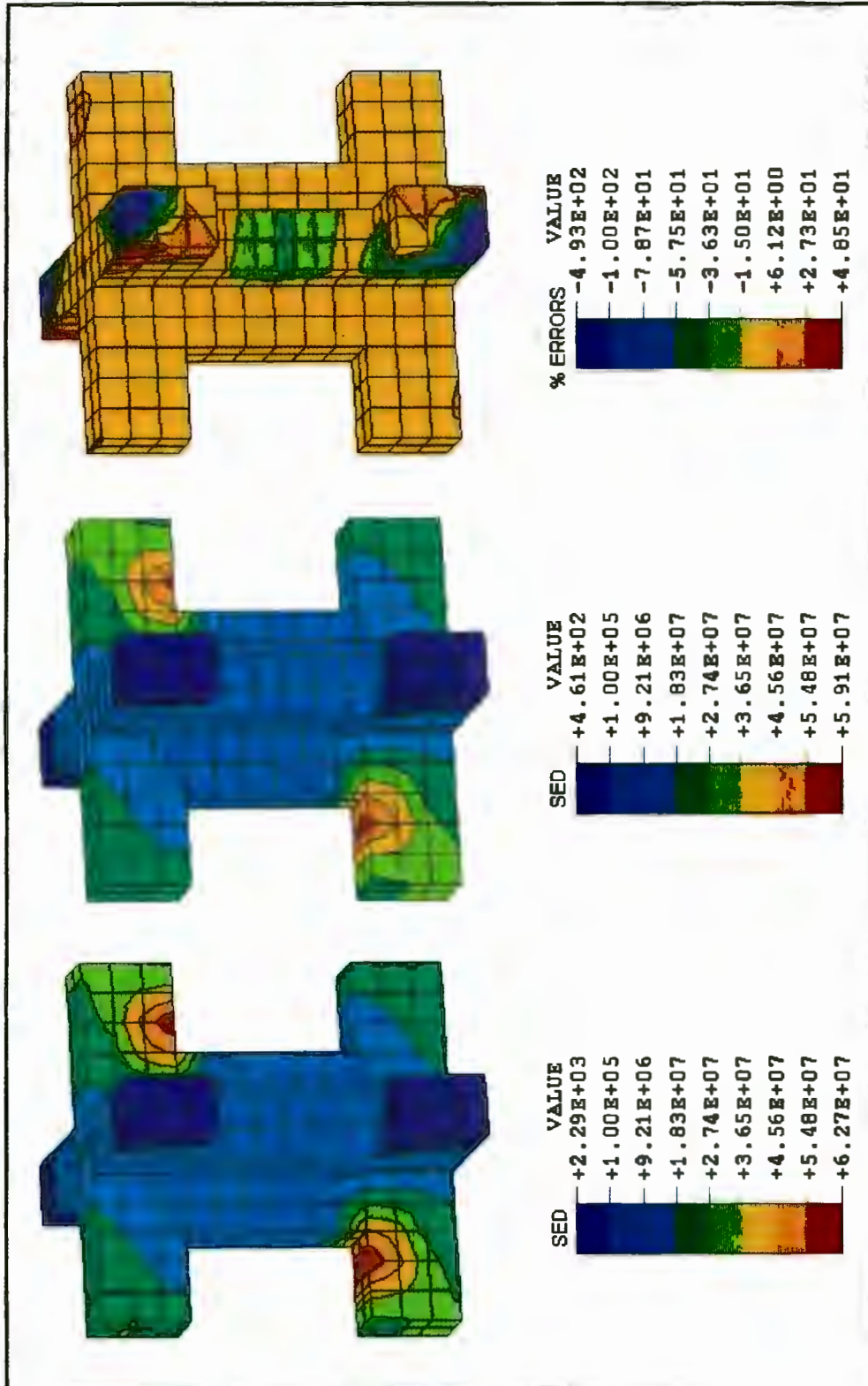


FIGURE 3.7 Second global test model (Section 3.4.2)



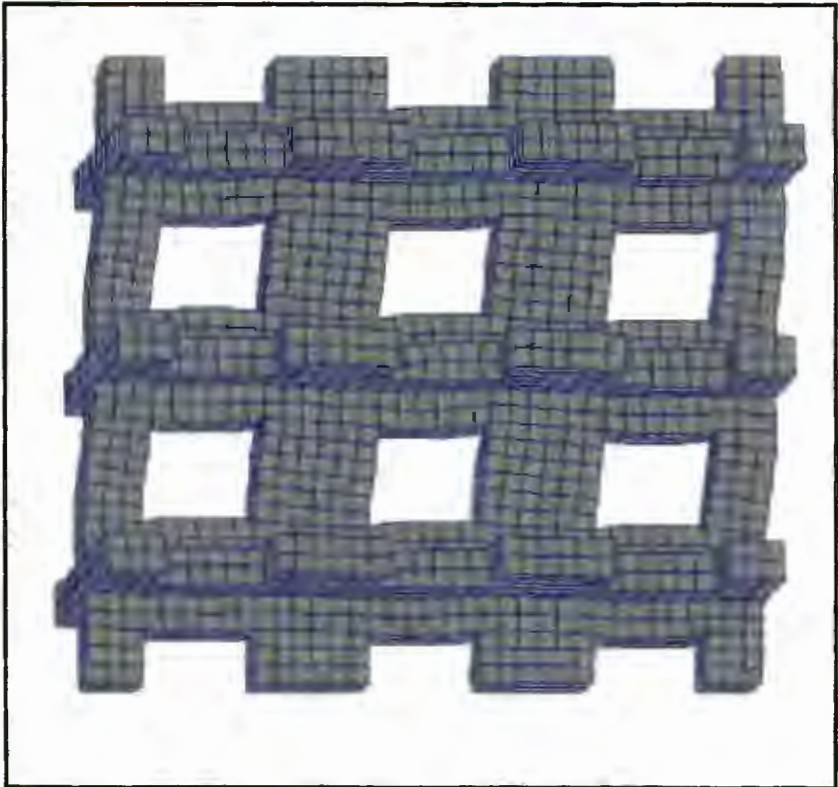
**FIGURE 3.8 Homogenisation and standard finite element predictions of strain energy densities in innermost base-cell for second numerical trial (Section 3.4.2)**

### **3.4.3 INTEGRATION SCHEME AND BOUNDARY EFFECTS**

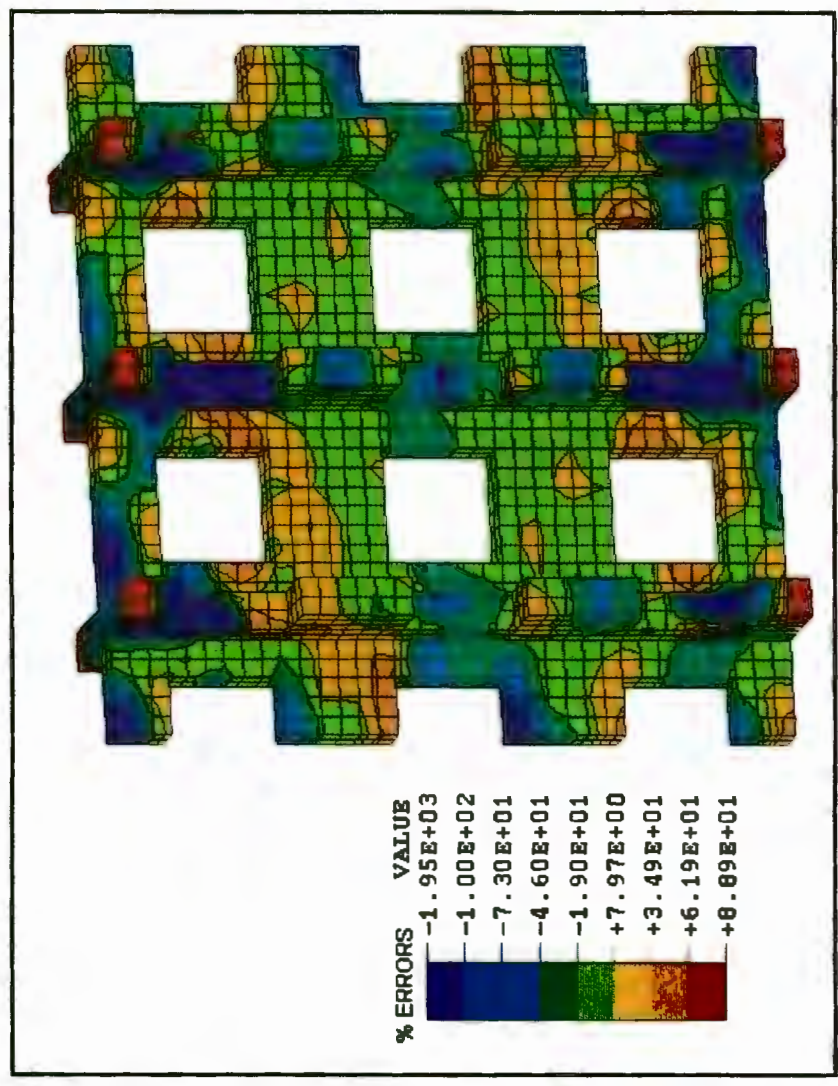
For the previous two test problems, full integration (2 x 2 x 2 gauss point rule) has been used for all the finite element calculations. The objective of this third test was to determine whether the generally high levels of accuracy that are achieved with full quadrature are maintained when reduced integration is used. As 8-noded linear elements are over-stiff when full integration is used, it is desirable to use reduced integration for the analysis of idealised bone structures so that the bending deformations can be more accurately predicted.

The third global model is the same as the second (Figure 3.7), except reduced integration is used for the homogenisation, localisation and the direct finite element calculations. Although the internal structures in the base-cell do not have inherent bending modes of deformation, applied shear loading does induce some bending within this microstructure. The results of this test (Table C3) for the innermost base-cell compare reasonably well to the full integration results, although in the regions of high strain, errors of up to 14% occur, which is somewhat higher than the maximum of 5% for the full integration result.

Over the entire global domain (all nine base-cell elements) the reduced and full integration results are similar (Tables C4 and C5). The results for the reduced integration analysis are illustrated in Figures 3.9a-d. Figure 3.9a shows the displaced shape of the global model under the applied loading. Figure 3.9c shows the predicted homogenisation strain energy densities throughout the porous region, compared to the direct finite element results in Figure 3.9d. The percentage errors in strain energy density are plotted in Figure 3.9b. These contour plots indicate that the homogenisation technique predicts the overall strain trends very well throughout the global model, and in the internal regions where strains are high, the actual magnitudes are in close agreement. However, where the strains are low, the percentage errors can be very large (more than 1000 %). These high errors are insignificant because they correspond to actual error magnitudes which are very low. However, certain high strains at the boundaries are underpredicted by the homogenisation method by up to 51%. This occurs for both the reduced and full integration schemes. The reason for this is that the external boundary influences result in localised strain energy density concentrations which do not recur periodically across the global domain and which are thus inconsistent with the periodicity assumption.

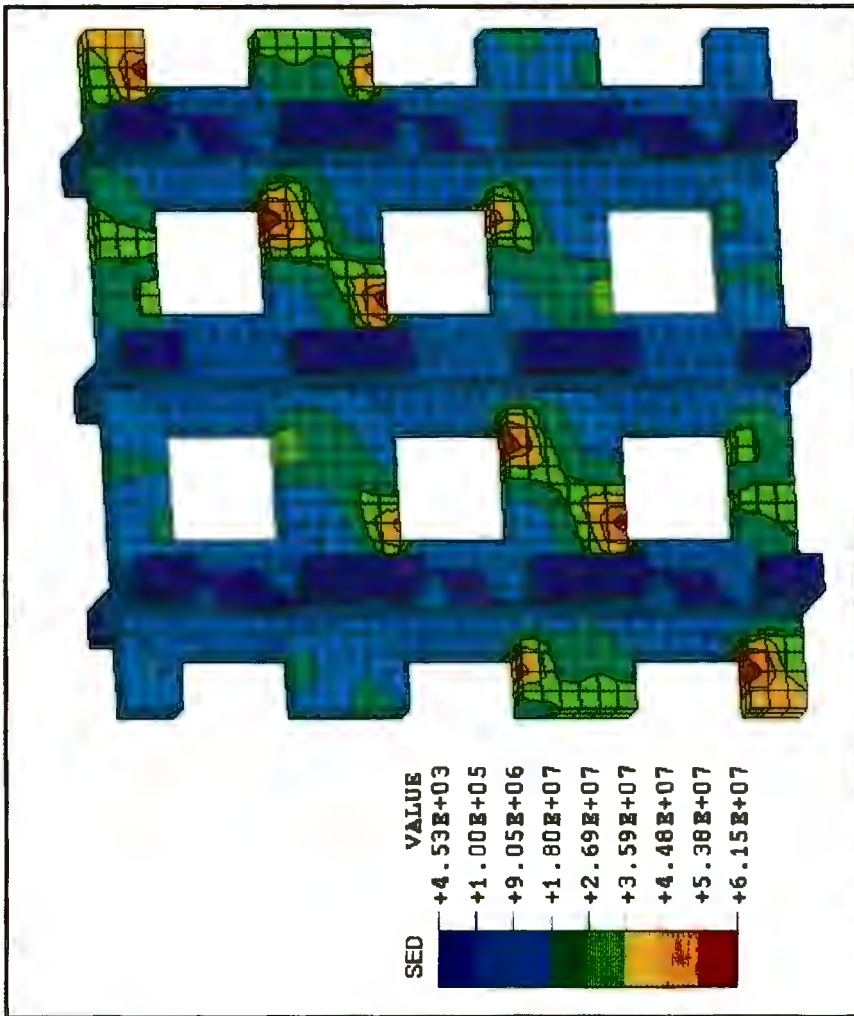


**3.9a**  
**DISPLACED SHAPE**

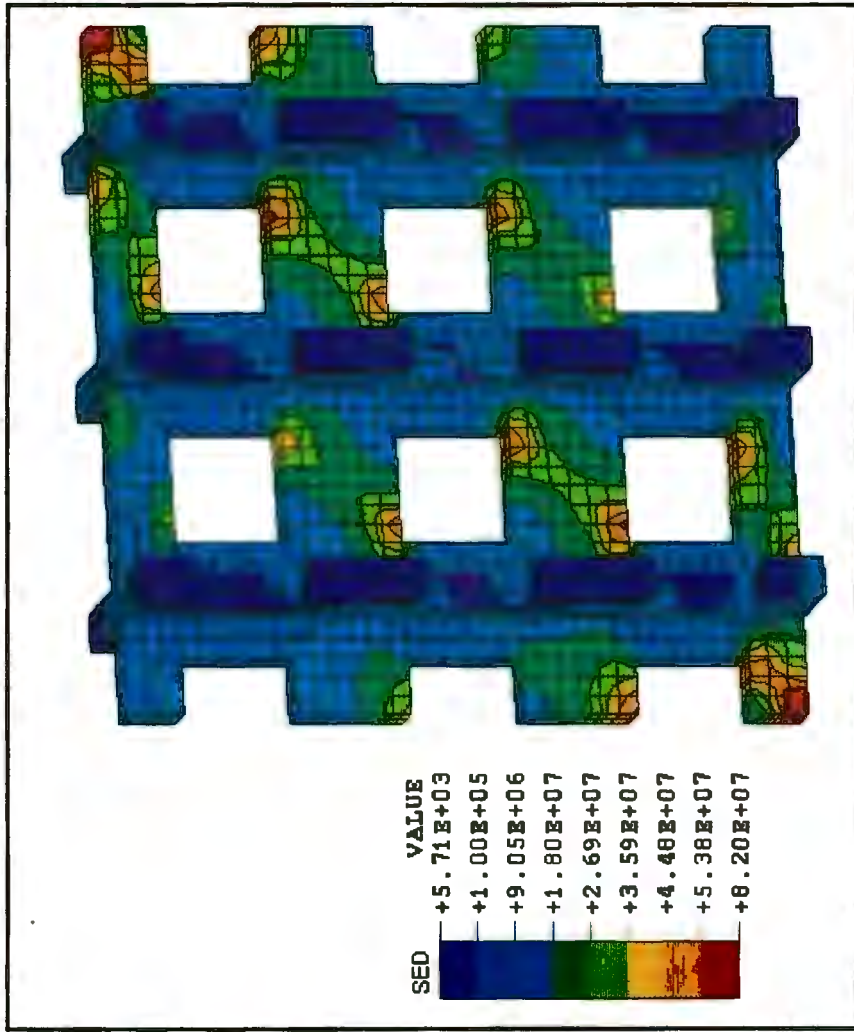


**3.9b**  
**PERCENTAGE ERRORS IN**  
**STRAIN ENERGY DENSITY**

**FIGURE 3.9** Displaced shape and percentage errors in SED for second global model using reduced integration (Section 3.4.3 - uniform shear and compressive loading)



**3.9c**  
**HOMOGENISATION**  
**PREDICTION**



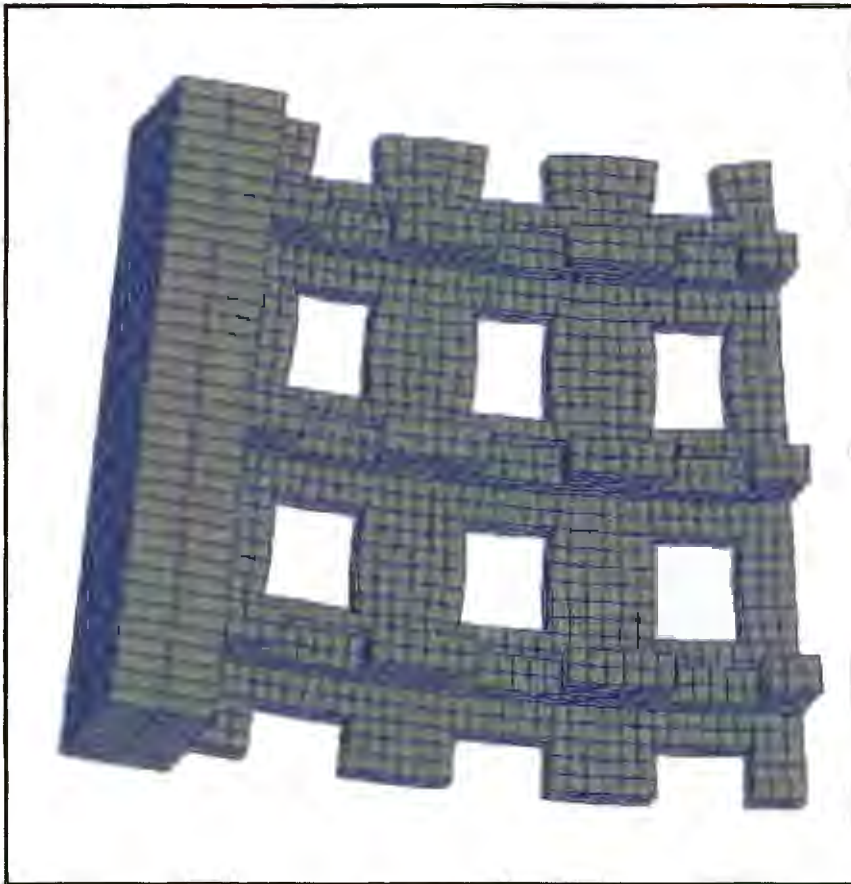
**3.9d**  
**STANDARD FEM**  
**PREDICTION**

**FIGURE 3.9 (cont.) Homogenisation and standard FEM predictions of strain energy density in full global model (Section 3.4.3 - uniform shear and compressive loading)**

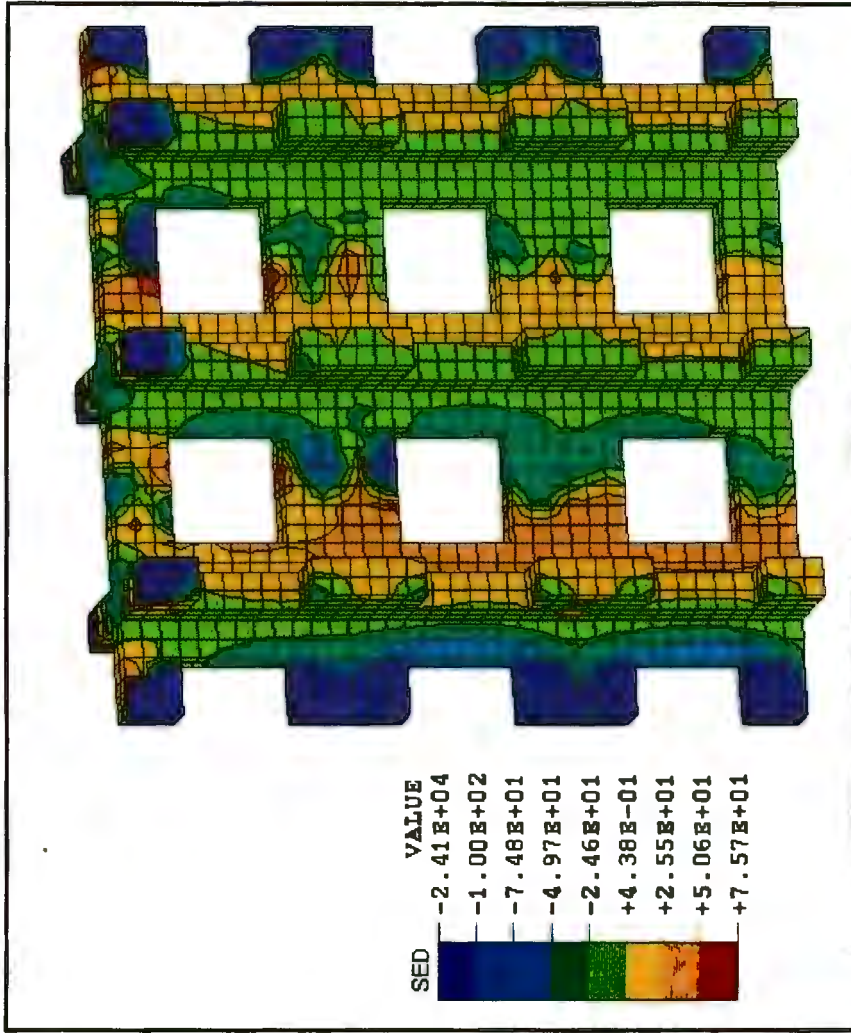
### 3.4.4 NON-UNIFORM LOADING

The effect of non-uniform loading on the accuracy of the results has been investigated using the same set of  $3 \times 3 \times 1$  base-cells as in the previous model with an additional thick, stiff metal plate resting on the top surface of the composite structure. The plate was loaded with a non-uniform eccentric pressure across the top surface. The resultant deformation of the model is shown in Figure 3.10a. The high stiffness of the metal plate ( $E=200\text{GPa}$ ) relative to that of the solid-phase material in the porous region ( $E=5\text{GPa}$ ) was assumed to render the softening effect of the higher degree of discretisation of the plate in the standard model - compared to the 6-element plate in the homogenisation model - negligible. (For the porous region, the reduced stiffness of the fully discretised base-cells in the direct analysis, compared to the single-element homogeneous base-cells, is accounted for in the homogenisation calculation of the apparent material properties).

The results of this test (using reduced integration) are illustrated graphically in Figures 3.10b,c and d. As in the previous test, the overall stress distributions and magnitudes using the homogenisation method are in close agreement with the direct finite element solution over the entire global domain. Again, in regions of high strain, the errors are low, and high percentage errors occur where the strain energy densities are very low. Table C6 shows that the percentage errors throughout the global model for this test are considerably lower than those of the previous test where uniform forced shear and compressive displacements were imposed on the model. 73% of the entire porous region has errors below 20%, only 9% of this region has errors above 50%, and all regions of high strain (within 20% of the maximum strain energy density) have errors below 16%.

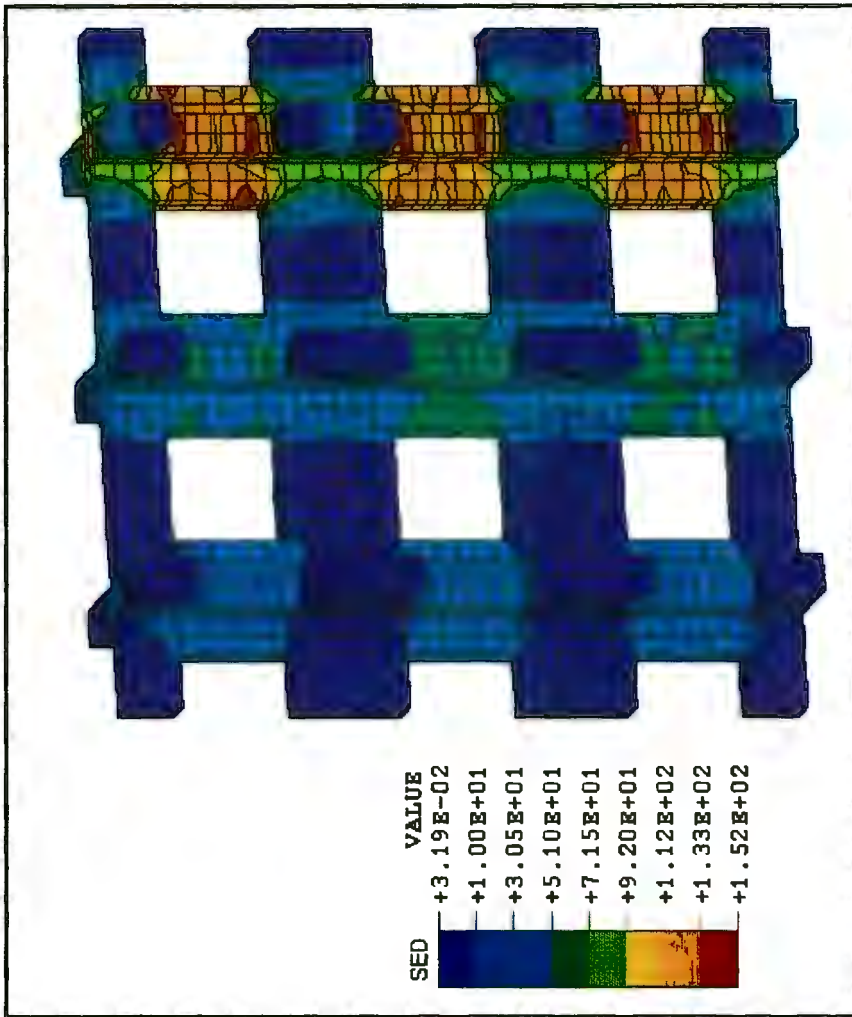


**3.10a**  
**DISPLACED SHAPE**

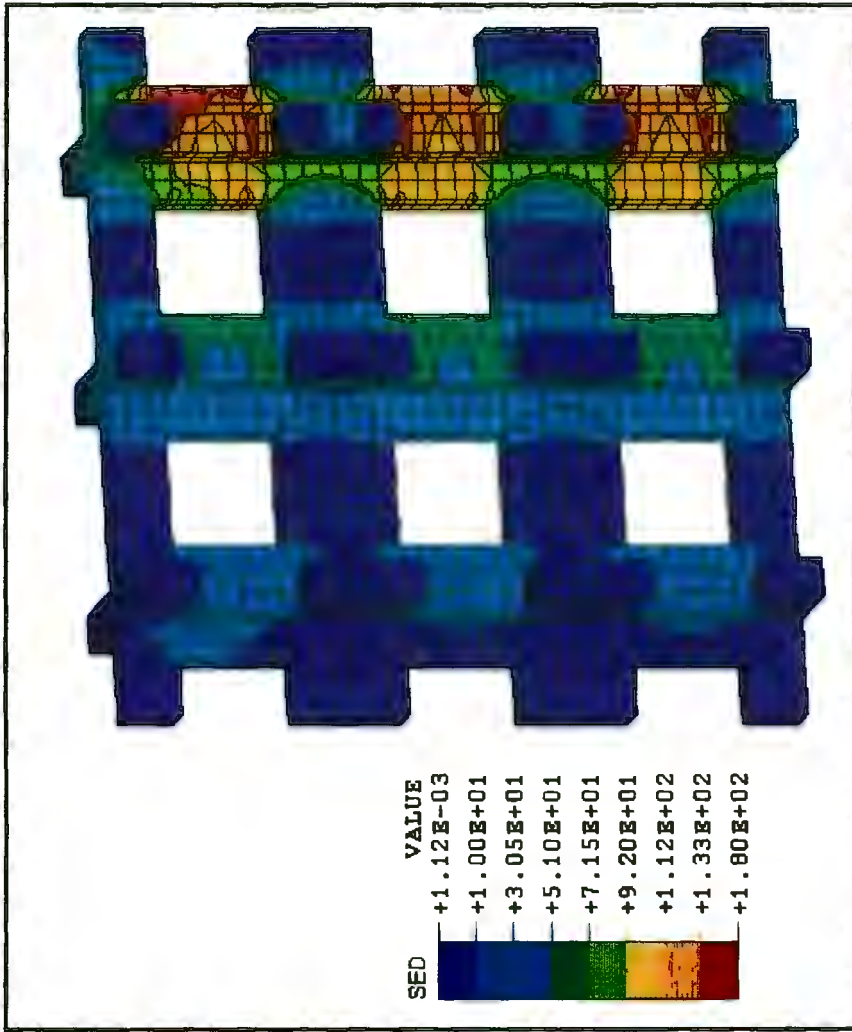


**3.10b**  
**PERCENTAGE ERRORS IN**  
**STRAIN ENERGY DENSITY**

**FIGURE 3.10** Displaced shape and percentage errors in SED for third global model using reduced integration (Section 3.4.4 - eccentric compressive loading)



**3.10c**  
**HOMOGENISATION**  
**PREDICTION**



**3.10d**  
**STANDARD FEM**  
**PREDICTION**

**FIGURE 3.10 (cont.) Homogenisation and standard FEM predictions of strain energy density in full global model (Section 3.4.4 - eccentric compressive loading)**

### 3.4.5 BENDING MODES

The base-cell that has been used for the global tests thus far consists of axially aligned plate-like structures made up of uniform brick elements. These plates do not exhibit internal bending under compressive loads. The tests described in this section involve simple base-cell models with curved members which are designed to bend under perfectly aligned compressive loads. Three base-cell models were generated with the same basic structure but varying wall thicknesses (Figure 3.11). The apparent constitutive matrices of these three base-cells were calculated using the homogenisation code, and the apparent axial Young's moduli were extracted from these results. The purpose of this test was to determine whether the predicted Young's moduli would vary with apparent density (determined from wall thickness) according to a power law relation - as is reported for cancellous bone (discussed in Chapter 2).

Reduced integration was used for these tests to accommodate the bending modes of the vertical structures. To prevent spurious zero-energy modes, hour-glass control was used. For the three base-cell models in this test, a range of values for  $F_{HG}$  (the hour-glass stiffness scaling factor - described in Appendix E) between 0.1 and 0.0001 was investigated. At a threshold value of around 0.001 round-off errors start to occur. A scale factor of  $F_{HG} = 0.01$  was thus used to calculate the effective compressive stiffness values for all three base-cells.

The resultant apparent Young's moduli for the three base-cell models are plotted against apparent density in Figure 3.12. A linear regression curve was fitted to the logarithmic values of these data points (including the origin), and it was found that for this base-cell structure, apparent stiffness is dependent on the square of apparent density ( $r^2 = 0.99$ ). The apparent density values were adjusted to include only the relative volume of the vertical bending members and not the upper and lower plates so that the regression curve could reasonably be assumed to go through the origin. In Figure 3.12, the same curve is plotted for the full integration results. The regression exponent for these results is 1.8 ( $r^2 = 0.99$ ), and the actual values of apparent stiffness are significantly higher than the reduced integration values - especially at low apparent densities.

One final test was conducted to test the prediction of bending strains by the homogenisation method compared to the direct finite element method. This simple test involved the vertical compression of one base-cell structure ( $\rho = 0.22$ ). The external boundaries were constrained in the transverse directions. The results of this test, using first reduced integration (with hour glass control) and then full integration, are listed in Tables C7 and C8, respectively. The full integration prediction of vertical stiffness is 23% greater than the reduced integration result. However, there are greater discrepancies between the homogenisation and direct results when reduced integration is used compared to the full integration results - especially in regions of high strain, where errors of up to 18% occur compared to only 2% when using full integration. This result is consistent with the result of the previous comparison between full and reduced integration schemes. Contour plots of the homogenisation and direct predictions of strain energy density in the base-cell using reduced integration are shown in Figures 3.13a and 3.13b. The percentage differences between these results are illustrated in Figure 3.13c. These plots show that the strain distributions are very well predicted by the homogenisation method - even with the less accurate reduced integration scheme.

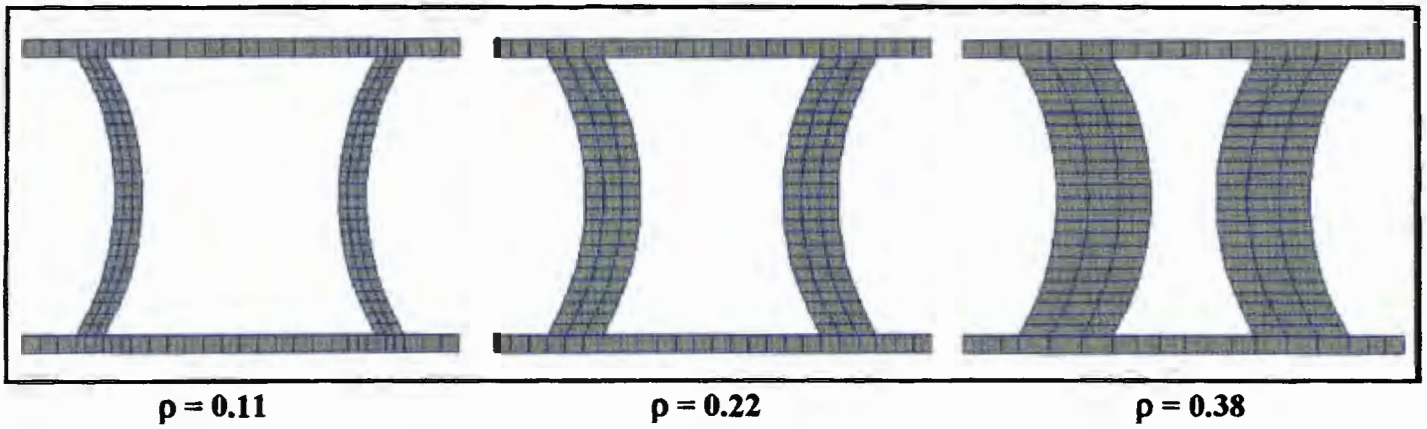


**FIGURE 3.11 Bending test base-cells (Section 3.4.5)**

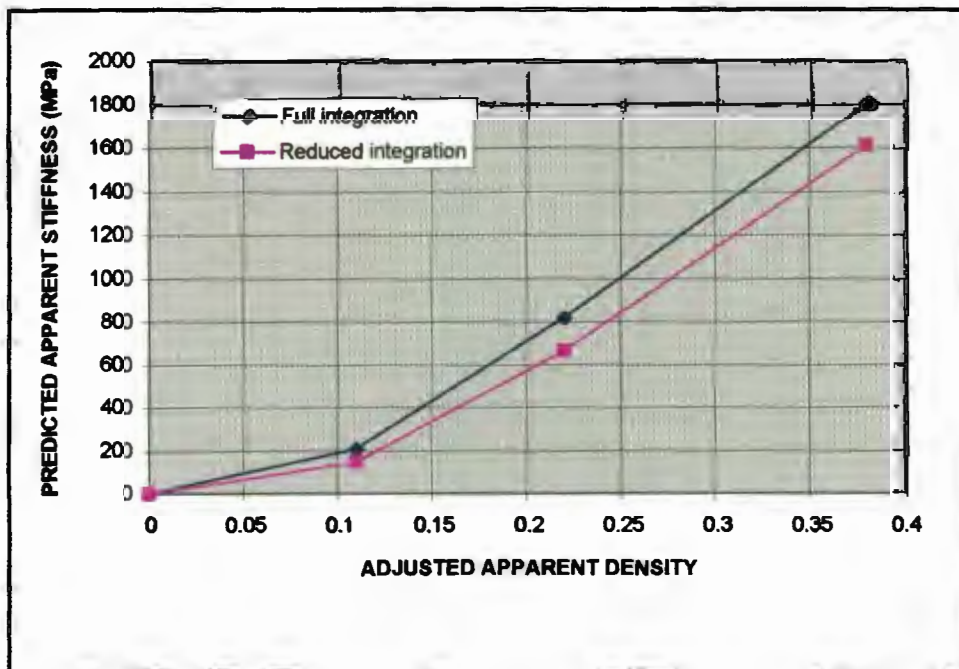


**FIGURE 3.12 Apparent vertical stiffness vs apparent density for base-cell structures with internal bending members**

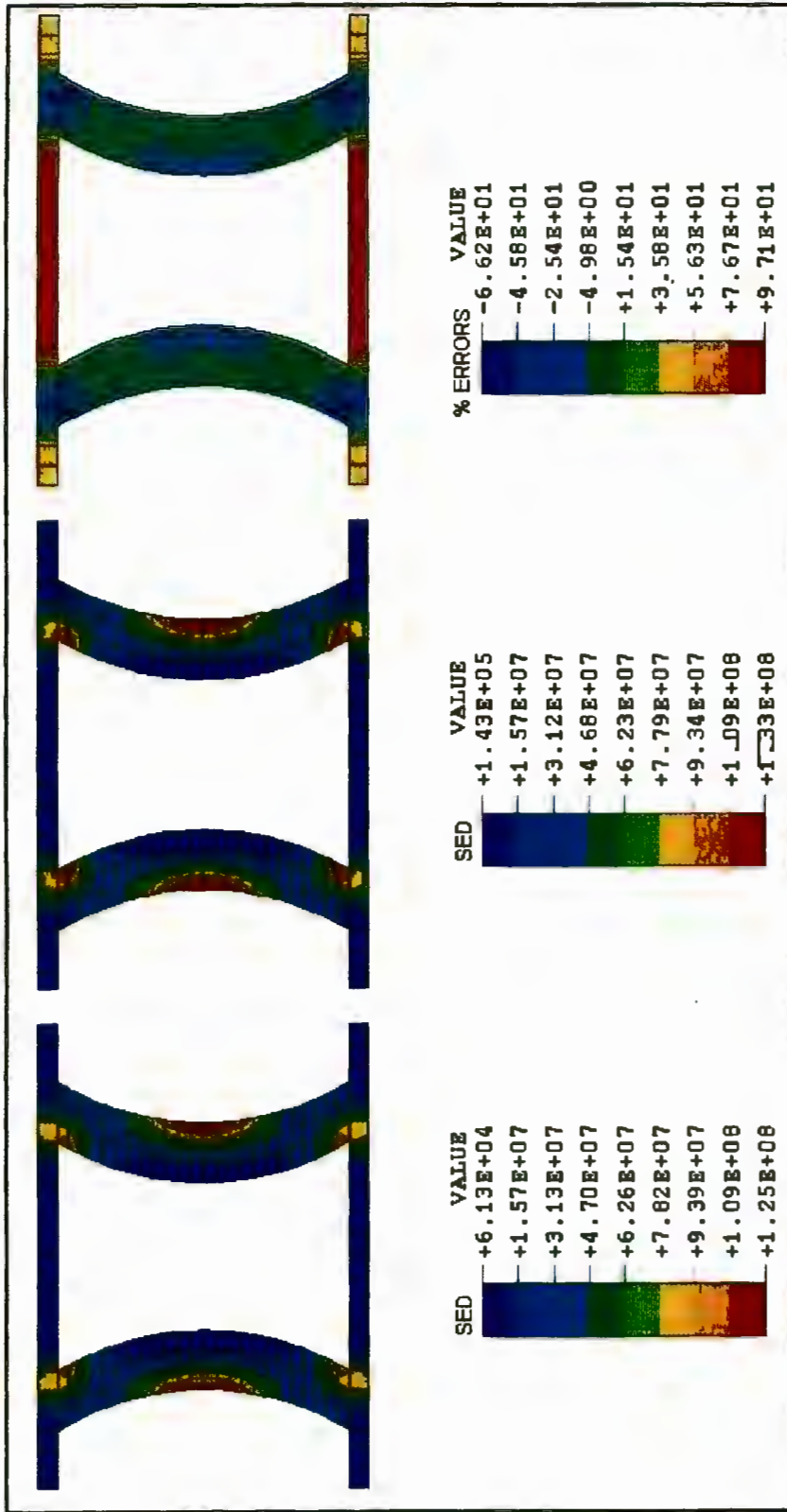


**FIGURE 3.13 Homogenisation and standard finite element predictions of strain energy densities in base-cell structure containing bending deformations (section 3.4.5)**

On the assumption that reduced integration is indeed a better integration scheme for the analysis of these base-cells, the results of the final tests between the standard analysis using reduced integration and the homogenisation analysis using full integration are compared. The differences between these two sets of results are listed in Table C9. The errors here are considerable. Differences of up to 33% occur in regions where the strain energy density is within the top 20%. Only 34% of the solid volume is within 20% of the standard finite element (reduced integration) results, and 40% of the solid volume has errors greater than 50%.

**TABLE 3.1 Summary of results of numerical homogenisation trials**

| TEST<br>Global<br>Model (Table) | Base-<br>cell/s | % solid volume<br>with errors<br>below 20% | % solid volume<br>with errors<br>above 50% | Maximum error in<br>regions of high<br>SED (top 20%) | Integration<br>rule                    |
|---------------------------------|-----------------|--------------------------------------------|--------------------------------------------|------------------------------------------------------|----------------------------------------|
| 1 (C1)                          | innermost       | 82%                                        | 9%                                         | 5%                                                   | full                                   |
| 2 (C2)                          | innermost       | 88%                                        | 4%                                         | 5%                                                   | full                                   |
| 2 (C3)                          | innermost       | 70%                                        | 6%                                         | 4%                                                   | reduced                                |
| 2 (C5)                          | all             | 50%                                        | 22%                                        | 54%                                                  | full                                   |
| 2 (C4)                          | all             | 49%                                        | 20%                                        | 51%                                                  | reduced                                |
| 3 (C6)                          | all             | 73%                                        | 9%                                         | 16%                                                  | reduced                                |
| 4 (C8)                          | 1               | 64%                                        | 19%                                        | 2%                                                   | full                                   |
| 4 (C7)                          | 1               | 51%                                        | 23%                                        | 18%                                                  | reduced                                |
| 4 (C9)                          | 1               | 34%                                        | 40%                                        | 33%                                                  | homog: full<br>vs standard:<br>reduced |

### 3.5 DISCUSSION

The tests that have been conducted to assess the capabilities of the homogenisation method have involved harsh conditions. Global models with low degrees of periodicity (high  $\eta$  - no smaller than 1/4) were used with fairly severe loading and boundary conditions. However, these tests have produced reasonably accurate results.

General stress distributions and stress magnitudes are well predicted by the homogenisation method - especially for compression loading of non-bending structures. Shear loading appears to result in slightly higher errors in the localisation predictions. In general, regions of high strain energy density are accurately predicted. However, high strains caused by localised boundary effects are under-predicted by the homogenisation method. Reduced levels of accuracy at the boundary have also been reported by Hollister *et al.* (1991 and 1992) and are to be expected since boundary constraints and non-uniform loading conditions tend to contradict the required assumption of periodicity that is inherent in the homogenisation solution. Errors caused by these localised boundary effects appear to drop off very sharply, and reasonable levels of accuracy are recovered at a distance of one base-cell length from the boundary.

In standard finite element analyses of slender structures which deform by some bending and which are modelled with linear 8-noded elements, the use of reduced integration results in better predictions of the bending deformations than the corresponding full integration predictions. The results of these tests have shown that this rule holds for the homogenisation method, since the apparent compressive stiffness of a structure which exhibits internal bending is significantly lower when lower order quadrature is used. However, using reduced integration for the calculation of tissue-level strains results in under-predictions of up to 20% (not caused by boundary effects) in regions of high strain. The reason for these higher levels of inaccuracy in the localisation calculations using reduced as opposed to full quadrature is unclear. One possible reason could be the influence of the periodic boundary conditions. It is likely that these periodic constraints tend to restrict the internal structures from deforming to a degree. This stiffening effect is perhaps shadowed by the additional artificial increases in bending stiffness caused by a full integration scheme. However, when reduced quadrature is used, the stiffening effect of the boundary conditions becomes more evident in the homogenisation solution when comparing tissue-level predictions to the direct finite element results.

Since bending is better predicted with a lower order integration rule, the direct finite element results using this scheme offer the highest accuracy. The reduced integration homogenisation results compare far more favourably with these standard results than the full quadrature homogenisation results. This indicates that, within the limitations of the homogenisation method, reduced integration provides the most accurate results when analysing base-cell structures which exhibit some internal bending.

---

## CHAPTER 4

# IDEALISED MODELS OF CANCELLOUS BONE USING THE HOMOGENISATION METHOD

---

In this chapter, the viability of creating realistic idealised models of cancellous bone is investigated. Previous work in this field is first reported and discussed. This is followed by a presentation of the development of representative finite element models of bone from the proximal tibia. The aim of this exercise was to create models which exhibit similar apparent mechanical behaviour to that reported for actual cancellous bone over a range of apparent densities. The base-cell models were analysed using the homogenisation technique and the apparent engineering constants extracted from the resultant apparent constitutive matrix. These predicted apparent elastic constants were then compared to experimental data.

As discussed in Chapters 1 and 2, cancellous bone from the proximal tibia has been chosen as a convenient region of bone to model for this feasibility study because of the availability of experimental data for this region.

### 4.1 PREVIOUS WORK

Much work on the application of the homogenisation method to the modelling of cancellous bone has been done by Scott J. Hollister and associates at the University of Michigan. Hollister *et al.* (1991) did numerical tests on simple idealised models of cancellous bone. They used the homogenisation method to calculate the apparent material properties of their structurally symmetric and isotropic base-cell structures which contained either cubic or spherical voids (Figure 4.1a-c). Predicted stiffness values were compared to experimental results for a range of bone specimens from different regions of the human anatomy. In general their results showed that the homogenisation of the idealised models over-predicted the stiffness of the cancellous bone specimens with the same apparent densities. The idealised models did not accommodate bending of the internal base-cell structures. A further limitation was that the structural isotropy of these models precluded the prediction of any orthotropic behaviour.

Hollister subsequently abandoned the idea of using idealised models of trabecular bone and later developed an homogenisation sampling procedure to calculate effective elastic properties of cancellous bone from digitised images of trabecular specimens. This computationally expensive technique involves the homogenisation of a large number of digitised trabecular specimens from a certain anatomical region and then calculating the average effective elastic properties from all the specimens. Hollister *et al.* (1994) conducted extensive numerical and experimental tests to investigate this technique. The apparent Young's moduli of 104 8mm cubic bone specimens were measured e

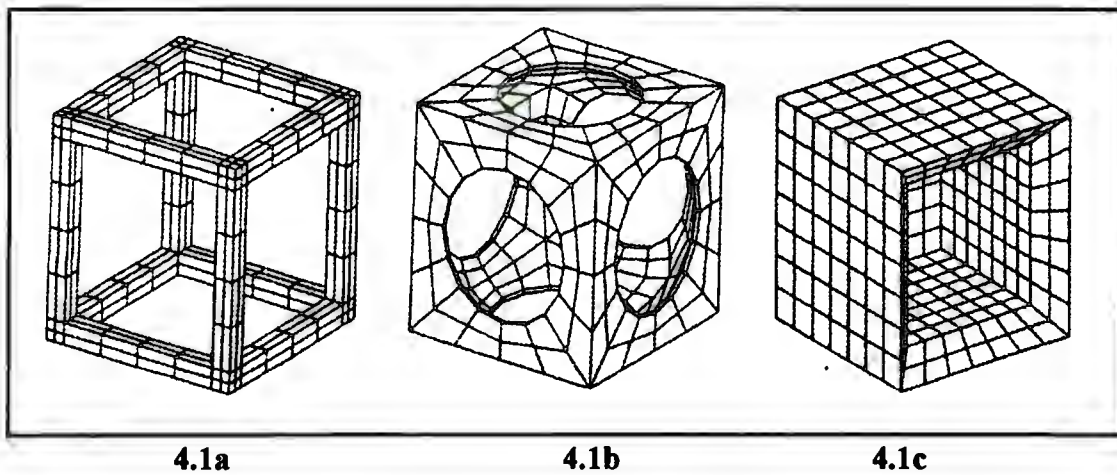


**FIGURE 4.1** Idealised models of cancellous bone (Hollister *et al.*, 1991)

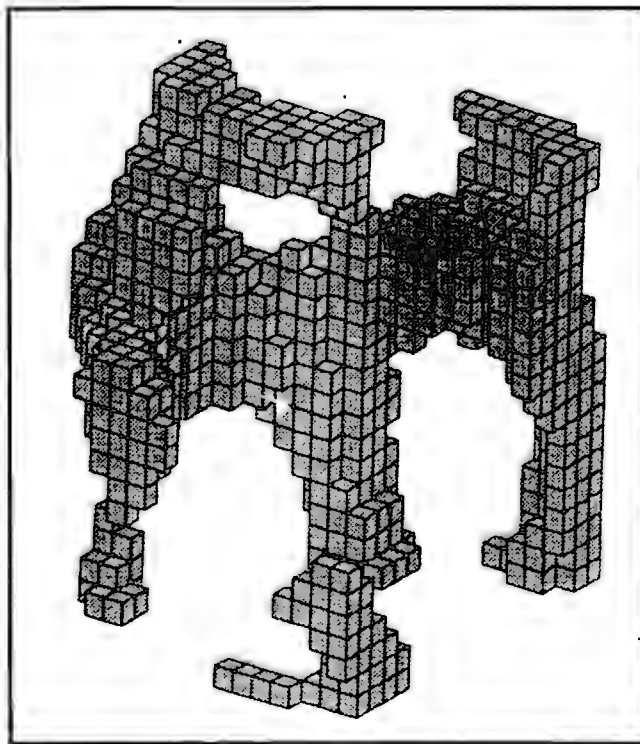


**FIGURE 4.2** Digitised 1mm cube sample of cancellous bone from lumbar spine (Hollister *et al.*, 1994)

experimentally. Each 8mm bone specimen was then digitised to produce 27 separate 1mm cubic base-cells of trabecular bone - randomly sampled within the 8mm bone specimen. These smaller samples were then discretised to create numerical base-cells. The base-cells were homogenised, and the resultant average predicted effective stiffness of the 27 base-cells was compared to the experimentally measured stiffness of the parent 8mm specimen. An example of one discretised base-cell is shown in Figure 4.2. The average effective stiffnesses of these digitised specimens were reasonably close to the experimentally measured values. In contrast to previous studies involving idealised models which always over-predicted the experimentally measured stiffness, these homogenised values under-predicted the experimental values by between 31% and 38% in all three orthogonal directions.

On the basis of their results for this analysis as well as their previous study which considered idealised cancellous bone models, the authors concluded that the wide variation in trabecular architecture may preclude the accurate prediction of effective stiffness of cancellous bone using idealised models based on assumed trabecular deformations. Indeed, their results would suggest that the homogenisation sampling procedure does provide more accurate predictions of effective stiffness for specific bone specimens. However, the possibility of generating more realistic idealised models of cancellous bone for specific anatomic regions has not been fully exhausted. The idealised models of Hollister *et al.* (1991) were simplistic and not representative of any typical cancellous bone architecture. No attempts have been made to accurately model the characteristic trabecular structures, and the predominant deformation modes have not been considered. As discussed in Chapter 2, both of these aspects have a significant influence on the effective mechanical behaviour of cancellous bone. Tiered, non face-to-face stacking of repeating structures, which has been observed in actual bone specimens (Beaupre and Hayes (1985)), has also not been incorporated in previous idealised models.

The digitised base-cells of Hollister *et al.* (1994), generated from actual specimens, were shown to have wide variations in architecture. As discussed in Chapter 2, the large random component in the structure of even the most region-specific bone has been well documented. Notwithstanding these random variations, it is widely accepted that specific regions do exhibit noticeable structural trends which have been characterised both qualitatively and quantitatively by various researchers. Thus it would seem reasonable to conclude that the biological mechanisms which control the formation and maintenance of cancellous bone in a specific region do aim at some ideal structure which exhibits certain apparent and local mechanical behaviours which are well suited (in terms of triaxial strength and impact absorption requirements) to that region. That these typical structural characteristics were not strongly evident in the digitally sampled structures of Hollister *et al.* might be explained by the fact that their 1mm cubic base-cells were too small to accommodate these basic structures. In Chapter 2, a number of studies are cited which report single repeating structural members which span distances greater than 5mm. The under-prediction of the apparent stiffnesses by the homogenisation sampling method is another indication that the typical structures occupy larger volumes than 1 cubic millimetre. One would expect the inherent over-stiffness of the finite element method (when using 8-noded brick elements to model structures which deform by some bending) to predict at least slightly higher stiffnesses than the experimental values. However, this was not the case for the digitised models. Thus the sample size which was used to create these base-cells was probably too small to represent any possible repeating

microstructures within the larger bone specimens, and so the incomplete base-cells were under-stiff.

The basic assumption of the homogenisation method is that the porous or composite material has a periodically repeating microstructure, and any variations in structure over the global domain are smooth and gradual. This requires that the base-cell be close to symmetric in structure. If this is not the case, any calculations of tissue-level quantities will be inaccurate because the imposed periodic boundary conditions on the base-cell are violated by the non face-to-face symmetry of the base-cell structure. Thus, although the averaged effective stiffness of randomly sampled, non-symmetric bone specimens is fairly well predicted using Hollister's homogenisation sampling method, any postprocessing of tissue strains or stresses would produce inaccurate results.

In this present study, the possibility of generating more realistic idealised models of cancellous bone by identifying a typical repeating structure within the bone is investigated. This is discussed in the next section.

## 4.2 IDEALISED FINITE ELEMENT MODELS OF CANCELLOUS BONE IN THE PROXIMAL TIBIA

Initially, simple models of proximal tibial cancellous bone were considered, including only the observed basic structural features of the actual bone. More realistic models were then developed by changing the models in order to make the structure and thus the mechanical behaviour approach that of actual cancellous bone. The homogenised apparent elastic properties of these models have been compared to the available experimental results. Attempts have been made to develop a range of base-cells to model a range of apparent densities. The development of the models is discussed in sections 4.2.1 - 4.2.5 below.

The observations and experimental evidence of Singh (1978) and Williams and Lewis (1982) on the structure and material behaviour of cancellous bone in the proximal tibia have been used as guidelines in the design of the idealised models. Singh categorised this region of bone as subtype IIIb (see section 2.1). The specific observations regarding this region of bone are repeated here. At high densities, the bone consists mainly of delicate plates (0.12-0.24mm thick) which form vertically orientated cylindrical-type closed-cell structures with diameters of 0.7-2.0mm. At lower densities, the plates acquire increasingly larger intertrabecular fenestrations, and the structure takes on the open-cell appearance of a network of interconnected rods. The basic cylindrical structure is evident over the entire range of densities. A sample of high density bone from this region is shown in Figures 4.3a-b (Williams and Lewis). The tubular structure is clearly visible in the transverse plane, and the vertical section shows that these cylindrical structures, which are about 4.5mm in length, have slightly elliptical shapes which allows the walls to bend under compressive loading.

In keeping with the more recent studies (Kuhn *et al.* (1989), Choi *et al.* (1990)), all idealised models in this study are assumed to have a solid phase Young's modulus of 5GPa and Poisson's ratio of 0.3.

The predicted engineering constants calculated by the homogenisation code for all base-cells are listed in tables in Appendix D. A summary of these results is given in Table 4.1. The results are reported for models using both full and reduced integration elements. The numerically predicted values of vertical stiffness are compared to the experimental values predicted by the best-fit cubic regression to the data of Williams and Lewis in Chapter 2. However, based on the work done by Keaveny *et al.* (1993), it can be assumed that Williams and Lewis' experimental results are systematically below the true values of apparent stiffness by between 45% and 70% owing to the effects of damage artefacts coupled with the specimen size and geometry that was used. There is no significant regression function for transverse stiffness. However, the accuracy of the homogenised values for transverse stiffness are compared indirectly to the experimental data by comparing the numerically predicted and experimentally measured ratios between vertical and transverse stiffness (i.e. by comparing the predicted and measured degrees of anisotropy). For high density cancellous bone in the proximal tibia ( $\rho > 0.25$ ), the experimentally measured ratio is about 7:1. At lower densities, where the vertical trabeculae exhibit more bending, this ratio is between 3:1 and 4:1 (Williams and Lewis (1982)).

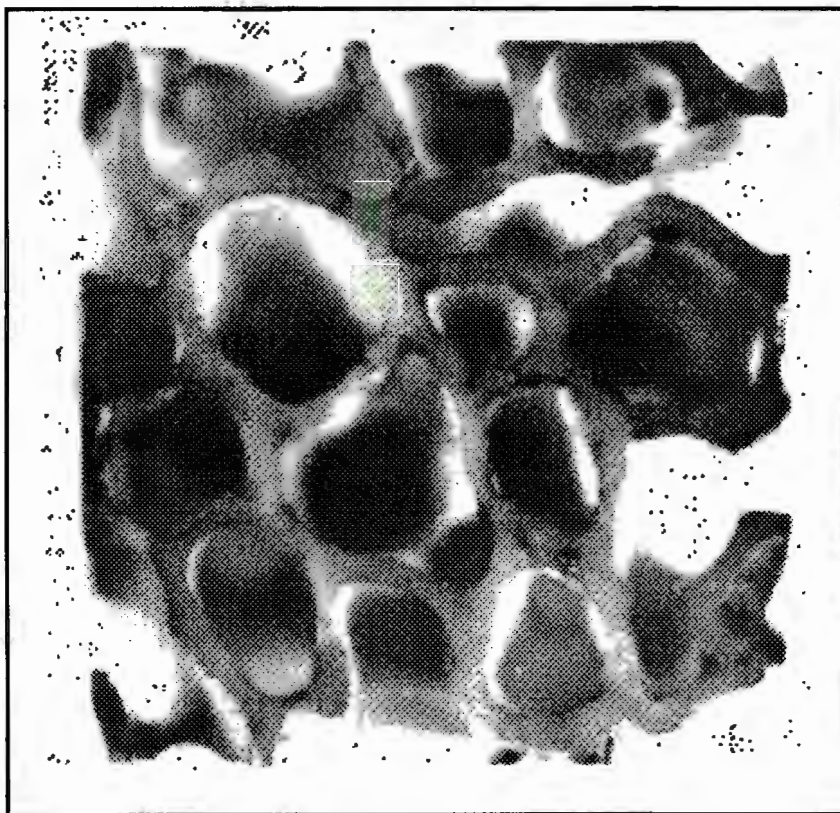


**FIGURE 4.3 a** Transverse view of high density bone from the proximal tibia, Williams and Lewis (1982)

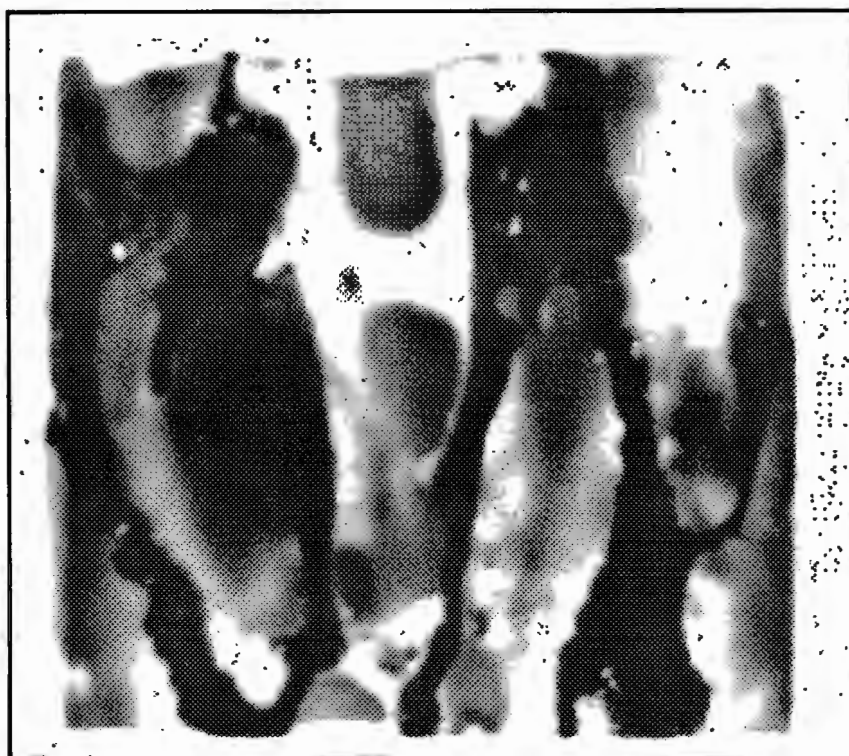


**FIGURE 4.3 b** Vertical view of high density bone from the proximal tibia, Williams and Lewis (1982)

### 4.2.1 MODEL I

The first, simple model of cancellous bone structure as a cylinder is shown in Figure 4.4. The 1.7mm long cylinder has an inner diameter of 1.35mm and a constant wall thickness of 0.18mm. The apparent density is 0.3.

The periodic boundary constraints, which are necessary for the homogenisation calculation of apparent material properties, are applied to this and all subsequent base-cells in the same way as described in Section 3.4.

The experimental value of vertical apparent stiffness (from the cubic regression curve) at  $\rho = 0.3$  is 70% less than the predicted homogenisation value for this first model - using full integration.

However, in the transverse directions, the experimental stiffness is more than 50% greater than the numerical prediction. The homogenised vertical stiffness using reduced integration remains unchanged, however the transverse stiffness is 30% less.

The high vertical stiffness can be attributed to the lack of vertical curvature in the walls of this structure, which prevents vertical bending. The absence of bending is confirmed by the fact that the predicted vertical stiffness does not drop when reduced integration is used. Furthermore, the actual value of the vertical stiffness is very close to the theory of mixtures prediction (which assumes pure axial compression, and is simply the transverse cross-sectional area multiplied by the solid material Young's modulus). The ratio of vertical to transverse stiffness using reduced integration is 48:1, compared to the experimental value of 7:1. This result indicates that some bending in the vertical direction must be accommodated, while the transverse bending stiffness should be increased.

### 4.2.2 MODEL II

Model I was modified to include a varying cross-sectional diameter in the transverse plane, from a maximum of 1.35mm at the top and bottom to a minimum of 0.95mm in the middle. This "cooling tower" type structure - illustrated in Figure 4.5 - allows bending to occur along the vertical axis. The apparent density of this model is 0.28.

The homogenisation results using full integration for this model are an improvement on the first attempt. The ratio of vertical to transverse stiffness is 8:1. The experimental prediction of vertical stiffness is 65% less than the homogenisation prediction. The reduced integration results show a huge drop of 95% in transverse stiffness, and a drop of only 3% in the vertical direction. The very low transverse stiffness is unrealistic, and is probably caused by the fact that there are only a few nodes which are constrained by the periodic boundary conditions in each transverse direction. This model probably has insufficient contact with the base-cell boundaries in the transverse plane, and so the predicted transverse stiffness is too low. Unlike the first model, this model has exhibited some vertical bending: the vertical stiffness is 23% lower than would be expected if axial compression was the only mode of deformation.

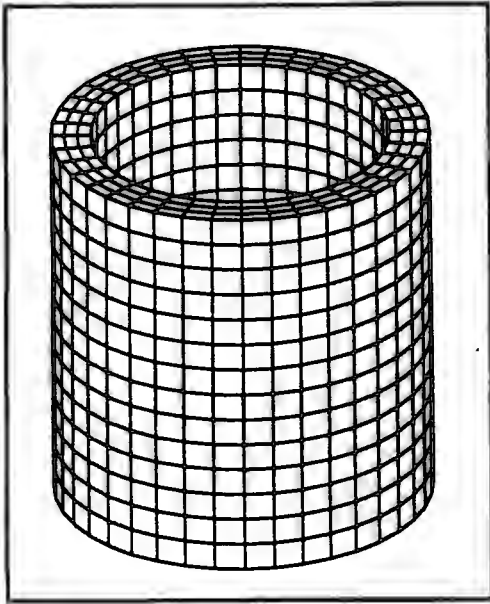


FIGURE 4.4 MODEL I

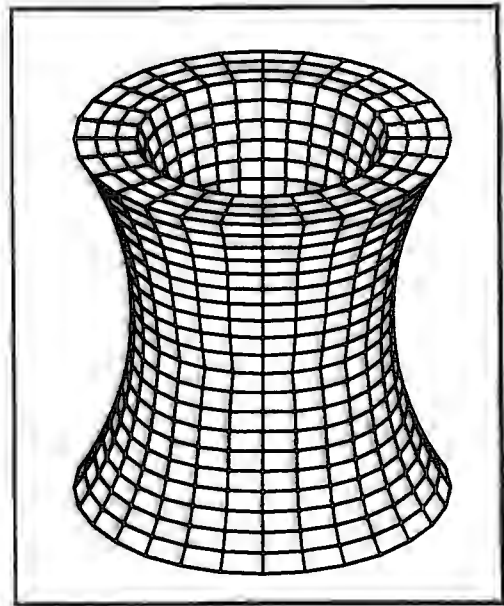


FIGURE 4.5 MODEL II

**TABLE 4.1 Homogenisation predictions of apparent Young's moduli of idealised models**

| Model | Density | Integration Rule | Predicted Vertical Stiffness (MPa) |               | Predicted Ratio of Vertical to Transverse Stiffness |              |
|-------|---------|------------------|------------------------------------|---------------|-----------------------------------------------------|--------------|
|       |         |                  | Homogenisation                     | Experimental* | Homogenisation                                      | Experimental |
| 1     | 0.3     | full             | 1472                               | 455 (1520)†   | 33:1                                                | 7:1          |
| 1     | 0.3     | reduced          | 1472                               |               | 48:1                                                |              |
| 2     | 0.28    | full             | 1117                               | 391 (1300)    | 8:1                                                 | 3:1 - 4:1    |
| 2     | 0.28    | reduced          | 1085                               |               | 55:1                                                |              |
| 3     | 0.35    | full             | 1579                               | 655 (2180)    | 4:1                                                 | 7:1          |
| 3     | 0.35    | reduced          | 1566                               |               | 6:1                                                 |              |
| 4     | 0.26    | full             | 852                                | 336 (1120)    | 6.4:1                                               | 4:1 - 7:1    |
| 4     | 0.26    | reduced          | 796                                |               | 8.6:1                                               |              |
| 5     | 0.15    | full             | 196                                | 158 (530)     | 2.2:1                                               | 3:1 - 4:1    |
| 5     | 0.15    | reduced          | 134                                |               | 2:1:1                                               |              |
| 6     | 0.15    | full             | 436                                | 158 (530)     | 4.4:1                                               | 3:1 - 4:1    |
| 6     | 0.15    | reduced          | 357                                |               | 6:1                                                 |              |

\* Experimental predictions from cubic regression fit to data of Williams and Lewis (1982)

† Values in parenthesis are maximum possible values assuming 70% under-measurement owing to systematic experimental errors (Keaveny *et al.* (1993))

### 4.2.3 MODEL III

When the base-cells from the first two models are stacked side by side, there are large gaps in-between the cylindrical structures. These gaps lead to low bending moduli in the transverse directions. The cancellous bone specimen in Figure 4.3 shows that adjacent tubular structures share common trabecular walls, and are generally not separated by gaps. Figure 4.6 shows the third model of cancellous bone from the proximal tibia. In this model the adjacent elliptical tubular-type structures share common walls so that there are no gaps between these major repeating structures which would artificially reduce the transverse stiffness. The Ellipsoid-type voids have maximum and minimum transverse diameters of 1.6mm and 0.7mm respectively, and the vertical length of these voids is 4.5mm. Wall thicknesses range from 0.15mm to 0.24mm. In an attempt to accommodate bending of the walls, the elliptical voids have been arranged so that the maximum transverse diameter of one void is surrounded by the minimum diameters of the adjacent voids. Consistent with observed architectural characteristics, this tiered stacking of the basic repeating structure ensures that at any cross-section in the transverse plane, the solid to void area fraction remains essentially constant. This model closely approximates the general structural features of actual high density proximal tibial cancellous bone, although none of the random variations are included, and there are no interconnecting holes or fenestrations between adjacent voids. As a result, the apparent density is high (0.35%). It was not practical to reduce the wall thicknesses of this model, since this would have resulted in highly distorted elements if the same level of mesh refinement was maintained. Furthermore, these wall thicknesses are consistent with observed values. There is no experimental data for such a high apparent density, and so extrapolation of the experimental correlation curve has been used to make comparisons with the experimental results. Although this base-cell has a slightly higher apparent density than that of the first two models, these densities are in same upper range, and so valid comparisons between the different apparent properties of these three base-cells can be made.

The experimental cubic regression curve predicts a vertical stiffness which is 59% less than the full integration homogenised prediction for this third model. This drops only 1% when reduced integration is used. Considering that the experimental value could be too low by up to 70%, this numerical result is within the probable range for high density cancellous bone. The ratio between vertical and transverse stiffness, using the reduced integration predictions, is 6:1 which is within the range of actual ratios for high density bone. Lower order quadrature produces significantly reduced stiffnesses (by more than 30%) in the transverse directions. These results indicate that while this structure still accommodates bending in the transverse directions, the vertical direction is again exhibiting mainly axial compression. This is confirmed by the fact that the theory of mixtures prediction of vertical stiffness is only 10% greater than the homogenisation prediction. This result is not necessarily unrealistic, since the cubic regression fit to Williams and Lewis' data suggests that at an apparent density as high as 0.35, bending modes would be far less predominant than at lower densities.

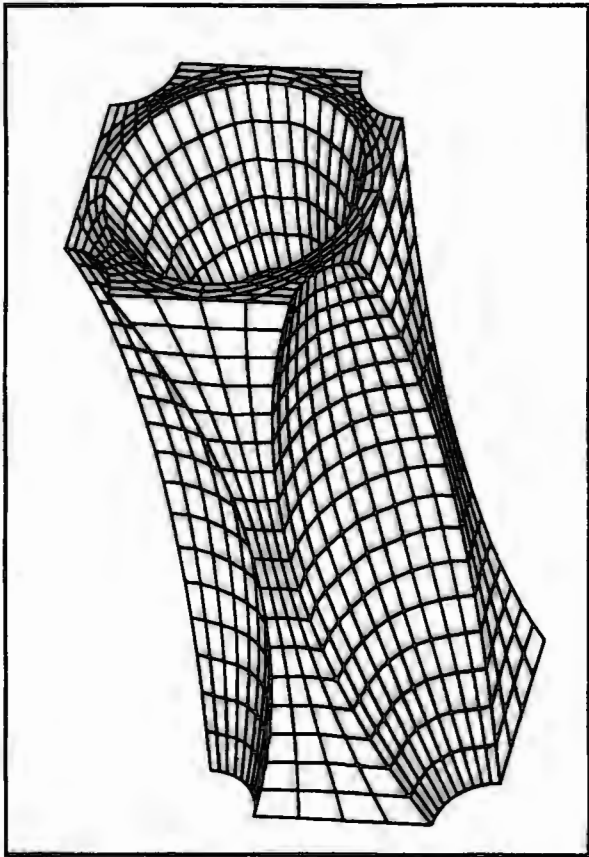


**FIGURE 4.6 MODEL III**

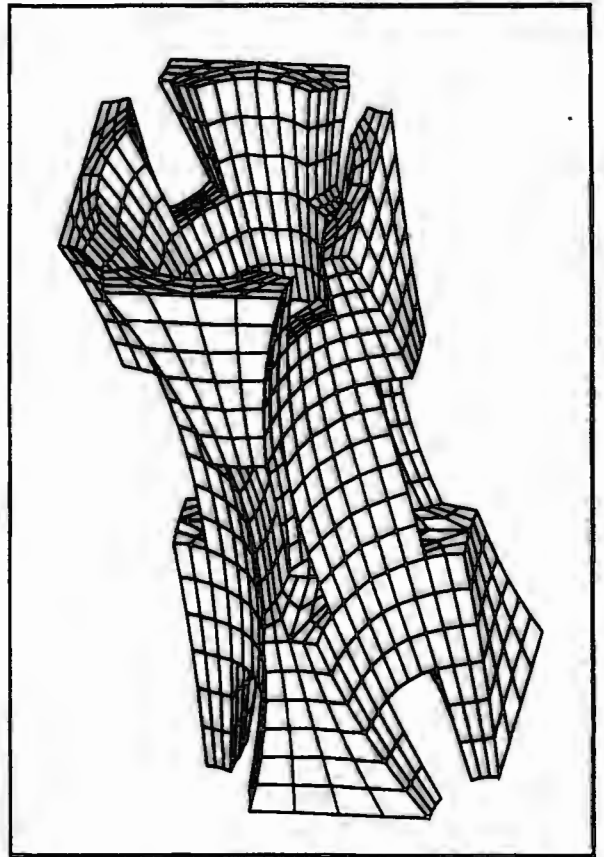


**FIGURE 4.7 MODEL IV**

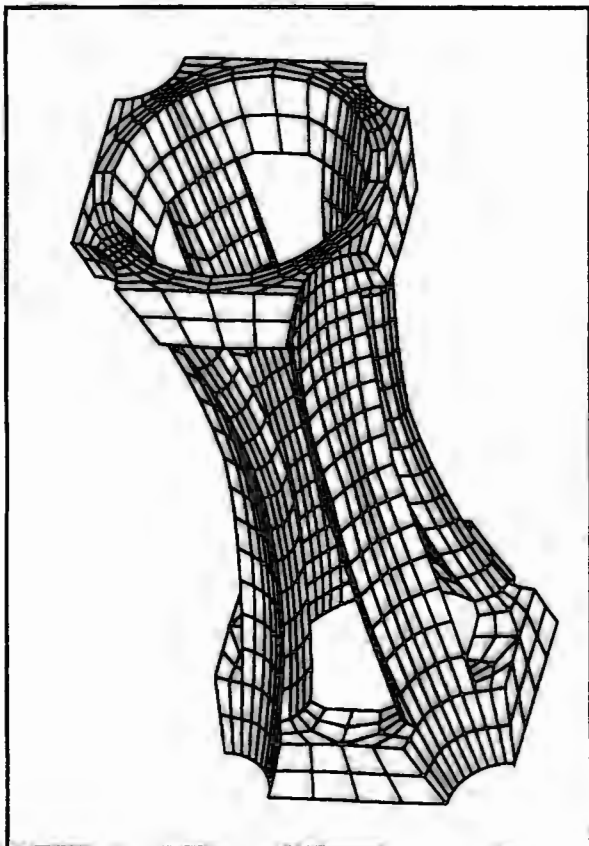


**FIGURE 4.8 MODEL V**

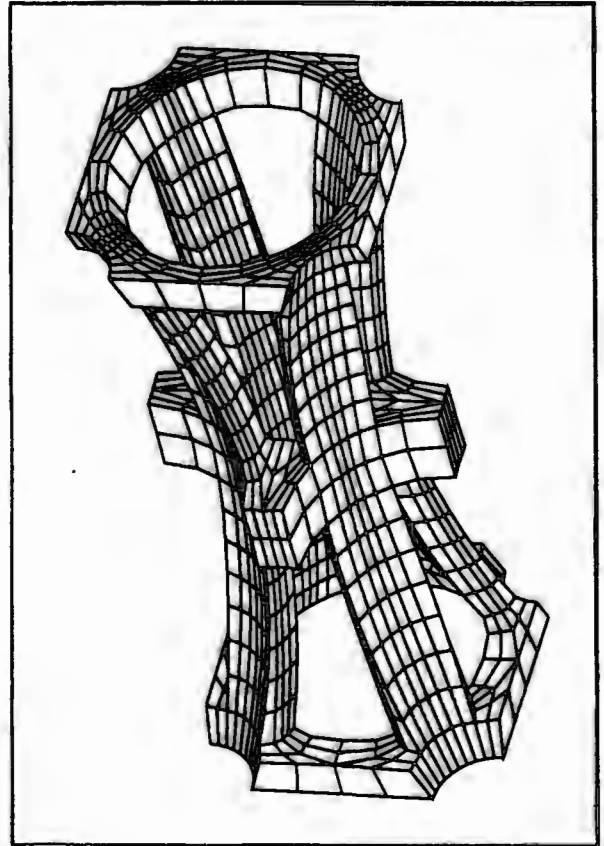


**FIGURE 4.9 MODEL VI**

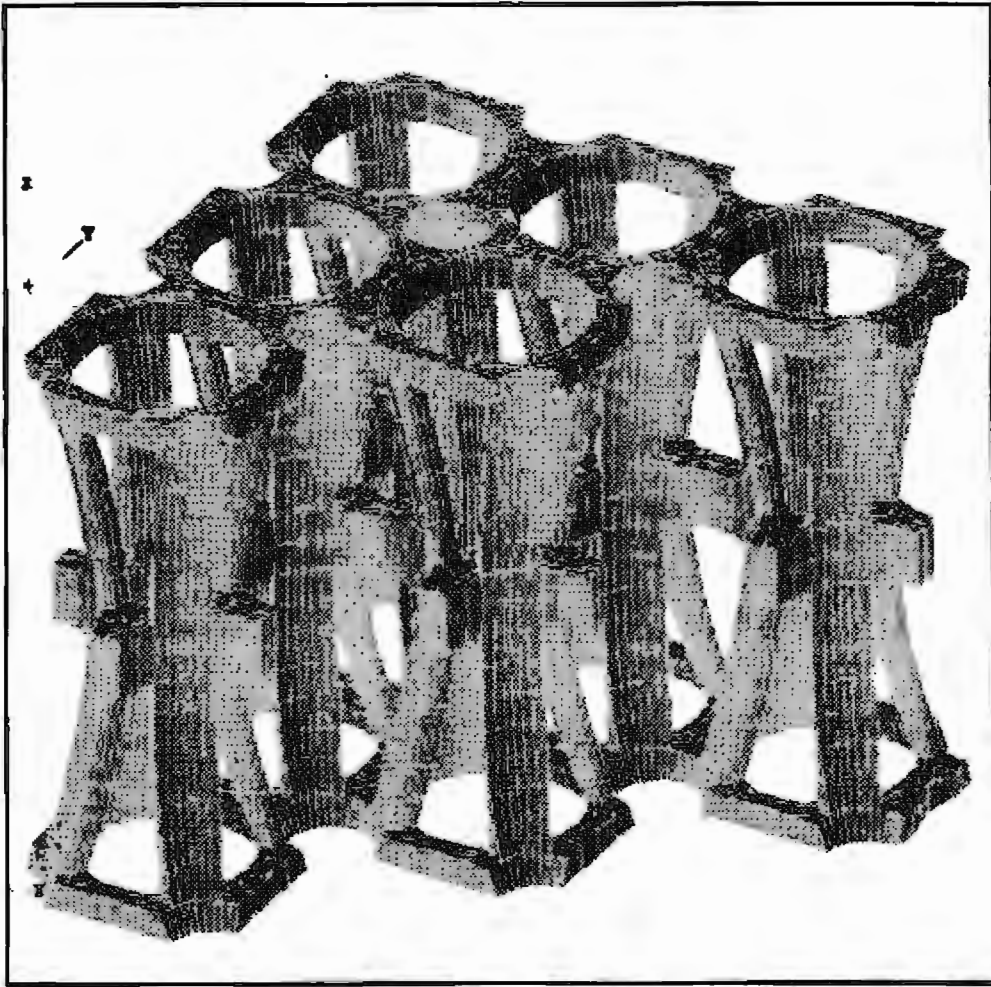


**FIGURE 4.10 a Oblique view of stacked base-cells (MODELVI)**

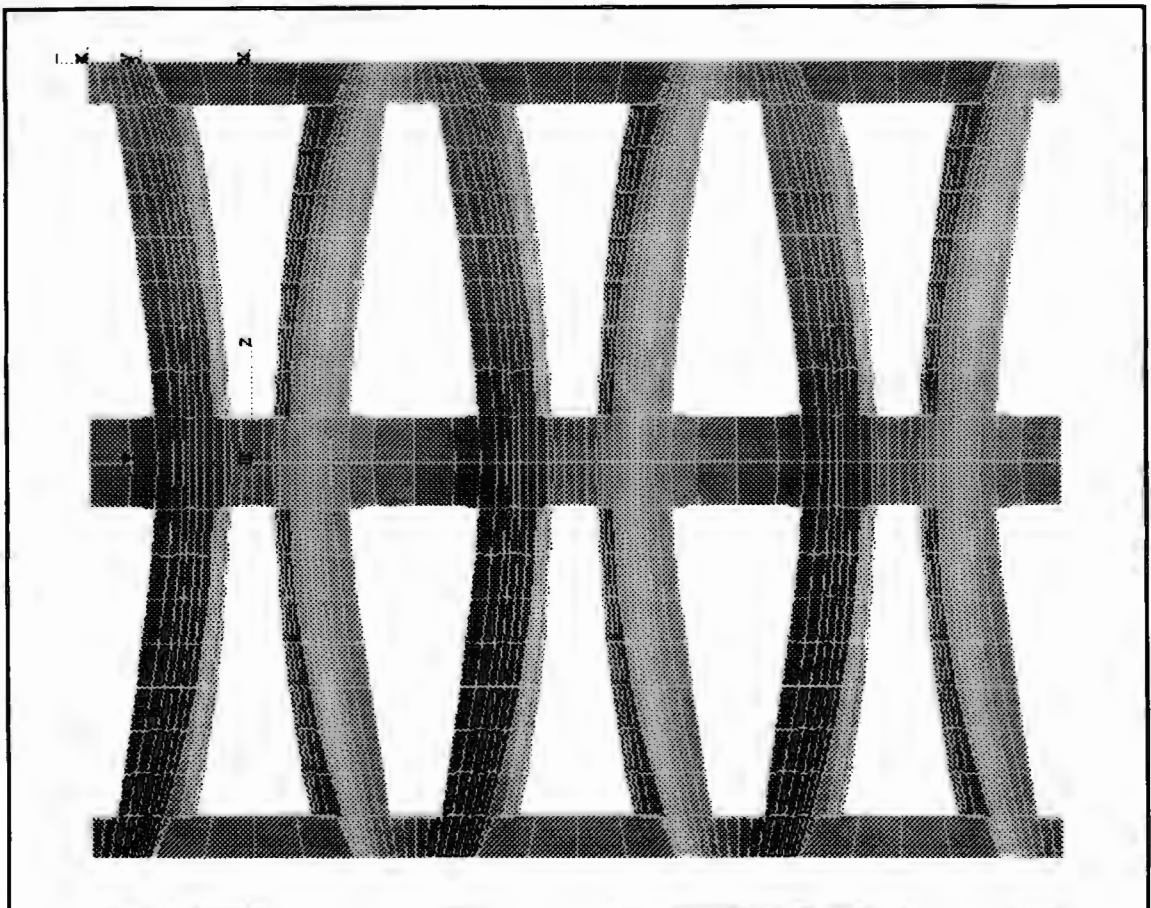


**FIGURE 4.10 b Vertical view of stacked base-cells (MODELVI)**

#### 4.2.4 MODEL IV

The fourth model investigates the predicted behaviour of a slightly lower density structure, where more vertical bending would occur compared to the previous model. This model has the same basic structure as model III, except some holes have been included between the voids. These holes or fenestrations were created by simply removing some of the elements in the common walls. In cancellous bone, the intertrabecular fenestrations are curved and blend in with the surrounding walls to reduce stress concentrations, and so the square holes with sharp corners in this model are simplistic. However, it has been assumed that these artificial holes adequately serve to reduce the apparent density and stiffness of the structure. The positioning and size of the fenestrations are arbitrary and were chosen for convenience with respect to the finite element mesh. The apparent density of this model (shown in Figure 4.7) is 0.26.

The predicted ratio of vertical to transverse stiffness for this idealised model is 6.4:1 for the full integration result and 8.6:1 using reduced quadrature. At this density the experimental ratio is in the range of 4:1 to 7:1. There is a difference of 8% in the predicted values of vertical stiffness between the two integration schemes. Furthermore, a 25% drop in solid volume, brought about by the introduction of fenestrations, has resulted in a 50% drop in vertical stiffness. These results indicate that some vertical bending does occur for this structure. The predicted values of transverse and vertical stiffness are also within the probable range determined from experimental evidence.

#### 4.2.5 MODEL V AND MODEL VI

The last two idealised models are for cancellous bone with low apparent densities. These models were again adapted from the basic closed-cell, elliptical-void structure of model III. Large fenestrations are included in these models to copy the typical structures of interconnected rods that are seen at low densities. The basic tubular characteristics have been maintained in accordance with the observations of Singh (1978) and Williams and Lewis (1982). These models are illustrated in Figures 4.8 and 4.9. Both models have an apparent density of approximately 0.15. An oblique and vertical view of a group of MODEL VI base-cells stacked side-by-side are shown in Figures 4.10 a and b. These pictures illustrate more clearly how the idealised base-cell models have been designed to copy the typical structures of the cancellous bone specimen shown in Figures 4.3 a and b.

The predicted vertical stiffnesses of the two models are quite different. Model V has a very low value, which is slightly lower than the corresponding experimental value. One would expect the actual stiffness at this low apparent density to be somewhat higher than the regression curve prediction because of the previously discussed experimental inaccuracies. The ratio of vertical to transverse stiffness is about 2:1 using both full and reduced integration. The drop in predicted stiffness from full to reduced integration is approximately 30% in both the vertical and transverse directions.

Model VI has a predicted vertical stiffness which is 166% greater than that of Model V, yet the transverse stiffness is about the same. The ratio of vertical to transverse stiffness for this model is 6:1 - using reduced integration. The higher value of vertical

stiffness for this model is expected since there is an additional transverse structure which essentially divides the length of the vertical bending structures in two, thereby increasing their bending stiffness. The volume of material which contributes to the transverse stiffness is similar in both models, and hence the predicted transverse stiffnesses are similar.

#### 4.2.6 REGRESSION ANALYSIS OF NUMERICAL RESULTS

The last four base-cell models have the same basic structure of model III. Interconnecting holes of different sizes have been included in this structure to achieve a range of apparent densities from 0.15 to 0.35. Regression curves have been fitted to this data for vertical and transverse stiffness versus apparent density. It has been assumed that the regression relations are smooth functions over the entire range of densities, and so each curve goes through the origin. A power law exponent of 1.7 is obtained if model VI is used for the low density data point. However if the predicted vertical stiffness of model V is used, the exponent rises to 2.9. The predicted exponent for the transverse data is only 1.6 - even though bending deformations predominate in this direction. Figure 4.11 shows the regression curves for vertical stiffness compared to the experimental results of Williams and Lewis (1982). The experimental data has three regression curves - all going through the origin. The first curve is fitted to the measured data for vertical stiffness, the second is to this data adjusted to account for the minimum expected error of 45%, and the third is for the same data adjusted to a maximum possible error of 70% (Keaveny *et al.* (1992)). The probable range of true Young's moduli lie between these last two adjusted experimental regression curves (i.e. the shaded area).

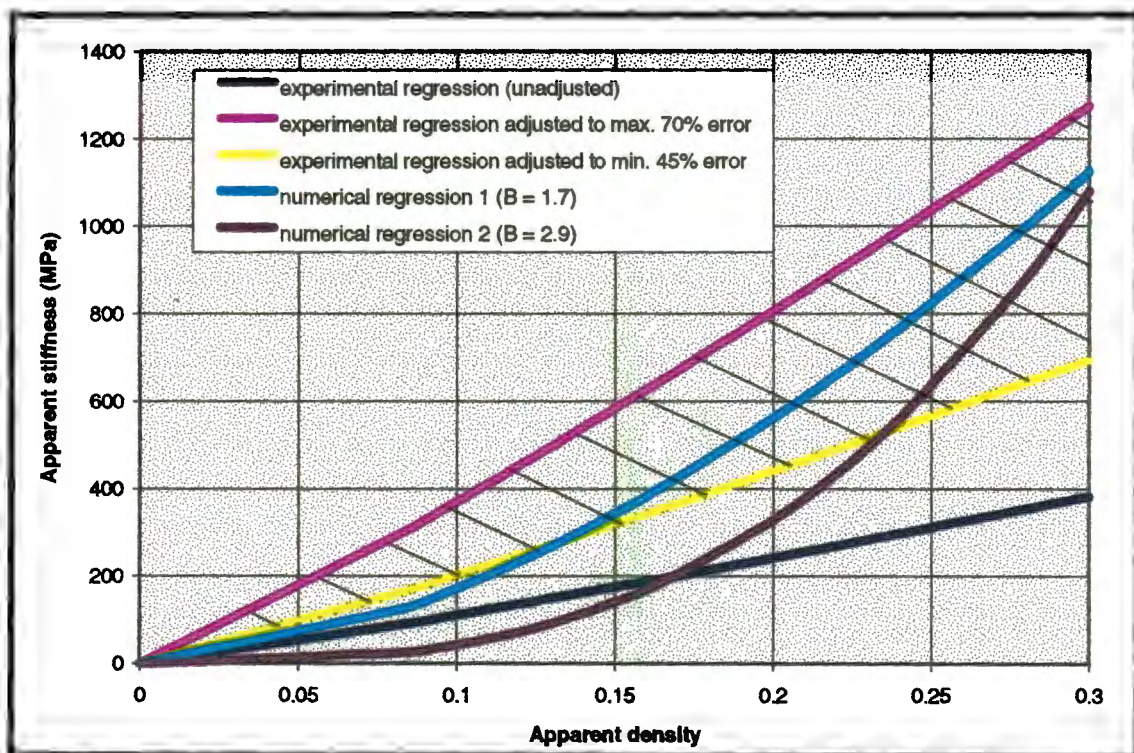
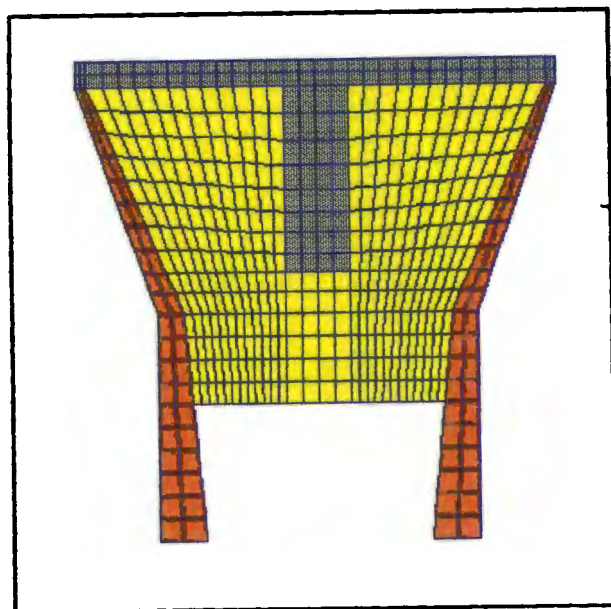


FIGURE 4.11 Regression curves to numerical predictions and experimental data of Williams and Lewis (1982) for vertical stiffness.

#### 4.2.7 GLOBAL KNEE MODEL

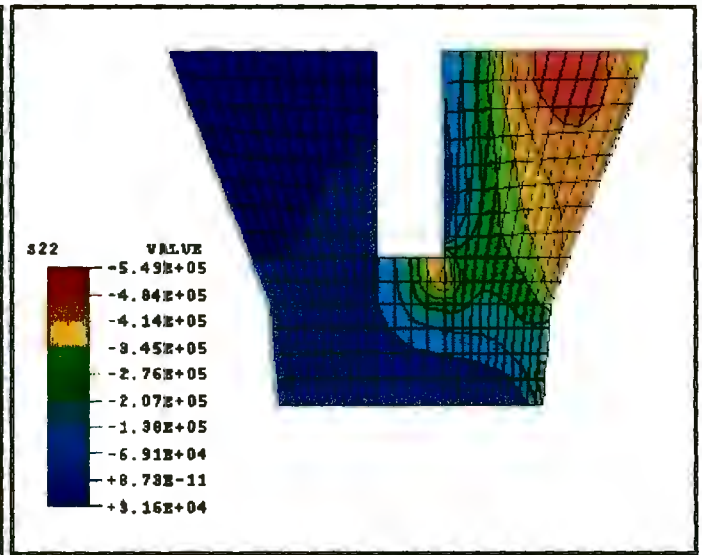
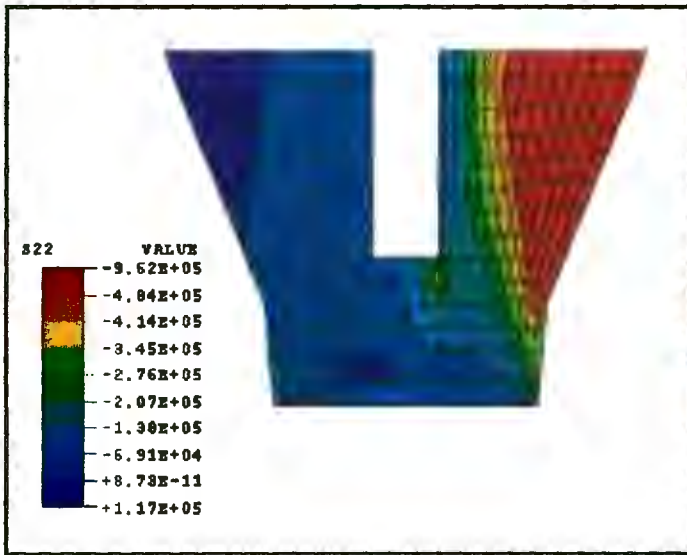
A simple global knee model with a cementless reconstructed articular surface was set up to investigate the different global behaviour when the cancellous bone is modelled with the apparent orthotropic material properties compared to isotropic properties.

The model (illustrated in Figure 4.12) was constructed with one layer of 8-noded elements. All nodes were constrained from moving in the out-of-plane direction to simulate a plane strain model. The grey region represents the steel tibial component which is perfectly bonded to the cancellous bone (in yellow). The orange region represents the cortex. This cortical region has been modelled with a high isotropic Young's modulus of 60GPa in an attempt to account for the hoop or cylindrical stiffening effect that is lost in this non-cylindrical model. The cancellous region was modelled first with the homogenised material constants calculated for MODEL VI (Table D12 in Appendix D), and then with an isotropic Young's modulus equal to the apparent vertical stiffness of MODEL VI and a Poisson's ratio of 0.3. These two models were loaded with an eccentric pressure on the upper left face of the metal component, and rigid body boundary conditions were applied to the base of the cortex.



**FIGURE 4.12 Simple global model of cementless reconstructed tibia**

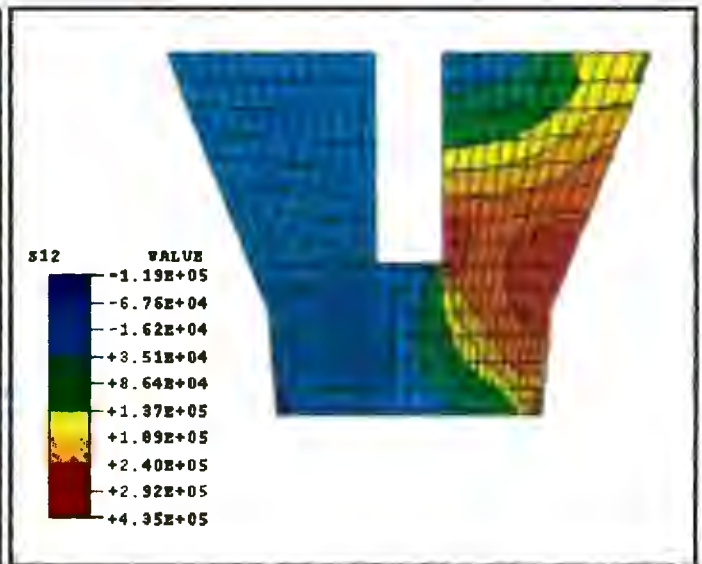
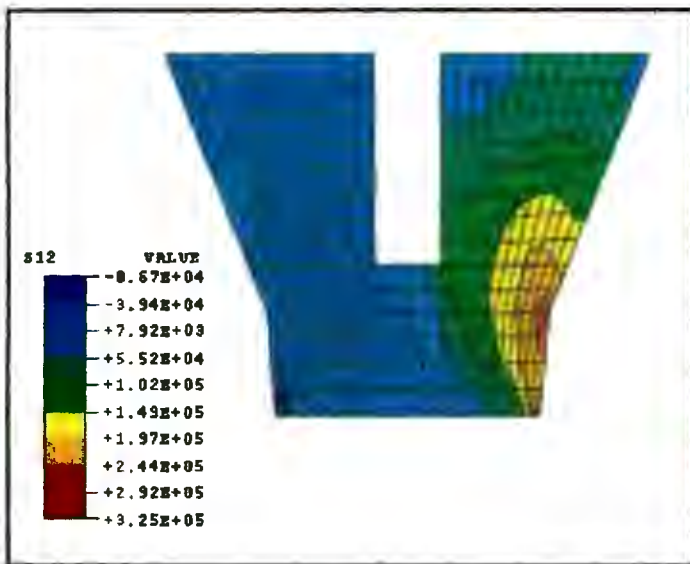
The results for these two global analyses are illustrated in Figures 4.13 and 4.14. Figure 4.13a shows the vertical axial stresses in the cancellous region of the orthotropic model, which are compared to the isotropic results in Figure 4.13b. The peak axial compressive stress in the isotropic model is 43% less than in the orthotropic model, and the stress gradients between the implant post and left cortical region are less severe. However, at the left-hand post tip the stress concentrations in the isotropic model are higher by up to 40% compared to the orthotropic model. Figures 4.14a and b compare the in-plane shear stresses in the cancellous regions for the two models. Here, the shear stresses in the orthotropic model are less than in the isotropic model by 25%, and the post-tip peak stresses are again considerably higher in the isotropic model by 190%.



**4.13a ORTHOTROPIC CANCELLOUS BONE**

**4.13b ISOTROPIC CANCELLOUS BONE**

**FIGURE 4.13 Vertical axial stresses in orthotropic and isotropic cancellous bone regions**



**4.14a ORTHOTROPIC CANCELLOUS BONE**

**4.14b ISOTROPIC CANCELLOUS BONE**

**FIGURE 4.14 In-plane shear stresses in orthotropic and isotropic cancellous bone regions**

### 4.3 DISCUSSION

The large discrepancies in documented experimental evidence, make it difficult to validate the predicted homogenised apparent elastic behaviour of idealised models of cancellous bone using all the experimental data. Although a full spectrum of the previously published experimental work has been considered and discussed in this thesis, the work of only two studies (Singh (1978) and Williams and Lewis (1982)) has been used as guidelines and as a means of comparison when designing the idealised models. However, where applicable, the results of other, more recent (and sometimes more accurate) work have been used to interpret the experimental observations and data of these two older studies. The advantage of using the work of Singh and Williams and Lewis was that their results provided quantitative data which could be used to make quantitative comparisons when assessing the behaviour of the idealised models.

The base-cell models were developed from simple basic structures to more sophisticated structures until the architecture and the apparent mechanical behaviour approached that of the actual bone. Although it was important to obtain models which exhibited apparent stiffnesses close to the expected values, it was considered more important that the overall orthotropic mechanical behaviour of these models was realistic. Although the actual stiffness magnitudes of the more sophisticated models are certainly within the expected range of values, they are consistently higher than the experimental data. In addition to the high probability that Williams and Lewis' experimental results are too low (see Chapter 2), there are a number of other possible reasons for these numerical over-predictions. Probably the most important factor is the fact that no attempt has been made to include the random aspects of actual bone in the idealised models. This would have been contrary to the base-cell requirements for the homogenisation technique and difficult to implement without introducing non-random bias in the structural models. Increased base-cell discretisation would also have reduced the over-stiffening effect of the finite element method. The inherent over-stiffness of eight-noded elements in bending was reduced by using lower order quadrature. As discussed in Chapter 2, the solid phase material properties of cancellous bone are highly variable. Thus the choice of material properties for the idealised models might have led to discrepancies between the numerical and experimental values of apparent stiffness. Williams and Lewis (1982) estimated a solid phase stiffness of 1.3GPa for their bone specimens. However, this calculation was based on the assumption that the vertical trabeculae deform by axial compression only. In this study a more realistic stiffness of 5GPa has been used.

The regression relations between apparent density and apparent stiffness that were found for models III to VI were highly sensitive to changes in single data values because there were only three data points for each regression. Therefore these actual calculated exponents cannot be compared to experimental evidence in order to validate the structures of the idealised models that have been developed. Nevertheless, some useful observations can be made from these results.

Although the two low density models, V and VI, ( $\rho = 0.15$ ) are constructed from the same basic structure, their homogenised vertical stiffnesses are quite different, and this difference results in a vastly different power law exponent. This result suggests that the regression exponent is highly dependent on the way in which the basic structure has been

altered or modified to create a range of apparent densities. Thus a reliable, experimentally observed relationship between apparent density and stiffness provides a very useful guide for ensuring that the idealised structural variations over a range of densities are consistent with actual variations in bone structure.

For all the idealised models, bending is the predominant mode of deformation in the transverse direction. Yet the predicted exponent relating apparent density to transverse stiffness is relatively low. Thus the value of the exponent does not necessarily give an indication of the amount of bending that occurs at any particular density. As suggested in Chapter 2, the exponent  $B$  in Equation (2.1), is more useful in giving an indication of how the proportions of bending and compression deformations within the structure vary over the range of densities. In the case of transverse structures, bending predominates over the entire range of densities, thus  $B$  should be fairly low. Whereas in the vertical direction, experimental evidence shows that bending is far less prevalent at high densities than at lower densities. Thus  $B$  is higher in this direction. The structural variations can thus be designed to affect a realistic relationship between stiffness and density over the range of densities. And the value of  $B$  should be used to check that any structural variations (e.g. changes in wall thickness, or increased/decreased intertrabecular holes) that are made to a basic idealised bone model in order to achieve a higher or lower density, are realistic.

The base-cell models that have been presented here are not necessarily the most accurate representations of cancellous bone architecture in the proximal tibia. Certainly, some improvements can be made to refine these structures. However, the results of this investigation have shown that by approximating the general structural characteristics of cancellous bone in a certain region, and by accommodating the correct proportions of deformation modes, idealised models can be developed which reasonably approximate the apparent anisotropic behaviour of the actual bone. The results of this study also suggest that basic idealised structures can be altered systematically to achieve a range of densities which exhibits an observed empirical relationship between apparent density and stiffness.

When cancellous bone is modelled realistically as an orthotropic material, compared to and isotropic material, the resultant global behaviour and stress distributions are significantly different. The results that were found for the simple global reconstructed tibia are similar to those found by Williams and Lewis (1982). The differences in the stresses in the orthotropic cancellous bone are not necessarily worse than the isotropic results (in terms of possible loosening, or unnatural bone remodelling). However, the altered stress distributions and magnitudes when cancellous bone is modelled more realistically will give a more accurate picture of the mechanical interaction of the implant and surrounding bone. This will lead to improved predictions of implant behaviour, and thus assist the process of implant design optimisation.

---

## CHAPTER 5

### CONCLUSIONS

---

This thesis has documented the work of an investigation into the feasibility of using the homogenisation method to create realistic idealised models of cancellous bone. Based on the findings of this work, the following conclusions are drawn:

- The microstructure and the apparent- and tissue-level mechanical properties of cancellous bone are highly variable and region-dependent. There is no general structure, and no specific relationship between apparent density and apparent stiffness which characterise all types of cancellous bone. However, there are certain specific regions of cancellous bone, such as the proximal tibia and distal femur which exhibit typical structural characteristics. These observed characteristics have a major influence on the apparent behaviour of the bone over the range of apparent densities. Thus, despite the large random component in the microstructures of all types of cancellous bone, there are certain regions which are suitable for idealised modelling.
- The homogenisation method is an accurate technique for the prediction of local strains in large global problems involving composites with periodically repeating microstructures. High levels of accuracy can be achieved in the prediction of local compressive strains. Although shear and bending strains are less accurately predicted than compressive strains, regions of high strain (not caused by local external boundary effects) can be expected to be within 20% of the standard finite element predictions for all load cases. Inaccuracies caused by global boundary effects do not recur throughout the global domain (as is the case for the standard mechanics homogenisation methods), and acceptable levels of accuracy are recovered at a distance of one base-cell length from the external boundary. When large bending or shear deformations occur within a base-cell, the use of lower order quadrature with hour glass control provides the most accurate prediction of true strain energy densities using the homogenisation method. These results indicate that the homogenisation method is a suitable technique for the global analysis of composite materials which undergo considerable internal bending and are highly anisotropic, such as cancellous bone. However, in order to produce accurate results with this technique, the base-cell structures must accurately represent the true microstructural nature of the actual material.
- It is indeed possible to create realistic idealised models of cancellous bone for specific regions. It is possible to simulate the apparent orthotropic material properties of cancellous bone reasonable accurately, provided the typical structures and the predominant deformation modes are well characterised. Since the idealised models in this study did not take the random variations in true bone structure into account, the homogenisation predictions of the apparent stiffness tended to be higher than the experimentally determined values. Also, the finite element method is overstiff - especially when a low level of discretisation is used. Notwithstanding these

limitations, this study has shown that idealised models can be developed to reasonably simulate the apparent orthotropic material properties of cancellous bone in the proximal tibia over the full range of apparent densities. Since these idealised models were achieved by modelling the observed microstructures of the actual bone, it is concluded (based on the original modelling assumption stated in Chapter 1) that these idealised models will reasonably accurately predict the actual tissue-level behaviour of true cancellous bone as well.

- Since cancellous bone from the proximal tibia can be realistically idealised, it can be concluded that idealised models can be developed for all regions of cancellous bone, provided they have typical repeating microstructures and exhibit specific deformation modes. Other regions of bone which would thus be well suited to idealised modelling include the distal femur, proximal femur, cervical vertebrae, and patella.
- The considerable differences in the global behaviour of cancellous bone when it is modelled realistically as an orthotropic material (albeit homogeneous) compared to a simplified isotropic material confirms the need for a more accurate modelling approach for this important region of bone. Ongoing improvements in artificial joint design will require more realistic modelling techniques. This study has shown that since cancellous bone can be modelled as an idealised material, the homogenisation method is a very useful tool for achieving higher levels of accuracy in the finite element analysis of reconstructed joints.

---

## REFERENCES

---

1. Abeyaratne R., Triantafyllidis N., An investigation of localisation in a porous elastic material using homogenisation theory, *J. Applied Mechanics*, **51**, 481-486, 1984.
2. Amstutz H.C., Sissons H.A., The structure of the vertebral spongiosa, *J. Bone Joint Surgery*, **51B**, 540-542, 1969.
3. Ashman R.B., Rho J.Y., Elastic modulus of trabecular bone material, *J. Biomechanics*, **21 (3)**, 177-181, 1988
4. Beaupre G.S., Hayes W.C., Finite element analysis of a three-dimensional open-celled model for trabecular bone, *ASME J. Biomechanical Engineering*, **107**, 249-256, 1985
5. Belytschko T., Kam liu W., Kennedy J.M., Shau-Jen Ong J., Hourglass control in Linear and nonlinear problems, 1983
6. Benssousan A., Lions J.L., Papanicoulau G., Asymptotic Analysis for Periodic Structures, North-Holland, Amsterdam, 1978
7. Carter D.R., Mechanical loading histories and cortical bone remodelling, *Calcified Tissue Int.*, **36**, S19-S24, 1984
8. Carter D.R., Hayes W.C., The compressive behaviour of bone as a two-phase porous structure, *J. Bone and Joint Surgery.*, **59A**, 954-962, 1977
9. Choi K., Kuhn J.L., Ciarelli M.J., Goldstein S.A., The elastic moduli of human subchondral, trabecular and cortical bone tissue and the size dependency of cortical bone modulus, *J. Biomechanics*, **23 (11)**, 1103-1113, 1990
10. Cook R.D., Malkus D.S. Plesha M.E. Concepts and Applications of Finite Element Analysis 3rd ed., John Wiley & Sons, 1989
11. Cowin S.C., Bone stress adaption models, *ASME J. Biomechanical Engineering*, **115**, 528-533, 1993
12. Ducheyne P., De Meester P., , Influence of a functional dynamic loading on bone ingrowth into surface pores of orthopedic implants, *J. Biomed. Mater. Res.*, **11**, 811-838, 1977
13. Galante J.O., Jacobs J., Clinical performances of ingrowth surfaces, *Clin. Orthop.*, **276**, 41-49, 1992
14. Gibson L. J., The mechanical behaviour of cancellous bone, *J. Biomechanics*, **18 (5)**, 317-328, 1985
15. Gibson L.J., Ashbey M.F., Cellular Solids, structures and properties, Pergamon Press, 1988

16. Goldstein S.A., The mechanical properties of trabecular bone: dependence on anatomic location and function, *J. Biomechanics*, **20 (11/12)**, 1055-1061, 1987
17. Goldstein S.A., Goulet R., McCubbrey D., Measurement and significance of three-dimensional architecture to the mechanical integrity of trabecular bone, *Calcified Tissue Int.*, **53**, 127-133, 1993
18. Goulet R.W., Goldstein S.A., Ciarelli M.J., Kuhn J.L., Brown M.B., Feldkamp L.A., The relationship between the structural and orthogonal compressive properties of trabecular bone, *J. Biomechanics*, **27 (4)**, 375-389, 1994
19. Guedes J.M., Kikuchi N., Preprocessing and postprocessing for materials based on the homogenisation method with adaptive finite element methods, *Computer Methods in Applied Mechanics and Engineering*, **83**, 143-198, 1990.
20. Harrigan T.P., Jasty M., Mann R.W., Harris W.H., Limitations of the continuum assumption in cancellous bone, *J. Biomechanics*, **21 (4)**, 269-275, 1988
21. Hill R., Elastic properties of composite materials - some theoretical principles, *J. Mech. Phys. Solids*, **11**, 357-372, 1963
22. Hinton E., Owen D.R.J., An Introduction to Finite Element Computations, Pineridge Press Limited, Swansea, 1979
23. Hodgkinson R., Currey J.D., Effects of structural variation on Young's modulus of non-human cancellous bone, *Journal of Engineering in Medicine* **204**, 43-52, 1990
24. Hollister S.J., Fyhrie D.P., Jepsen K.J., Goldstein S.A., Application of homogenization theory to the study of trabecular bone mechanics, *J. Biomechanics*, **24**, 825-839, 1991
25. Hollister S.J., Kikuchi N., A comparison of homogenisation and standard mechanics analyses for periodic porous composites, *Computational Mechanics* **10**, 73-95, 1992
26. Hollister S.J., Weissman D.E., McCubbrey D.A., A modelling procedure to evaluate vertebral body mechanics from trabecular microstructural properties, *39th Annual Meeting, Orthopaedic Research Society*, Feb. 1993
27. Hollister S.J., Brennan J.M., Kikuchi N., A homogenisation sampling procedure for calculating trabecular bone effective stiffness and tissue level stress, *J. Biomechanics*, **27**, 433-445, 1994
28. Hollister S.J., Kikuchi N., Goldstein S.A., Do bone ingrowth processes produce a globally optimized structure?, *J. Biomechanics*, **26**, 391-407, 1993
29. Keaveny T.M., Borchers R.E., Gibson L.J., Hayes W.C., Theoretical analysis of the experimental artifact in trabecular bone compressive modulus, *J. Biomechanics*, **26 (4/5)**, 599-607, 1993
30. Keaveny T.M., Borchers R.E., Gibson L.J., Hayes W.C., Trabecular bone modulus and strength can depend on specimen geometry, *J. Biomechanics*, **26 (8)**, 991-1000, 1993

31. Keaveny T.M., Gui E., Wachtel E.F., McMahon T.A., Hayes W.C., Trabecular bone exhibits fully linear elastic behaviour and yields at low strains, *J. Biomechanics*, **27** (9) 1127-1136, 1994
32. Ko C.C., Kohn D.H., Hollister S.J., Micromechanics of Implant Tissue Interfaces, *J. Oral Implantology*, **XVIII** (3), 220-230, 1992
33. Kohn D.H., Ko C.C., Hollister S.J., Effect of tissue modulus, symmetry and fibrous tissue on the local properties of a porous coating/tissue interfacial zone, *39th Annual Meeting, Orthopaedic Research Society*, Feb. 1993
34. Kohn D.H., Ko C.C., Hollister S.J., Coupled global/local modelling of porous coated implants: error estimates for different loading conditions, *39th Annual Meeting, Orthopaedic Research Society*, Feb. 1993
35. Kohn D.H., Ko C.C., Hollister S.J., Localised stress analysis of dental implants using homogenisation theory, *Advances in Bioengineering*, **22**, 607-610, 1992
36. Linde F., Hvid I., Stiffness behaviour of trabecular bone specimens, *J. Biomechanics*, **20** (1), 83-89, 1987
37. Linde F., Norgaard P., Hvid I., Odgaard A., Soballe K., Mechanical properties of trabecular bone. Dependency on strain rate, *J. Biomechanics*, **24**, 803-809, 1991
38. Linde F., Hvid I., Madsen F., The effect of specimen geometry on the mechanical behaviour of trabecular bone specimens, *J. Biomechanics*, **25** (4), 359-368, 1992
39. Mackerle J., Finite and boundary element techniques in biomechanics: a bibliography (1991-1993), *Finite Elements in Analysis and Design*, **16**, 163-174, 1994
40. Meguid S.A., Kalamkarov A.L., Asymptotic homogenisation of elastic composite materials with a regular structure, *Int. J. Solids Structures*, **31** (3) 303-316, 1994
41. Mente P.L., Lewis J.L., Experimental method for the measurement of the elastic modulus of trabecular bone tissue, *J. Orthopaedic Research*, **7**, 456-461, 1989
42. Miller I., Freund J.E., Probability and Statistics for Engineers ed. 3, Prentice-Hall, 1985
43. Mosekilde L., Vertebral structure and strength *in vivo* and *in vitro*, *Calcified Tissue Int.*, **53 suppl 1**, 121-126, 1993
44. Oxnard C.E., Bone and bones, architecture and stress, fossils and osteoporosis, *J. Biomechanics*, **26 suppl 1**, 63-79, 1993
45. Potter M.C., Foss J.F., Fluid Mechanics, John Wiley, New York, 1975
46. Pugh J.W., Rose R.M., Radin E.L., A structural model for the mechanical behaviour of trabecular bone, *J. Biomechanics*, **6**, 657-670, 1973

47. Rho, J.Y., Ashman R.B., Turner C.H., Young's modulus of trabecular and cortical bone material: ultrasonic and microtensile measurements, *J. Biomechanics*, **26 (2)**, 111-119, 1993
48. Rice J.C., Cowin S.C., Bowman J.A., On the dependence of the elasticity and strength of cancellous bone on apparent density, *J. Biomechanics*, **21 (2)**, 155-168, 1988
49. Ryan S.D., Williams J.L., Tensile testing of rodlike trabeculae excised from bovine femoral bone, *J. Biomechanics*, **22 (4)**, 351-355, 1989
50. Santosa F., Symes W.W., A model for a composite with anisotropic dissipation, *Int. J. Solids Structures*, **25 (4)**, 381-392, 1989
51. Sigmund O., Materials with prescribed constitutive parameters: an inverse homogenisation problem, *Int. J. Solids Structures*, **31 (17)**, 2313-2329, 1994
52. Singh I., The architecture of cancellous bone, *J. Anatomy.* , **127 (2)**, 305-310, 1978
53. Snyder B.D., Hayes W.C., Multiaxial structure-property relations in trabecular bone, 1990
54. Snyder B.D., Piazza S., Edwards W.T., Hayes W.C., Role of trabecular morphology in the etiology of age-related vertebral fractures, *Calcified Tissue Int.*, **53 (suppl 1)**, 14-22, 1993
55. Townsend P.R., Rose R.M., Radin E.L., Buckling studies of single human trabeculae, *J. Biomechanics* **8**, 199-201, 1975
56. Townsend P.R., Raux P., Rose R.M., Miegel R.E., Radim E.L., The distribution and anisotropy of the stiffness of cancellous bone in the human patella, *J. Biomechanics*, **8**, 363-367, 1975
57. Williams J.L., Lewis J.L., Properties and an Anisotropic model of cancellous bone from the proximal tibial epiphysis, *ASME J. Biomechanical. Engineering.*, **104**, 50-56, 1982.
58. Whitehouse W.J., Dyson E.D., Scanning electron microscope studies of trabecular bone in the proximal end of the human femur, *J. Anat*, **118 (3)**, 417-444, 1974
59. Williams J.L., Lewis J.L., Properties and an anisotropic model of cancellous bone from the proximal tibial epiphysis, *ASME J. Biomech. Eng.*, **104**, 51-56, 1982

---

## APPENDIX A

### Definition of the Sample Correlation Coefficient

---

The sample correlation coefficient,  $r$ , is defined by Miller and Freund (1985) as:

$$r = \frac{S_{xy}}{\sqrt{S_{xx} \cdot S_{yy}}}$$

for  $n$  pairs of values  $(x_i, y_i)$

$$\text{where } S_{xx} = n \sum_{i=1}^n x_i^2 - \left( \sum_{i=1}^n x_i \right)^2$$

$$S_{yy} = n \sum_{i=1}^n y_i^2 - \left( \sum_{i=1}^n y_i \right)^2$$

$$S_{xy} = n \sum_{i=1}^n y_i x_i - \left( \sum_{i=1}^n x_i \right) \left( \sum_{i=1}^n y_i \right)$$

For a statistical regression fit to a set of  $x, y$  data the value  $r$  indicates that  $100r^2\%$  of the variation among the  $y$  data values is explained by, or accounted for, or attributed to corresponding differences among the  $x$  data values.

---

## APPENDIX B

### Theory of Homogenisation

---

A summary of the formal derivation of homogenisation theory (Guedes and Kikuchi (1992)) is detailed here.

As discussed in Chapter 3, the asymptotic expression for the periodic displacement field,  $\mathbf{u} = (u_1, u_2, u_3)^T$ , of a composite material can be written:

$$\mathbf{u}(\mathbf{x}, \mathbf{y}) = \mathbf{u}_0(\mathbf{x}, \mathbf{y}) + \eta \mathbf{u}_1(\mathbf{x}, \mathbf{y}) + \eta^2 \mathbf{u}_2(\mathbf{x}, \mathbf{y}) + \dots \quad (\text{B1})$$

where  $\mathbf{x}$  is the global coordinate vector,  
 $\mathbf{y}$  is the local, base-cell coordinate vector - related to  $\mathbf{x}$   
 by  $\mathbf{y} = \mathbf{x}/\eta$

And for some function  $\mathbf{g}(\mathbf{x}, \mathbf{y}) = \mathbf{g}(\mathbf{x}, \mathbf{x}/\eta)$ , using the chain rule:

$$\frac{d\mathbf{g}}{d\mathbf{x}} = \frac{\partial \mathbf{g}}{\partial \mathbf{x}} + \frac{1}{\eta} \frac{\partial \mathbf{g}}{\partial \mathbf{y}} \quad (\text{B2})$$

The equation for global-level (overall) equilibrium of a body with external tractions,  $t_i$  on boundary  $\Gamma$ , using virtual work, can be written in indicial notation as:

$$\int_{\Omega} \mathbf{D}_{ijkl} \frac{\partial u_k}{\partial x_l} \frac{\partial v_i}{\partial x_j} d\Omega = \int_{\Gamma} t_i v_i d\Gamma \quad (\text{B3})$$

where  $v_i$  is the virtual displacement  
 $\mathbf{D}_{ijkl}$  is the fourth order constitutive tensor

This is equivalent to Equation (3.6) in Chapter 3. Expanding this using the chain rule and the asymptotic expression for displacements (B1) - considering only the first and second order displacement terms for simplicity, gives:

$$\int_{\Omega} \mathbf{D}_{ijkl} \left\{ \begin{aligned} & \frac{1}{\eta^2} \frac{\partial u_{0k}}{\partial y_l} \frac{\partial v_i}{\partial y_j} + \frac{1}{\eta} \left[ \left( \frac{\partial u_{0k}}{\partial x_l} + \frac{\partial u_{1k}}{\partial y_l} \right) \frac{\partial v_i}{\partial y_j} + \frac{\partial u_{0k}}{\partial y_l} \frac{\partial v_i}{\partial x_j} \right] \\ & + \left[ \left( \frac{\partial u_{0k}}{\partial x_l} + \frac{\partial u_{1k}}{\partial y_l} \right) \frac{\partial v_i}{\partial x_j} + \frac{\partial u_{1k}}{\partial x_l} \frac{\partial v_i}{\partial y_j} \right] \end{aligned} \right\} d\Omega = \int_{\Gamma} t_i v_i d\Gamma \quad (\text{B4})$$

This equation holds if the terms of the same order are equal to zero. Thus, in the limit as  $\eta \rightarrow 0$ , (B4) can be separated into three equations:

terms of order  $O(1/\eta^2)$ :

$$\frac{1}{\eta^2} \int_{\Omega} \mathbf{D}_{ijkl} \frac{\partial u_{0k}}{\partial y_l} \frac{\partial v_i}{\partial y_j} d\Omega = 0 \quad (\text{B5})$$

terms of order  $O(1/\eta)$ :

$$\frac{1}{\eta} \int_{\Omega} \mathbf{D}_{ijkl} \left[ \left( \frac{\partial u_{0k}}{\partial x_l} + \frac{\partial u_{1k}}{\partial y_l} \right) \frac{\partial v_i}{\partial y_j} + \frac{\partial u_{0k}}{\partial y_l} \frac{\partial v_i}{\partial x_j} \right] d\Omega = 0 \quad (\text{B6})$$

terms of order  $O(1)$ :

$$\int_{\Omega} \mathbf{D}_{ijkl} \left[ \left( \frac{\partial u_{0k}}{\partial x_l} + \frac{\partial u_{1k}}{\partial y_l} \right) \frac{\partial v_i}{\partial x_j} + \frac{\partial u_{1k}}{\partial x_l} \frac{\partial v_i}{\partial y_j} \right] d\Omega = \int_{\Gamma} t_i v_i d\Gamma \quad (\text{B7})$$

According to the definition of the global and local coordinate systems, if the global dimensions are of order 1, then the base-cell dimensions are of order  $\eta$ . Therefore, the traction term in (B7) is of the order  $O(1)$  because the function  $t_i$  describes the global boundary tractions which are independent of the base-cell dimensions (and thus independent of  $\eta$ ).

For Equation (B5) to hold for all  $v(x,y)$ ,  $u_0$  must be a function of the global coordinate system,  $x$ , only. The formal proof is given by Guedes and Kikuchi (1992). This result implies that the third term in the left-hand integrand of (B6) is zero. Therefore Equation (B6) becomes:

$$\int_{\Omega} \mathbf{D}_{ijkl} \left( \frac{\partial u_{0k}}{\partial x_l} + \frac{\partial u_{1k}}{\partial y_l} \right) \frac{\partial v_i}{\partial y_j} d\Omega = 0 \quad (\text{B8})$$

This is the equilibrium expression at the local, base-cell level, and is equivalent to Equation (3.8) in Chapter 3. The first and second terms in the brackets correspond to the apparent and fluctuation strains, respectively. This equilibrium expression is solved to find the fluctuation strains in terms of the apparent strain (i.e. the localisation step).

Now considering Equation (B6), and choosing  $v$  to be a function of the global coordinate system,  $x$ , only, the third term in square brackets on the left-hand side is zero:

$$\int_{\Omega} \mathbf{D}_{ijkl} \left( \frac{\partial u_{0k}}{\partial x_l} + \frac{\partial u_{1k}}{\partial y_l} \right) \frac{\partial v_i}{\partial x_j} d\Omega = \int_{\Gamma} t_i v_i d\Gamma \quad (\text{B9})$$

This is equivalent to (B3) which is the expression for global equilibrium. Using the periodicity requirement and the relation between apparent and fluctuation strains (from (B8) or (3.8)), this can be shown to be equivalent to Equation (3.11) in Chapter 3.

---

## APPENDIX C

### Tables of results for numerical homogenisation trials

---

| RANGE OF<br>% ERROR IN SED | % OF TOTAL<br>NUMBER OF ELEMENTS |
|----------------------------|----------------------------------|
| 0-10%                      | 75.0%                            |
| 10-20%                     | 12.5%                            |
| 20-30%                     | 3.1%                             |
| 30-50%                     | 5.2%                             |
| 50-100%                    | 2.1%                             |
| > 100%                     | 2.1%                             |

Maximum percentage error in SED for all elements with actual SED values within 20% of the maximum is 5.1%

**Table C1 Results for innermost base-cell (Section 3.4.1)  
(full integration)**

| RANGE OF<br>% ERROR IN SED | % OF TOTAL<br>NUMBER OF ELEMENTS |
|----------------------------|----------------------------------|
| 0-10%                      | 67.7%                            |
| 10-20%                     | 14.6%                            |
| 20-30%                     | 2.1%                             |
| 30-50%                     | 6.8%                             |
| 50-100%                    | 6.8%                             |
| > 100%                     | 2.1%                             |

Maximum percentage error in SED for all elements with actual SED values within 20% of the maximum is: 5.4%

**Table C2 Results for innermost base-cell (Section 3.4.2)  
(full integration)**

| RANGE OF<br>% ERROR IN SED | % OF TOTAL<br>NUMBER OF ELEMENTS |
|----------------------------|----------------------------------|
| 0-10%                      | 37.5%                            |
| 10-20%                     | 32.3%                            |
| 20-30%                     | 12.5%                            |
| 30-50%                     | 11.5%                            |
| 50-100%                    | 5.2%                             |
| > 100%                     | 1.0%                             |

Maximum percentage error in SED for all elements with actual SED values within 20% of the maximum is: 14.0%

**Table C3 Results for innermost base-cell (Section 3.4.2)  
(reduced integration)**

| RANGE OF<br>% ERROR IN SED | % OF TOTAL<br>NUMBER OF ELEMENTS |
|----------------------------|----------------------------------|
| 0-10%                      | 26.4%                            |
| 10-20%                     | 22.9%                            |
| 20-30%                     | 15.4%                            |
| 30-50%                     | 15.6%                            |
| 50-100%                    | 11.4%                            |
| > 100%                     | 8.3%                             |

Maximum percentage error in SED for all elements with actual SED values within 20% of the maximum is: 51.0%

**Table C4 Results for all base-cells (Section 3.4.3)  
(reduced integration)**

| RANGE OF<br>% ERROR IN SED | % OF TOTAL<br>NUMBER OF ELEMENTS |
|----------------------------|----------------------------------|
| 0-10%                      | 31.7%                            |
| 10-20%                     | 18.0%                            |
| 20-30%                     | 12.8%                            |
| 30-50%                     | 16.0%                            |
| 50-100%                    | 13.2%                            |
| > 100%                     | 8.5%                             |

Maximum percentage error in SED for all elements with actual SED values within 20% of the maximum is: 53.7%

**Table C5 Results for all base-cells (Section 3.4.3)  
(full integration)**

| RANGE OF<br>% ERROR IN SED | % OF TOTAL<br>NUMBER OF ELEMENTS |
|----------------------------|----------------------------------|
| 0-10%                      | 50.9%                            |
| 10-20%                     | 22.0%                            |
| 20-30%                     | 9.4%                             |
| 30-50%                     | 8.7%                             |
| 50-100%                    | 4.7%                             |
| > 100%                     | 4.2%                             |

Maximum percentage error in SED for all elements with actual SED values within 20% of the maximum is: 15.9%

**Table C6 Results for all base-cells (Section 3.4.4)  
(reduced integration)**

| RANGE OF<br>% ERROR IN SED | % OF TOTAL<br>NUMBER OF ELEMENTS |
|----------------------------|----------------------------------|
| 0-10%                      | 26.6%                            |
| 10-20%                     | 24.5%                            |
| 20-30%                     | 2.1%                             |
| 30-50%                     | 23.4%                            |
| 50-100%                    | 23.4%                            |
| > 100%                     | 0.0%                             |

Maximum percentage error in SED for all elements with actual SED values within 20% of the maximum is: 17.8%

**Table C7 Results for single base-cell (Section 3.4.5)  
(reduced integration)**

| RANGE OF<br>% ERROR IN SED | % OF TOTAL<br>NUMBER OF ELEMENTS |
|----------------------------|----------------------------------|
| 0-10%                      | 40.4%                            |
| 10-20%                     | 23.4%                            |
| 20-30%                     | 0.0%                             |
| 30-50%                     | 17.0%                            |
| 50-100%                    | 19.2%                            |
| > 100%                     | 0.0%                             |

Maximum percentage error in SED for all elements with actual SED values within 20% of the maximum is: 1.6%

**Table C8 Results for single base-cell (Section 3.4.5)  
(full integration)**

| RANGE OF<br>% ERROR IN SED | % OF TOTAL<br>NUMBER OF ELEMENTS |
|----------------------------|----------------------------------|
| 0-10%                      | 23.4%                            |
| 10-20%                     | 10.6%                            |
| 20-30%                     | 4.3%                             |
| 30-50%                     | 21.3%                            |
| 50-100%                    | 23.4%                            |
| > 100%                     | 17.0%                            |

Maximum percentage error in SED for all elements with actual SED values within 20% of the maximum is: 33.4%

**Table C9 Results for single base-cell (Section 3.4.5)  
(homogenisation analysis: reduced integration,  
versus standard analysis: full integration)**

## APPENDIX D

### Tables of Homogenised engineering constants for idealised bone models

```

*****
ENGINEERING CONSTANTS
FROM HOMOGENISED
BASE CELL MODEL I
*****
E11: 43.7 MPa
E22: 43.7 MPa
E33: 1472.3 MPa

v12: 0.85
v13: 0.3
v21: 0.85
v23: 0.3
v31: 0.9E-02
v32: 0.9E-02

G12: 86.8 MPa
G23: 246.8 MPa
G13: 246.8 MPa
*****
    
```

**TABLE D1 MODEL I**  
(Full Integration)

```

*****
ENGINEERING CONSTANTS
FROM HOMOGENISED
BASE CELL MODEL I
*****
E11: 30.6 MPa
E22: 30.6 MPa
E33: 1472.3 MPa

v12: 0.65
v13: 0.30
v21: 0.65
v23: 0.30
v31: 0.63E-02
v32: 0.63E-02

G12: 59.5 MPa
G23: 195.9 MPa
G13: 195.7 MPa
*****
    
```

**TABLE D2 MODEL I**  
(Red. Integration)

```

*****
ENGINEERING CONSTANTS
FROM HOMOGENISED
BASE CELL MODEL II
*****
E11: 135.2 MPa
E22: 137.4 MPa
E33: 1116.6 MPa

v12: 0.38
v13: 0.43
v21: 0.38
v23: 0.42
v31: 0.52E-01
v32: 0.52E-01

G12: 80.2 MPa
G23: 127.8 MPa
G13: 123.6 MPa
*****
    
```

**TABLE D3 MODEL II**  
(Full Integration)

```

*****
ENGINEERING CONSTANTS
FROM HOMOGENISED
BASE CELL MODEL II
*****
E11: 6.5 MPa
E22: 6.4 MPa
E33: 1085.3 MPa

v12: 0.34E-01
v13: 0.43
v21: 0.34E-01
v23: 0.43
v31: 0.3E-02
v32: 0.3E-02

G12: 3.2 MPa
G23: 5.8 MPa
G13: 3.8 MPa
*****
    
```

**TABLE D4 MODEL II**  
(Red. Integration)

```

*****
ENGINEERING CONSTANTS
FROM HOMOGENISED
BASE CELL MODEL III
*****
E11: 387.5 MPa
E22: 387.5 MPa
E33: 1578.6 MPa

v12: 0.64
v13: 0.30
v21: 0.64
v23: 0.30
v31: 0.7E-01
v32: 0.7E-01

G12: 286.7 MPa
G23: 381.3 MPa
G13: 381.3 MPa
*****
    
```

**TABLE D5 MODEL III**  
(Full Integration)

```

*****
ENGINEERING CONSTANTS
FROM HOMOGENISED
BASE CELL MODEL III
*****
E11: 261.8 MPa
E22: 261.8 MPa
E33: 1566.3 MPa

v12: 0.75
v13: 0.30
v21: 0.75
v23: 0.30
v31: 0.5E-01
v32: 0.5E-01

G12: 274.7 MPa
G23: 375.4 MPa
G13: 375.4 MPa
*****
    
```

**TABLE D6 MODEL III**  
(Red. Integration)

```

*****
ENGINEERING CONSTANTS
FROM HOMOGENISED
BASE CELL MODEL IV
*****
E11: 133.0 MPa
E22: 133.0 MPa
E33: 8515.0 MPa

v12: 0.68
v13: 0.21
v21: 0.68
v23: 0.21
v31: 0.3E-01
v32: 0.3E-01

G12: 82.3 MPa
G23: 71.8 MPa
G13: 71.8 MPa
*****

```

TABLE D7 MODEL IV  
(Full Integration)

```

*****
ENGINEERING CONSTANTS
FROM HOMOGENISED
BASE CELL MODELIV
*****
E11: 93.0 MPa
E22: 93.0 MPa
E33: 796.3 MPa

v12: 0.76
v13: 0.18
v21: 0.76
v23: 0.18
v31: 0.2E-01
v32: 0.2E-01

G12: 66.7 MPa
G23: 56.7 MPa
G13: 56.7 MPa
*****

```

TABLE D8 MODEL IV  
(Red. Integration)

```

*****
ENGINEERING CONSTANTS
FROM HOMOGENISED
BASE CELL MODEL V
*****
E11: 87.9 MPa
E22: 87.9 MPa
E33: 196.0 MPa

v12: 0.66
v13: 0.7E-01
v21: 0.66
v23: 0.7E-01
v31: 0.3E-01
v32: 0.3E-01

G12: 39.5 MPa
G23: 6.4 MPa
G13: 6.4 MPa
*****

```

TABLE D9 MODEL V  
(Full Integration)

```

*****
ENGINEERING CONSTANTS
FROM HOMOGENISED
BASE CELL MODEL V
*****
E11: 64.3 MPa
E22: 64.3 MPa
E33: 133.9 MPa

v12: 0.74
v13: 0.5E-01
v21: 0.74
v23: 0.5E-01
v31: 0.3E-01
v32: 0.3E-01

G12: 29.7 MPa
G23: 4.9 MPa
G13: 4.9 MPa
*****

```

TABLE D10 MODEL V  
(Red. Integration)

```

*****
ENGINEERING CONSTANTS
FROM HOMOGENISED
BASE CELL MODEL VI
*****
E11: 100.2 MPa
E22: 100.2 MPa
E33: 433.7 MPa

v12: 0.59
v13: 0.17
v21: 0.59
v23: 0.17
v31: 0.4E-01
v32: 0.4E-01

G12: 27.3 MPa
G23: 27.1 MPa
G13: 27.1 MPa
*****

```

TABLE D11 MODEL VI  
(Full Integration)

```

*****
ENGINEERING CONSTANTS
FROM HOMOGENISED
BASE CELL MODEL VI
*****
E11: 58.8 MPa
E22: 58.8 MPa
E33: 356.5 MPa

v12: 0.73
v13: 0.14
v21: 0.73
v23: 0.14
v31: 0.2E-01
v32: 0.2E-01

G12: 19.0 MPa
G23: 21.7 MPa
G13: 21.7 MPa
*****

```

TABLE D12 MODEL VI  
(Red. Integration)

---

## APPENDIX E

### User Information on Homogenisation Code

---

The homogenisation code, called HFEP3, uses a frontal solver which has been adapted to solve for the six "load" vectors simultaneously. The large demands on memory brought about by these changes to the code made it necessary to change the allocation of data in the solution routine from memory to disk space. This, combined with the fact that there is no element numbering optimisation in the code has resulted in a fairly slow solution time. A base-cell of 2000 elements typically takes up to two hours to run to completion on a RISK 6000 370 IBM. The complex base-cell meshes are generated using the ABAQUS preprocessor, ABAPRE (Hibbit *et al.* (1994)). A separate code, INTRFACE, was written to change the format of the ABAQUS input deck to a file which is compatible with the input format of HFEP3. The periodic boundary constraints are defined in ABAPRE using pin-type multi-point constraints which force corresponding nodes on opposite faces of the base-cell to have the same displacements in each of the three nodal degrees of freedom. These multi-point constraint definitions are sorted into sets of master and slave nodes in INTRFACE. The required format of the base-cell input deck is listed below.

READING: HFEP3.DAT INPUT DECK

number of nodes, elements, materials, problem type, number of nodes per element  
 number of constrained nodes, integration rule, number of master-slave definitions

64 26 1 4 8 1 2 19

element definitions

element, material, 8 node numbers

|    |   |    |    |    |    |    |    |    |    |
|----|---|----|----|----|----|----|----|----|----|
| 1  | 1 | 1  | 5  | 6  | 2  | 17 | 21 | 22 | 18 |
| 2  | 1 | 2  | 6  | 7  | 3  | 18 | 22 | 23 | 19 |
| 3  | 1 | 3  | 7  | 8  | 4  | 19 | 23 | 24 | 20 |
| 4  | 1 | 5  | 9  | 10 | 6  | 21 | 25 | 26 | 22 |
| 5  | 1 | 6  | 10 | 11 | 7  | 22 | 26 | 27 | 23 |
| .  |   |    |    |    |    |    |    |    |    |
| .  |   |    |    |    |    |    |    |    |    |
| .  |   |    |    |    |    |    |    |    |    |
| 22 | 1 | 38 | 42 | 43 | 39 | 54 | 58 | 59 | 55 |
| 23 | 1 | 39 | 43 | 44 | 40 | 55 | 59 | 60 | 56 |
| 24 | 1 | 41 | 45 | 46 | 42 | 57 | 61 | 62 | 58 |
| 25 | 1 | 42 | 46 | 47 | 43 | 58 | 62 | 63 | 59 |
| 26 | 1 | 43 | 47 | 48 | 44 | 59 | 63 | 64 | 60 |

nodal coordinates

nodes, x y z coords

|    |           |           |           |
|----|-----------|-----------|-----------|
| 1  | .0000000  | .0000000  | .0000000  |
| 2  | .3333330  | .0000000  | .0000000  |
| 3  | .6666670  | .0000000  | .0000000  |
| 4  | 1.0000000 | .0000000  | .0000000  |
| 5  | .0000000  | .3333330  | .0000000  |
| 6  | .3333330  | .3333330  | .0000000  |
| .  |           |           |           |
| .  |           |           |           |
| 60 | 1.0000000 | .6666670  | 1.0000000 |
| 61 | .0000000  | 1.0000000 | 1.0000000 |
| 62 | .3333330  | 1.0000000 | 1.0000000 |
| 63 | .6666670  | 1.0000000 | 1.0000000 |
| 64 | 1.0000000 | 1.0000000 | 1.0000000 |

rigid body constraint

node, degrees of freedom constrained (all three)

1 1 2 3

master-slave definitions

master node, number of slaves, degrees of freedom (all three)

1 7 1 1 1

slave nodes

|     |     |     |     |     |     |     |
|-----|-----|-----|-----|-----|-----|-----|
| 4,  | 13, | 49, | 16, | 52, | 61, | 64, |
| 2   | 3   | 1   | 1   | 1   |     |     |
| 14, | 50, | 62, |     |     |     |     |
| 33  | 3   | 1   | 1   | 1   |     |     |
| 36, | 45, | 48, |     |     |     |     |
| .   |     |     |     |     |     |     |
| .   |     |     |     |     |     |     |
| 34  | 1   | 1   | 1   | 1   |     |     |
| 46, |     |     |     |     |     |     |
| 35  | 1   | 1   | 1   | 1   |     |     |
| 47, |     |     |     |     |     |     |
| 37  | 1   | 1   | 1   | 1   |     |     |
| 40, |     |     |     |     |     |     |
| 41  | 1   | 1   | 1   | 1   |     |     |
| 44, |     |     |     |     |     |     |

material properties

Young's modulus, Poisson's ratio

00000000.0000000 0.299999999999999989

When HFEP3 is run, there is an option to do either a full homogenisation run (i.e. calculation of apparent constitutive matrix,  $\mathbf{D}_{app}$ ), or just a postprocessing of apparent strains (i.e. calculation of tissue-strains within the base-cell using Equation (3.16)). As mentioned, the homogenisation step is generally a lengthy one for complex microstructures, and so the  $\chi^k$  matrices are stored in a separate .fil file to avoid having to repeat this step when postprocessing various apparent strain states.

The homogenisation code that was developed for this study uses only 8-noded cubic elements which are over-stiff in bending when full quadrature is used. However, with reduced integration this over-stiffening effect is reduced. And so this integration scheme is better suited to structures (such as cancellous bone) which undergo some internal bending under compressive loads.

When using reduced integration, a degree of diagonal decay was reported during the homogenisation solutions for the base-cells which had internal bending members, indicating incipient zero-energy or hour-glass modes. Hughs (1987) gives a detailed description of this phenomenon. The possibility of serious round-off errors owing to the diagonal decay in the solutions made it necessary to implement an hour glass control algorithm in the homogenisation code.

The basic problem of hour-glassing is that when reduced integration is used to calculate the element stiffness matrix there are certain element deformation modes which have no stiffness associated with them. Thus, if these modes are not constrained by external boundary conditions, they will be activated - resulting in deformations which are not caused by any externally applied loads. This will result in a singular solution. The basic philosophy of hour glass control algorithms is to augment each element stiffness matrix with a set of artificial stiffness matrices which give each of the zero energy modes some stiffness. The hour glass stiffness terms must be large enough to prevent hour-glassing but small enough to have only a negligible effect on any legitimate modes of deformation. There are different ways of introducing these hour glass stiffnesses. However a comprehensive investigation into these methods was not undertaken for this thesis as it was not within the scope of this work. Belytschko *et al.* (1983) presented a method which introduces the hour-glass stiffness by including additional terms in the strain displacement B-matrix. This method takes into account the shape of the element. It is well suited to non-linear problems because the calculation of the internal force residual takes the modified B-matrix into account, and so convergence is achieved in the conventional way. This method would also be suitable for the homogenisation technique: By introducing the hour glass stiffness in the B-matrix the equilibrium in Equation (3.14) is maintained without unnecessarily affecting the relationship between apparent strain and fluctuation strain. However, for this thesis a less sophisticated method has been used which involves simply adding appropriate terms to each element stiffness matrix. Although this approach might lead to greater inaccuracies in the results, the hour-glass terms were kept small enough to keep any inaccuracies to within acceptable levels. This method is described by Cook *et al.* (1989). For an 8-noded hexahedral element there are twelve spurious zero energy modes. Thus there are twelve independent artificial stiffness matrices associated with each hour glass mode.

These standard artificial stiffness matrices are calculated in the homogenisation code and are weighted for each element according to the element volume and shear modulus (element shape is not taken into account). In addition, the artificial matrices are multiplied by a scale factor,  $F_{HG}$ , which can be adjusted to ensure that the stiffness terms are neither too high nor too low. For base-cells which exhibit no internal bending under compressive loads (such as the base-cell that was used in the first four homogenisation trials in Chapter 3) no hour glass control is required. But the more internal bending that occurs, the greater  $F_{HG}$  must be to prevent hour-glassing.

The homogenisation and localisation subroutines (HOMOG and TISSUE) in the finite element homogenisation code HFEP3 are listed below. The full code is stored on the floppy disk in the back of this thesis. The codes INTRFACE and ERRORS - the results postprocessing code - are also stored on this disk.

#####

SUBROUTINE HOMOG

#####

IMPLICIT DOUBLE PRECISION (A-H,O-Z)

INCLUDE 'fep3.inc'

PARAMETER

1( MNODE=9 ,MDIME=3 ,MDOFN=3 ,MPROP=11 ,MGAUS=3 ,  
2 MSTRE=6 ,MEVAB=24 ,MTOTG=9 )

PARAMETER

1( MTOTV=MDOFN\*MPOIN )

COMMON/CONTRL/

1 NDOFN ,NELEM ,NEVAB ,NGAUS ,NMATS ,  
2 NNODE ,NPOIN ,NPROP ,NTOTG ,NTOTV ,  
3 NVFIX ,NSTRE ,NTYPE ,NDIME ,NAXIS

COMMON/CORE /

2 IFFIX(MTOTV) ,FIXED(MTOTV,1)  
4 ELOAD(MEVAB,MELEM,MSTRE) ,EVOLUME(MELEM)

COMMON/DATAIN/

1 MATNO(MELEM) ,LNODS(MELEM,MEVAB) ,COORD(MPOIN,MDIME) ,  
2 NOFIX(MVFIX) ,PRESC(MVFIX,MDOFN) ,  
3 PROPS(MMATS,MPROP) ,MASTER(MTOTV)

COMMON/GAUSSD/

1 POSGP(MGAUS) ,WEIGP(MGAUS)

COMMON/SHAPES/

1 SHAPE(MNODE) ,DERIV(MDIME,MNODE) ,CARTD(MDIME,MNODE) ,  
2 GPCOD(MDIME,MTOTG)

COMMON/RESULT/

1 TDISP(MTOTV,6)

COMMON/VOLUMES/

1 TVOLUME, BVOLUME

DIMENSION

1 BMATX(MSTRE,MEVAB) ,DMATX(MSTRE,MSTRE) ,  
2 ELCOD(MDIME,MNODE) ,ESTIF(MEVAB,MEVAB) ,  
4 ELDIS(MDOFN,MNODE) ,DUMMY(6,6) ,DUM(6,6) ,  
5 EDISP(MEVAB,6) ,DAPP(6,6)

DATA R0 ,R1 ,R3 ,R8 ,R45

& /0.0D0,1.0D0,3.0D0,8.0D0,45.D0/

\*\*\*\*\*

DESCRIPTION OF ACTIVE VARIABLES MATRICES IN THIS SUBROUTINE

\*\*\*\*\*

NDOFN = number of degrees of freedom ((dimensions)

NELEM = number of elements

NEVAB = number of degrees of freedom per element

NGAUS = gauss point rule

NMATS = number of materials

NNODE = number of nodes per element

NPOIN = total number of nodes in base-cell

NPROP = number of material properties

NSTRE = number of independent stress terms

ELOAD(MEVAB,MELEM,MSTRE) = set of six independent "load" vectors  
corresponding to the six apparent strains  
(stored for each element in base-cell)

EVOLUME(MELEM) = volume of each element

COORD(MPOIN,MDIME) = nodal coordinates

PROPS(MMATS,MPROP) = material properties

SHAPE(MNODE) = displacement shape functions

DERIV(MDIME,MNODE) = derivative functions of shape functions

CARTD(MDIME,MNODE) = mapped derivatives from isoparametric element to  
actual element coordinates

GPCOD(MDIME,MTOTG) = gauss point coordinates

TDISP(MTOTV,6) = Global nodal displacement matrix (for six load cases)

TVOLUME = total base-cell volume

BVOLUME = solid volume of base-cell

BMATX(MSTRE,MEVAB) = strain-displacement matrix

DMATX(MSTRE,MSTRE) = constitutive matrix for base-cell  
solid-volume material

ELCOD(MDIME,MNODE) = local element coordinates

ESTIF(MEVAB,MEVAB) = element stiffness matrix

EDISP(MEVAB,6) = local element nodal displacements

DAPP(6,6) = apparent constitutive matrix

\*\*\*\*\*

\*\*\* THIS SUBROUTINE CALCULATES THE HOMOGENISED CONSTITUTIVE MATRIX  
\*\*\* OF THE MICROSTRUCTURE

\*\*\*\*\*

PRINT\*, 'ENTERING HOMOGENISATION ROUTINE'

Accumulate contributions to DAPP from each element

TVOLUME = R0

DO 999 IELEM =1, NELEM

PRINT\*, 'ELEMENT: ', IELEM

LPROP = MATNO(IELEM)

YOUNG = PROPS(LPROP, 1)

POISS = PROPS(LPROP, 2)

Evaluate coordinates and the micro displacements of the element

nodal points for each independent load case

DO 10 INODE =1, NNODE

LNODE=IABS(LNODS(IELEM, INODE))

NPOSN=(LNODE-1)\*NDOFN

DO 10 IDOFN=1, NDOFN

ELCOD(IDOFN, INODE)=COORD(LNODE, IDOFN)

DO 10 I=1, 6

EDISP(((INODE\*3)-3+IDOFN), I)=TDISP(NPOSN+IDOFN, I)

10 CONTINUE

09 continue

KGASP=0

Enter numerical integration loop

Initialise DUMMY

DO 15 ISTORE=1, 6

DO 15 JSTORE=1, 6

DUMMY(ISTORE, JSTORE)=R0

15 CONTINUE

DO 70 IGAUS=1, NGAUS

EXISP=POSGP(IGAUS)

DO 70 JGAUS=1, NGAUS

ETASP=POSGP(JGAUS)

do 70 kgaus=1, nkaus

ezesp=posgp(kgaus)

KGASP=KGASP+1

Evaluate the constitutive matrix

CALL MODPS(DMATX, LPROP)

Evaluate the shape functions, elemental volume etc.

CALL SFR2(ETASP, EXISP, ezesp)

CALL JACOB2(ELCOD, DJACB, IELEM, KGASP, 1)

DVOLUME=DJACB\*WEIGP(IGAUS)\*WEIGP(JGAUS)\*weigp(kgaus)

Evaluate the strain-displacement matrix

CALL BMATPS( BMATX ,ELCOD ,KGASP )

\*\*\*\*\*

Calculate homogenised constitutive matrix

\*\*\*\*\*

DO 60 ISTORE=1, 6

DO 60 JSTORE=1, 6

DO 60 IEVAB=1, NEVAB

DUMMY(ISTORE, JSTORE) = DUMMY(ISTORE, JSTORE) +

1 BMATX(ISTORE, IEVAB) \*

2 EDISP(IEVAB, JSTORE) \*

3 DVOLUME

60 CONTINUE

70 CONTINUE

Initialise DUM





```

PRINT*,'HOW MANY GLOBAL ELEMENTS REQUIRE POSTPROCESSING?'
READ(6,*) NTOTEL
PRINT*,'GLOBAL ELEMENTS:',NTOTEL

Open file to store microstrains for later use in error calculations
open(11,file='micro.res',status='unknown')

** Calculate tissue strains using REDUCED or FULL integration ???
PRINT*,'REDUCED INTEGRATION => STRAINS CALCULATED AT CENTROID'
PRINT*,'FULL INTEGRATION      => STRAINS CALCULATED AT GAUSS '
PRINT*,'
          POINTS AND AVERAGED (AT CENTROID)'
PRINT*,'DO YOU WANT TO USE REDUCED OR FULL INTEGRATION'
PRINT*,'TO CALCULATE THE TISSUE STRAINS ? (R or F)'
READ(6,20) RF
IF(RF.EQ.'R'.OR.RF.EQ.'r') THEN
  PRINT*,'USING REDUCED INTEGRATION'
ELSE
  PRINT*,'USING FULL INTEGRATION'
  GOTO 25
ENDIF

** Calculate B-matrix at REDUCED integration gauss point
MODE1=1
NGAUS = 1
GOTO 26
25 CONTINUE
** Calculate B-matrix at FULL integration gauss points
MODE1=1
NGAUS = 2
26 CONTINUE
CALL GAUSSQ(NGAUS)

Read apparent strain values from file and calculate microstrains
for each global base cell element
LOOP over tissue strain calculation for each global element)
DO 115 ITOTEL=1,NTOTEL
  READ(15,1085) MACELEM, (STRAPP(MACELEM,JSTRE),JSTRE=1,4),
1 STRAPP(MACELEM,6), STRAPP(MACELEM,5)
1085 FORMAT(I13,6(1X,G11.4))

DO 110 IELEM=1,NELEM
  LPROP = MATNO(IELEM)
  YOUNG = PROPS(LPROP,1)
  POISS = PROPS(LPROP,2)

Evaluate coordinates and micro displacements of the element
nodal points
DO 30 INODE =1,NNODE
  LNODE=IABS(LNODS(IELEM,INODE))
  NPOSN=(LNODE-1)*NDOFN
  DO 30 IDOFN=1,NDOFN
    ELCOD(IDOFN,INODE)=COORD(LNODE,IDOFN)
    DO 30 I=1,6
      EDISP(((INODE*3)-3+IDOFN),I)=TDISP(NPOSN+IDOFN,I)
30 CONTINUE

Initialize BSTORE matrix
DO 40 ISTRE=1,MSTRE
  DO 40 IEVAB=1,MEVAB
40 BSTORE(ISTRE,IEVAB)=R0
KGASP=0

Enter numerical integration loop

DO 90 IGAUS=1,NGAUS
  EXISP=POSGP(IGAUS)
  DO 90 JGAUS=1,NGAUS
    ETASP=POSGP(JGAUS)
    do 90 kgaus=1,ngaus
      ezesp=posgp(kgaus)

```

